Title
Hyperspectral Imaging and Machine Learning for Nanomaterials Characterization

Author
shevitski, brian

Publication Date
2019

Hyperspectral Imaging and Machine Learning for Nanomaterials Characterization

by

Brian Shevitski

A dissertation submitted in partial satisfaction of the

requirements for the degree of

Doctor of Philosophy

in

Physics

in the

Graduate Division

of the

University of California, Berkeley

Committee in charge:

Professor Alex K. Zettl, Co-chair
Doctor Shaul Aloni, Co-chair
Professor Michael F. Crommie
Professor Junqiao Wu

Fall 2019

Hyperspectral Imaging and Machine Learning for Nanomaterials Characterization

Abstract

Hyperspectral Imaging and Machine Learning for Nanomaterials Characterization

by

Brian Shevitski

Doctor of Philosophy in Physics

University of California, Berkeley

Professor Alex K. Zettl, Co-chair

Doctor Shaul Aloni, Co-chair

Nanoscale material systems are of great importance for answering open questions in fundamental science and enabling advancements in next-generation technologies. This dissertation explores the structural, electronic, and optical properties of several nanomaterial systems at the atomic-, nano-, and micro- length scales. A collection of analytical characterization tools, non-trivial imaging methods, and advanced data analysis techniques are presented. This methodology is essential for finding and understanding new physics in nanomaterial systems; it is also an important tool for characterizing new nanomaterial systems and determining the relationship between synthetic parameters and relevant material properties. Applications of these techniques to a wide array of scientific questions are given throughout the thesis.

A newly discovered source of highly localized light emission in hexagonal boron nitride (h-BN) is presented. This luminescent color center is closely related to unique impurities and native defects that occur exclusively in high-quality samples grown using a special high-pressure, high-temperature synthetic routine. An electron beam is used as a probe to characterize the luminescence, as well as activate and deactivate the light emission. The electron beam can also be used to deterministically create arbitrary nanoscale light emission patterns in h-BN synthesized using more conventional methods. A variety of h-BN polytypes are discussed and the effects of growth parameters, geometry, dimensionality, impurity concentration, and sample preparation on light emission are discussed.

Transition-metal dichalcogenides (TMDs) are an exciting class of Van der Waals (VDW) materials that display a variety of unique phenomena in their 2D (monolayers) and 1D (nanotubes and nanoribbons) forms that are absent in the bulk material. A special synthesis method which allows for targeted growth of specific nanostructures is presented along with characterization of the TMD nanomaterials. A combination of special transmission electron

microscopy (TEM) techniques and advanced data analysis methodology allows for rapid determination of the grain structure of continuous, nanocrystalline, monolayer TMD films.

Gallium chalcogenides (GCs) are another class of VDW materials, closely related to TMDs, that are of significant interest to the nanoscience community. The type and concentration of chalcogen atoms in these materials can be varied, resulting in a alloys with tunable structural, electronic, and optical properties. A combination of TEM, angle-resolved photoemission spectroscopy (ARPES), and photoluminescence (PL) is used to fully characterize the quasiparticle band structure, optical bandgap, and crystalline phase of the alloys across their compositional range. Monolayers of these materials exhibit a distinct change in band structure, resulting in the material transitioning from direct bandgap in the bulk to indirect bandgap in the 2D limit.

The characterization and analysis methods discussed here are broadly applicable to a wide variety of nanomaterial systems. Widespread adoption of machine learning and automation in the nanoscience community is a promising route toward high-throughput scientific inquiry.

VITA

2012	B.A. (Physics), University of California, Los Angeles
2014	M.A (Physics), University of California, Berkeley
2012 -2017	Graduate Student Instructor, Department of Physics, University of California, Berkeley
2012 - 2019	Graduate Student Researcher, Department of Physics, University of California, Berkeley and The Molecular Foundry, Berkeley, CA

PUBLICATIONS

B. Shevitski, S. Ulstrup, R.J. Koch, H. Cai, S. Tongay, L. Moreschini, C. Jozwiak, A. Bostwick, A. Zettl, E. Rotenberg, and S. Aloni, Tunable Electronic Structure in Gallium Chalcogenide van der Waals Compounds. *Physical Review B* 100 (2019) pp. 165112.

B. Shevitski, S.M. Gilbert, C.T. Chen, C. Kastl, E.S. Barnard, E. Wong, D.F. Ogletree, K. Watanabe, T. Taniguchi, A. Zettl, and S. Aloni, Blue-Light-Emitting Color Centers in High-Quality Hexagonal Boron Nitride. *Physical Review B* 100 (2019) pp. 155419.

S. Turner, **B. Shevitski**, H. Long, M. Lorenzo, J. Marquez, S. Aloni, V. Altoe, M. Worsley, and A. Zettl, Self-Assembly and Metal-Directed Assembly of Organic Semiconductor Aerogels and Conductive Carbon Nanofiber Aerogels with Controllable Nanoscale Morphologies. *Carbon* 153 (2019) pp. 648-656.

J. Cahill. S. Turner, J. Ye, **B. Shevitski**, S. Aloni, T. Baumann, A. Zettl, J. Kuntz, and M. Worsley, Ultra-High Temperature Ceramic Aerogels. *Chemistry of Materials* 31 (2019) pp. 3700-3704.

S.M. Gilbert, T. Pham, M. Dogan, S. Oh, **B. Shevitski**, G. Schumm, S. Liu, P. Ercius, S. Aloni, M.L. Cohen, and A. Zettl, Alternative Stacking Sequences in Hexagonal Boron Nitride. *2D Materials* 6 (2019) pp. 021006.

D.J. Garfield, N.J. Borys, S.M. Hamed, N.A. Torquato, C.A. Tajon, B. Tian, **B. Shevitski**, E.S. Barnard, Y.D. Suh, S. Aloni, J.B. Neaton, E.M. Chan, B.E. Cohen, P.J. Schuck, Enrichment of Molecular Antenna Triplets Amplifies Upconverting Nanoparticle Emission. *Nature Photonics* 12 (2018) pp. 402-407.

S.M. Gilbert, G. Dunn, A. Azizi, T. Pham, **B. Shevitski**, E. Dimitrov, S. Liu, S. Aloni, and A. Zettl, Fabrication of Subnanometer-Precision Nanopores in Hexagonal Boron Nitride. *Scientific Reports* 7 (2017) pp. 1-7.

S. Turner, H. Long, **B. Shevitski**, T. Pham, M. Lorenzo, E. Kennedy, S. Aloni, M. Worsley, and A. Zettl, Density Tunable Graphene Aerogel Using a Sacrificial Polycyclic Aromatic Hydrocarbon. *Physica Status Solidi* (b) 254 (2017) pp. 1700203.

C. Kastl, C.T. Chen,T. Kuykendall, **B. Shevitski**, T.P. Darlington, N.J. Borys, A. Krayev, P.J. Schuck, S. Aloni, A.M. Schwartzberg, The Important Role of Water in Growth of Monolayer Transition Metal Dichalcogenides. *2D Materials* 4 (2017) pp. 021024.

M. Sainato, A. Sahu, **B. Shevitski**, J.D. Forster, S. Aloni, G. Barillaro and J.J. Urban, Long Range Order in Nanocrystal Assemblies Determines Thin Film Charge Transport. *ACS Omega* 2 (2017) pp. 3681-3690.

T. Pham, A. Fathalizadeh, **B. Shevitski**, S. Turner, S. Aloni, and A. Zettl, A Universal Wet-Chemistry Route to Metal Filling of Boron Nitride Nanotubes. *Nano Letters* 16 (2015) pp. 320-325.

B. Shevitski, M. Mecklenburg, W. A. Hubbard, E. R. White, B. Dawson, M. S. Lodge, M. Ishigami, and B. C. Regan, Dark-field transmission electron microscopy and the Debye-Waller factor of graphene. *Physical Review B* 87 (2013) pp. 045417.

E. R. White, M. Mecklenburg, **B. Shevitski**, S. B. Singer, and B. C. Regan, Charged Nanoparticle Dynamics in Water Induced by Scanning Transmission Electron Microscopy. *Langmuir* 28 (2012) pp. 3695-3698.

Dedicated to anyone who contributes to Wikipedia or Stack Exchange.

Preface

I was involved in a wide array of exciting, interdisciplinary, and collaborative projects during my tenure as a graduate student. This thesis documents that work. A common theme is hyperspectral imaging techniques applied to nanomaterial systems. The massive amount of complex, multidimensional data I needed to analyze led me to discover and adopt advanced data analysis methods from other fields. These techniques allow for rapid processing and interpretation of large complex data sets and has made my research much more impactful, especially from an interdisciplinary perspective.

The first two chapters of the thesis present useful background information on characterization techniques, especially hyperspectral imaging, and advanced data analysis methods. Applications of these techniques (usually instances where I have been involved in projects in more of a supporting role) are dispersed throughout these chapters.

The subsequent chapters discuss the details of projects I have worked on as a primary contributor. Each chapter is meant to be able to stand on its own, supported by the background material in the first several chapters. These chapters are essentially more in-depth, expanded versions of the publications that have resulted from my graduate research.

I hope that this thesis is pleasant to read for my committee and useful to any readers who think it might be helpful for their research.

-Brian Shevitski

Acknowledgments

Graduate school has been a long, hard struggle. I couldn't have done it without the help of a long list of people. Thank you all for everything you've done for me over the years.

Research Advisors:
Shaul Aloni
Alex Zettl

PhD Committee:
Mike Crommie
Junqiao Wu
Jeff Neaton

Friends and Family:
Maree Caput
Darlene Rivera
Mark Sims
Sara Rivera
Rudy Craig-Anders
Ruben Anders
Kathleen Craig
Sammy Bochat
Daniel Werder
Isaac Nicholson
Patrick Connolly
Mark Morgan
Michael Girard
Matt Jaffe
Eric Thewalt and Elaine Angelino
Andy Smith
Wil Velasco
Donna Moore and George Robinson
Steve and Patty Seidensticker
Patrick, Kim, Joe, and Lisa Seidensticker
Jeff Moore and Kathleen Ghiloni

Zettl Lab, UC Berkeley:
Jon Deasy
Laura Lutz-King
Thang Pham
Matt Gilbert
Sally Turner
Scott Meyer
Derek Popple
Donez Horton-Bailey
Alex Ungar
Gabe Schumm
Willi Mickelson
Gabe Dunn
Aidin Fathalizadeh
Seita Onishi
Ashley Gibb
Hu Long
Wu Shi
All of Matt and Sally's undergrads

Physics Department, UC Berkeley:
Anne Takizawa
James Analytis
Holger Müller
Erin Sohr
Jackie Brosamer
Melanie Veale
Terry Buehler
Claudia Trujillo
Joelle Miles
Anne Takizawa

The Molecular Foundry:
Nick Borys
Chris Chen
Christoph Kastl
Adam Schwartzberg
Melanie West
Vittorino Lanzio
Katherine Cochrane
Bruno Schuler
Andrew Thron

David Garfield
Jim Schuck
Aeron Hammack
Peter Ercius
Andy Minor
Colin Ophus
Mary Scott
Karen Bustillo
Jim Ciston
Rohan Dhall
Marissa Libbee
Chengyu Song
Tom Pekin
Alex Weber-Bargioni
Lorenzo Maserati
Erika Penzo
Monica Lorenzon
Stefano Dallorto
Benedikt Ursprung
David Hom
Paul Ashby
Mike Elowson
Mike Nielsen
Virginia Altoe
Ed Barnard
Ed Wong
Paul Ashby
Jeff Neaton
Tess Smidt
Perry Lao
Suksham Barun
Meg Holm
Tev Kuykendall
Tracy Mattox
Frank Ogletree

Advanced Light Source:
Søren Ulstrup
Roland Koch
Eli Rotenberg

UCLA:
Chris Regan
Matt Mecklenburg
Jared Lodico
Ed White
Billy Hubbard
Luke Wukmer
Dot Gong

Collaborators:
Kenji Watanabe (NIMS Japan)
Takashi Taniguchi (NIMS Japan)
Marcus Worsley (LLNL)

Everyone Else:
My Publication Reviewers
Bill Burr
Ganyao
Everyone at PRS
Sam Harris
Dave Chappelle
Joe Rogan
The Inventor of Cheese
Paul Thomas Anderson
Bernie Sanders
Louie C.K.
Stanley Kubrik
Founders of thepiratebay
The Troops

Contents

List of Figures

List of Tables

Chapter 1

Experimental and Imaging Methods

> *"One of the great things about books is sometimes there are some fantastic pictures."*
>
> — George W. Bush

1.1 Chapter Introduction

This chapter presents a brief theoretical and practical introduction to the various imaging techniques used to characterize and study the nanomaterial systems presented in later chapters. These imaging methods can be roughly grouped into two categories: conventional and hyperspectral.

Conventional imaging produces two-dimensional data from a single collection channel. Generally speaking, the contrast in conventional image data is interpreted using a physical model to connect the sample-excitation interaction with the resulting counts in the detection channel. The most common example of a conventional imaging technique is optical microscopy, in which a specimen is placed under uniform illumination and the intensity of reflected (or transmitted) light is recorded by the pixels of a camera.

Hyperspectral imaging, also referenced simply as spectral imaging (SI) or spectral mapping, measures the spatial distribution of spectroscopic features. Generally speaking, SI rasters a small probe of electrons or photons across a sample and records the response at every pixel. Multiple spectroscopic information channels (as well as conventional imaging channels) can be acquired simultaneously and the relationship between the data channels can be inferred using a variety of techniques. SI is a powerful method for understanding the relationship between material properties such as crystal structure, morphology, optical properties, and electronic behavior. A familiar example of SI is photoluminescence (PL) mapping, where a laser is focused to a diffraction limited spot, rastered across a specimen, and a light emission spectrum is recorded at every location.

To effectively extract information from imaging data, it is import to keep two key questions in mind: What is the resolution of the instrument or technique? What are the physical mechanisms that produce contrast in the image? These two parameters (resolution and contrast mechanism) are the focus of the following sections, which outline the imaging techniques referred to throughout the thesis.

1.2 What is Resolution?

The resolution of an imaging technique typically refers to the smallest distance that two points can be separated by and still be recognized as two distinct objects [1], as shown in figure 1.1. The usual mathematical description for this is the Rayleigh limit (figure 1.1(b)), which is satisfied when the first minimum of one intensity distribution is located at the central maximum of another intensity distribution. Other definitions of resolution exist, such as the Sparrow limit [2] (figure 1.1(c)), when the combined light from two overlapping and equally bright intensity distributions is constant along a line between their central peaks. Alternative definitions, such as the Sparrow limit, are less common. Throughout this thesis the Rayleigh definition of resolution is used unless otherwise specified.

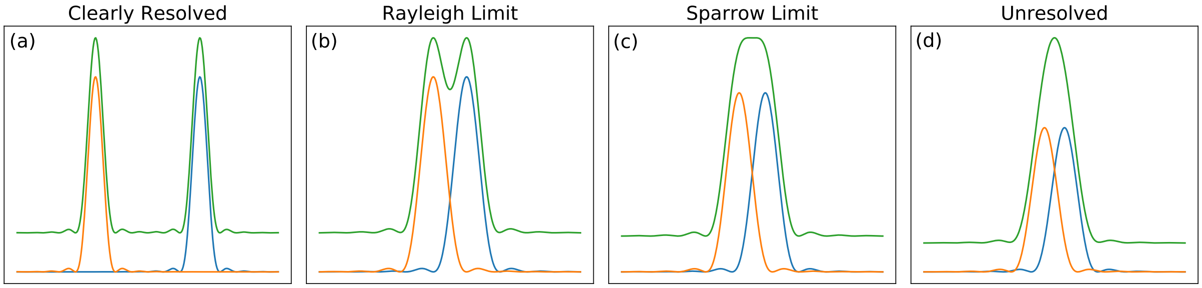

Figure 1.1: Illustration of basic resolution criteria. The two points in (a) are separated by a large enough distance such that they are obviously distinct. The Rayleigh limit, when the central maxima of one peak is located at the first minima of the other (panel (b)), is usually accepted as the limit of resolution for two points. The Sparrow limit, in panel(c), is slightly lower than the Rayleigh limit, but is not generally used when discussing the resolution of an instrument.

From a mathematical perspective, the size of the smallest probe that can formed by an imaging system is the same as the Rayleigh limit of resolution between two points for that system. The smallest probe that can be formed, or the diffraction limit, from a wave with wavelength λ passing through a (circular) aperture with numerical aperture NA is:

$$d = \frac{1.22\lambda}{\mathrm{NA}} \tag{1.1}$$

The numerical factor in the numerator is a consequence of the Airy function which describes the far-field distribution of intensity (diffraction) when a wave passes through a circular aperture. Equation 1.1 shows that it is desirable to have a small wavelength excitation with high numerical aperture (usually referred to as convergence angle in the context of electron optics) for high-resolution imaging.

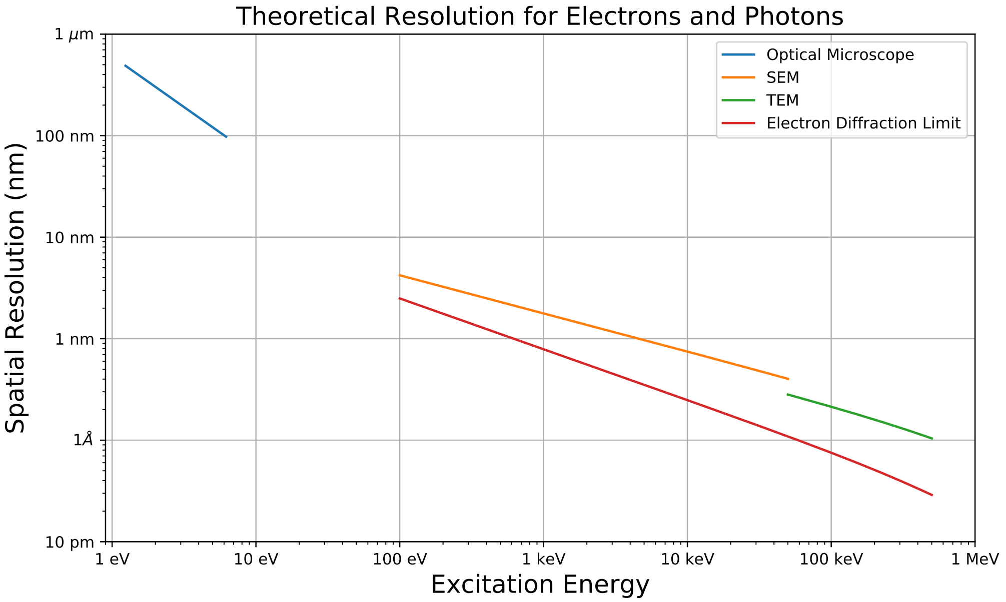

Figure 1.2: Plot of resolution limits for imaging with electrons and photons. Optical microscopy at the diffraction limit is commonplace, and the resolution is dictated mostly by the wavelength of light used. Electron optics are much more complicated and are effectively limited by the need to use lower convergence angles (NA) due to aberrations caused by the magnetic lenses in the electron optical system. As a result, higher resolution is usually achieved by using electrons with higher kinetic energy.

Some imaging techniques are not limited by the size of the smallest probe that can be formed, but rather by the volume of the sample that has a significant interaction with the excitation probe [3]. This fact is especially relevant to techniques that use a small probe to excite a specimen and measure the response. In particular, the resolution of cathodoluminescence (CL) in the scanning electron microscope (SEM), presented in section 1.14 and used extensively in chapters 5 and 6, is limited by the size of the excitation volume more than the size of the probe (see figure 1.3).

A similar effect can occur when the sample-excitation interaction is long-range, such as the excitation of phonons or plasmons by fast electrons. The resolution of electron energy-loss spectroscopy (EELS), presented in section 1.10, is limited by this delocalization effect [4], leading to challenges when mapping spatial variations of electronic properties in nanostructures.

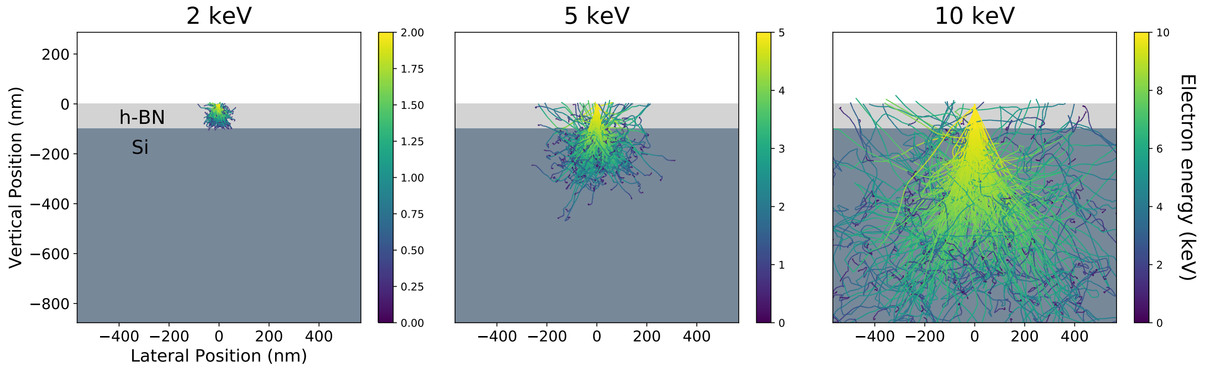

Figure 1.3: Simulated trajectories of electrons traveling through boron nitride on silicon. The nominal size of the probe is only 1 nm, but much larger volumes of linear sizes ranging from 10-1000 nm are interrogated by the probe, depending on the excitation energy.

1.3 Transmission Electron Microscopy (TEM)

Transmission electron microscopy (TEM) is a powerful tool for interrogating materials on meso, nano, and atomic length scales [5, 6, 7]. This instrument uses a beam of electrons accelerated through a potential in the keV to MeV range to probe a specimen. TEM has a wide field of view, large range of magnifications, and many operational modes. Figure 1.4 shows the main TEM operational modes, which are discussed in more detail in the following sections.

In conventional TEM imaging (figure 1.4(a)), a parallel beam of electrons interacts with a thin sample, scatters, is refocused, and forms a magnified image of the sample. In diffraction mode (figure 1.4(b)) the angular distribution of electron scattering from the sample is recorded. In scanning TEM (STEM), a convergent probe of electrons is rastered across the sample and the response is recorded using a variety of detection channels (figure 1.4(c)).

TEM is particularly well-suited to studying nanomaterials as high-energy electrons have wavelengths much shorter than inter-atomic distances in solids. The wavelength-energy relation for electrons with relativistic kinetic energy, E, is:

$$\begin{aligned}\lambda(\mathrm{E}) &= \frac{hc}{\sqrt{\mathrm{E}^2 + 2\mathrm{E}\,mc^2}}\\ \frac{\lambda(\mathrm{E})}{(\mathrm{pm})} &= 1240 \times \left(\left(\frac{\mathrm{E}}{(\mathrm{keV})}\right)^2 + 1022\frac{\mathrm{E}}{(\mathrm{keV})}\right)^{-1/2},\end{aligned} \tag{1.2}$$

where h is Planck's constant, m is the electron rest mass, and c is the speed of light. Using equation 1.2 reveals that a 200 keV electron (a typical electron energy for TEM operation) has a wavelength of ~ 2.5 pm, far below the angstrom length scales that are typically relevant for solid-state physics.

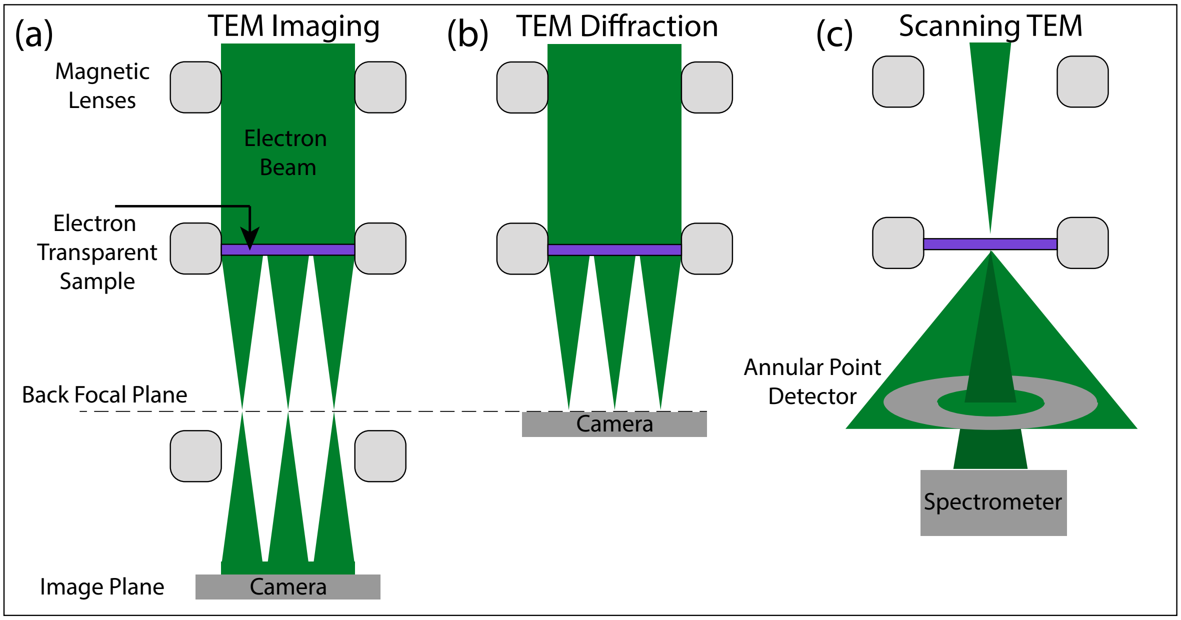

Figure 1.4: Overview of basic TEM operation modes. In conventional imaging mode (a), a parallel beam is used and an image is formed by focusing the electrons scattered by the sample. In diffraction mode (b), the angular distribution of scattered electrons is captured. Scanning mode (c) rasters a convergent probe across the sample, and data is collected at each raster point.

In practice the actual resolution of TEM is far above the diffraction limit. Most TEMs are limited by the aberrations introduced by the crude electromagnetic lenses used for focusing electrons. Even advanced TEMs, that have special optics and software to correct the worst of these aberrations, are limited by instabilities in the instrument, departures from monochromaticity in the electron beam, and higher-order aberrations. Finally, practically speaking, the stability of the sample under study usually imposes the limit of resolution. Beam damage, signal to noise, hydrocarbon contamination, and vibrations of the sample are usually the limiting factors for the resolution of TEM imaging experiments. Practical and theoretical limits of resolution for the various modes of imaging in TEM are presented in the following sections.

1.4 TEM Sample Prep

Special considerations must be made in order for a sample to be interrogated using TEM. Because the signal in TEM is generated using electrons transmitted through a material, a TEM sample must be electron transparent. A good sample allows a sufficient number of transmitted electrons to fall on the detection system to enable the acquisition of high signal-to-noise data in a reasonable amount of time. The threshold for electron transparency is mainly a function of the electron beam energy and the average atomic number (Z) of the sample. Electrons with high kinetic energy can penetrate further into samples with low Z, and *vice versa*. Generally speaking, the thinner the sample, the better. In practice, TEM samples should be less than 100 nm in thickness with an ideal sample being 10-20 nm.

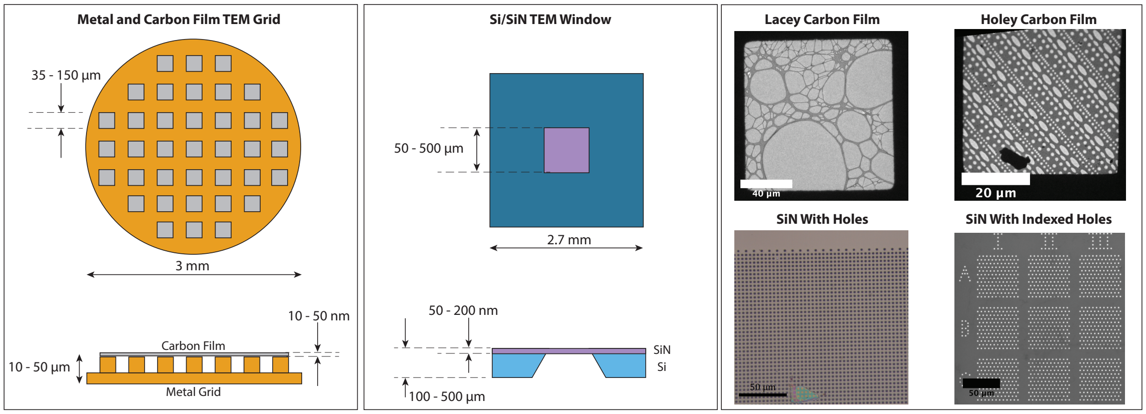

Figure 1.5: Overview of TEM sample grid and support film types (not to scale). The most common sample substrate is a metal grid covered with a thin amorphous carbon support film. Another common substrate is an electron transparent SiN window supported by an underlying Si chip. The electron transparent window is created using lithographic techniques and chemical etching to remove the underlying Si, so the dimensions of the electron transparent window are highly customizable. The electron transparent support film can also be customized with variable-sized holes or indexing for specific applications.

Nanostructures are highly electron-transparent, making TEM imaging a perfect tool for studying them. However, in this extreme limit of thinness, certain modes of analytical TEM become impractical or impossible. Monolayer materials, nanotubes, and single chain materials have very few atoms for the electron beam to interact with. This makes spectroscopic techniques such as electron energy-loss spectroscopy (EELS) or energy-dispersive x-ray spectroscopy (EDS or EDX) nearly impossible for some nanostructure specimens. Also, in this few-atom limit some more common TEM techniques like scanning transmission electron microscopy (STEM) and select-area electron diffraction (SAED) become much more challenging due to a lack of specimen-beam interaction and resulting contrast.

The easiest method for preparing a nanomaterial specimen for TEM is suspension of material in solution followed by drop casting onto a TEM grid or window (see figure 1.5). This technique is especially useful for high throughput studies of nanoparticles, nanotubes, nanowires, and aerogels. These materials are easily suspended in solution and sonication usually separates the individual nanostructures from one another. Provided that the solution has the proper concentration of material, drop casting provides a TEM sample with well separated nanostructures that are easy to image and characterize.

Studying 2D materials using TEM is slightly more challenging. Typically, specimens must be thinned from bulk material (usually by mechanical exfoliation using tape) and transferred to an intermediate substrate before being transferred to a TEM substrate. Preparation of 2D material TEM samples is more of an art than a science, and several common methods are presented below. Methods for preparing samples of this type fall into two main categories: polymer-free and polymer-assisted.

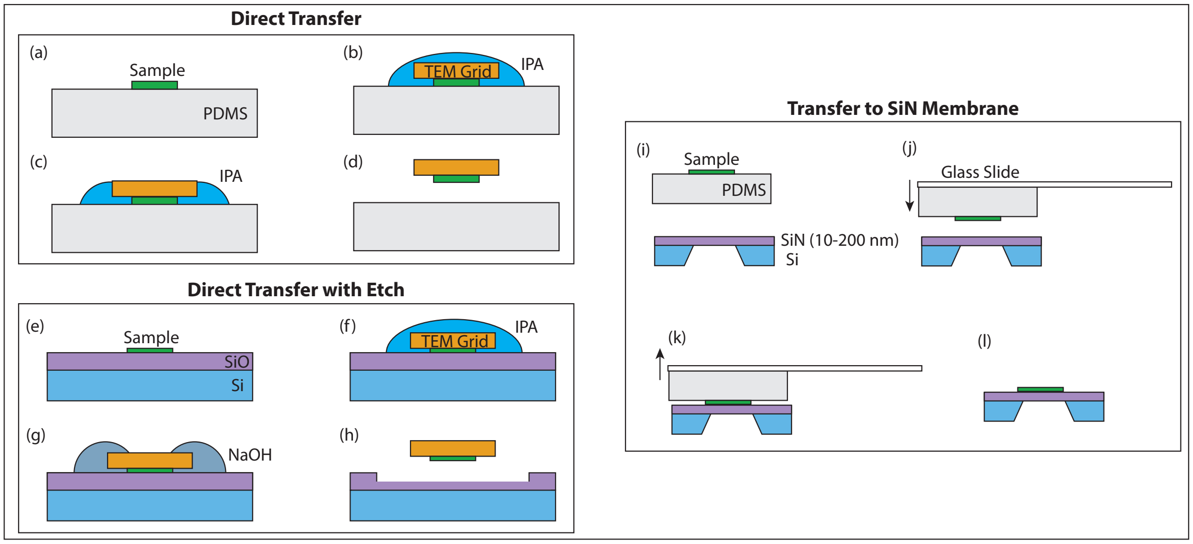

Figure 1.6: Overview of polymer free TEM sample preparation techniques. In the first direct transfer technique, material is first exfoliated onto a sticky PDMS substrate (a). A metal and carbon film TEM grid is then adhered to the 2D material flake by placing the grid on top of the sample, depositing a drop of IPA, and allowing the IPA to dry (a). Once dry, another drop of IPA is placed (c), freeing the 2D material from the PDMS but not the grid, which is then removed (d). A similar method uses a Si/SiO intermediate substrate (e). The grid is affixed in the same way as before (f) but is freed from the intermediate substrate by etching away the SiO layer using NaOH or similar ((g) and (h)). A PDMS stamp with affixed 2D material can also be used (i). The stamp can be aligned with an underlying TEM window (j) under an optical microscope using a micromanipulation translation stage and the 2D material can be deterministically transferred to a specific region ((k) and (j)).

In polymer-free or direct transfer methods (see figure 1.6 for overview), thin pieces of 2D material are transferred from an intermediate substrate to a TEM grid or window either by using surface forces from a drying drop of solvent to adhere 2D material to the grid [8], or by using pressure to transfer material from a stamp to a TEM window [9]. When using the surface tension of a drying liquid, an extra step is required to free the specimen from the underlying substrate. This can be accomplished using chemical etching or a subsequent application of solvent to change the surface forces between the substrate and the 2D material. Samples made using these techniques are usually cleaner and of higher quality than samples made using the polymer transfer techniques discussed below. The stamping method also has the distinct advantage of having the ability to deterministically transfer specific pieces of material to predefined locations.

Polymer-assisted transfer techniques (figure 1.7) are very common and are advantageous because they allow for easy preparation of samples. In these methods, the material to be studied is embedded in a matrix of polymer which is then removed from the intermediate substrate. The 2D material can then be transferred to a TEM substrate, and the polymer is removed with further processing. Early versions of this technique used PMMA as the transfer matrix [10], but more recent methods that use polyacrylate (PC) are capable of producing high quality samples, with a low degree of contamination [11].

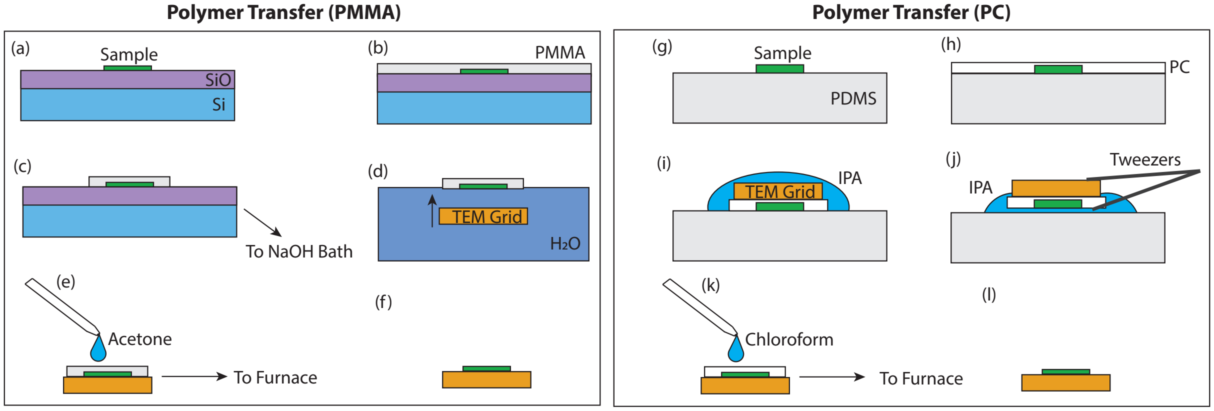

Figure 1.7: Overview of TEM sample preparation techniques using polymer transfer. Flakes of material are exfoliated onto a Si/SiO substrate (a) and a thin layer of PMMA is spun onto the surface (b). Excess PMMA is scraped away, and the substrate is transferred to a NaOH bath to etch away the oxide layer (c). After the polymer-encased 2D material is freed from the intermediate substrate by chemical etching, it is washed in water and scooped up with a TEM grid (d). Finally, the excess polymer is removed using solvent and/or annealing (e). Panels (g) - (i) show a similar routine that uses polyacrylate instead of PMMA and does not require a chemical etch.

A final note about TEM sample prep: SiN TEM windows have a distinct advantage for sample prep because material can be synthesized directly on the TEM imaging substrate, completely eliminating the need for transferring the material. This is especially helpful for delicate thin-films or diffuse nanostructures, such as those presented in Chapter 7. This technique is also necessary for TEM imaging of nanoparticle superlattices, presented in section 2.14.

1.5 Conventional TEM Imaging

In conventional TEM, a monochromatic plane-wave of electrons (parallel beam) is incident on a thin sample. The electrostatic potential of the crystal weakly perturbs and scatters the incident plane wave. The angle of scattered electrons, θ, is related to the scattered wave spatial frequency, q, (or alternatively the momentum transferred) via the relation:

$$\theta = \lambda\, q, \tag{1.3}$$

where λ is the electron wavelength. High-resolution TEM imaging theory treats the specimen as a weak-phase object (WPO). The WPO approximation assumes that the beam electrons are weakly perturbed by the sample, acquiring a phase-shift as they traverse the specimen. The incident electrons traveling an infinitesimal distance $\mathrm{d}z$ through a specimen at speed v, will accumulate an amount of phase:

$$\mathrm{d}\varphi = \frac{V(z)\,\mathrm{d}z}{\hbar v}. \tag{1.4}$$

The phase-shifted scattered electron waves are refocused by a magnetic lens (objective lens) and interfere with the unscattered portion of the incident beam electron wave, resulting in an image. Ideally, a TEM image is a phase-contrast map of the projected electrostatic potential of the specimen.

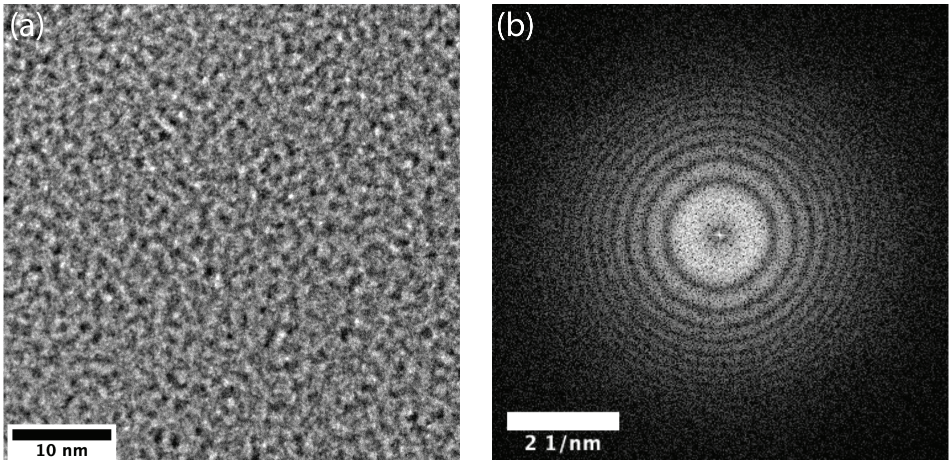

Figure 1.8: TEM image and fast Fourier transform of amorphous carbon. The power spectrum (b) of the image (a) shows that the contrast transfer function (CTF) is oscillatory for low and medium spatial frequencies and damped at the highest spatial frequencies.

However, due to the imperfect nature of electromagnetic lenses (aberrations), the scattered electrons acquire additional phase shifts as they pass through the objective lens. The objective lens phase shift (in frequency space) is given by:

$$\chi(q) = \frac{\pi}{2\lambda}\Big(-2\Delta f(\lambda q)^2 + C_s(\lambda q)^4\Big), \tag{1.5}$$

where Δf is the lens defocus, and C_s is the spherical aberration coefficient of the lens (typical values of C_s for TEMs are in the range of 1 -2 mm). Because of these additional phases from lens aberrations, the final image is a convolution of the projected potential with a contrast transfer function (CTF), which is given by:

$$\mathrm{CTF} = \sin(\chi(q)). \tag{1.6}$$

Inspection of the CTF (figure 1.9) reveals that the TEM is a band-pass imaging system; the pass band is a complicated, oscillatory function related to image defocus and lens aberration.

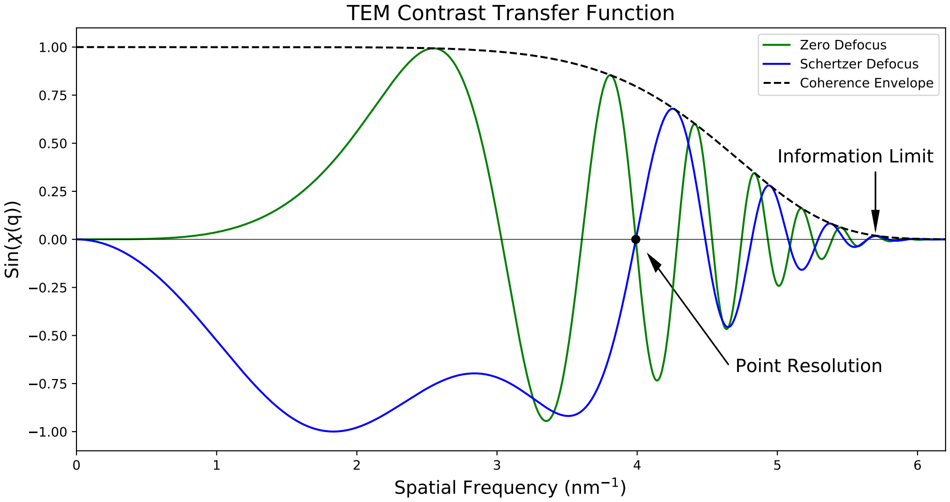

Figure 1.9: Contrast transfer function (CTF) for TEM. The TEM acts as a band-pass imaging system. The width of the first pass band, is maximized by setting the defocus to a special value (Scherzer defocus), which defines the point resolution of the instrument. The CTF is oscillatory so with sufficient knowledge of the instrument conditions, information can still be extracted past the resolution limit . Contrast transfer is exponentially damped for higher spatial frequencies; the width of the damping function defines the information limit of the instrument.

The oscillatory nature of the CTF reveals that contrast in TEM is not necessarily easy to interpret. An ideal band-pass imaging system would have a uniform response across the band of spatial frequencies relevant to the measurement. In order to approximate a flat response, a special defocus value is chosen based on the wavelength of the electrons and the value of the spherical aberration, called the Scherzer defocus. The Scherzer defocus is defined as:

$$\Delta f_s = \sqrt{\frac{3C_s\lambda}{2}}. \tag{1.7}$$

The resolution in TEM imaging is defined as the first zero of the CTF (approximately the bandwidth of the first pass band) at the Scherzer defocus value and is given by:

$$d_s = \sqrt[4]{\frac{C_s \lambda^3}{6}}. \tag{1.8}$$

The Scherzer resolution, d_s, is much larger than the diffraction-limited resolution, showing that the resolution of normal TEM is limited by spherical aberration, not wavelength. An alternative view is that the resolution is diffraction limited, with the effective NA restricted to smaller values that exclude the distorted portion of the wavefront. Aberration corrected TEMs achieve higher resolution mostly by correcting the spherical aberration with software and specially designed lenses.

Inspection of the CTF reveals that if one has sufficient knowledge of their instrument, information can be extracted from images beyond the resolution limit. However, The CTF is exponentially damped at higher spatial frequencies due to partial coherence of the electron source, a finite range of electron kinetic energies in the beam, and instrument instabilities. No information can be obtained for spatial frequencies outside of the coherence envelope. The width of the coherence envelope is aptly called the information limit of the instrument.

1.6 Crystallography

The majority of research in solid state physics is focused on crystals, systems that have regular periodicity or long-range (compared to typical electron wavelengths in the system) order. Nanomaterials are of particular interest because they have long range order in zero (nanoparticles, nano-onions, and fullerenes), one (nanotubes, nanowires, and chain materials), or two (2D materials) dimensions and are spatially confined in the remaining dimensions. Crystallography is the mathematical formalism used to describe the periodicity in solid state systems [12, 13].

In a periodic system (lattice), the position of any point can be described by a vector,

$$\mathbf{R}_{uvw} = u\mathbf{a}_1 + v\mathbf{a}_2 + w\mathbf{a}_3, \tag{1.9}$$

where u, v, and w are integers and $\mathbf{a}_i$ are the lattice vectors of the system. The defining feature of a periodic system is that any point in the system can be reached using a linear combination of these lattice vectors.

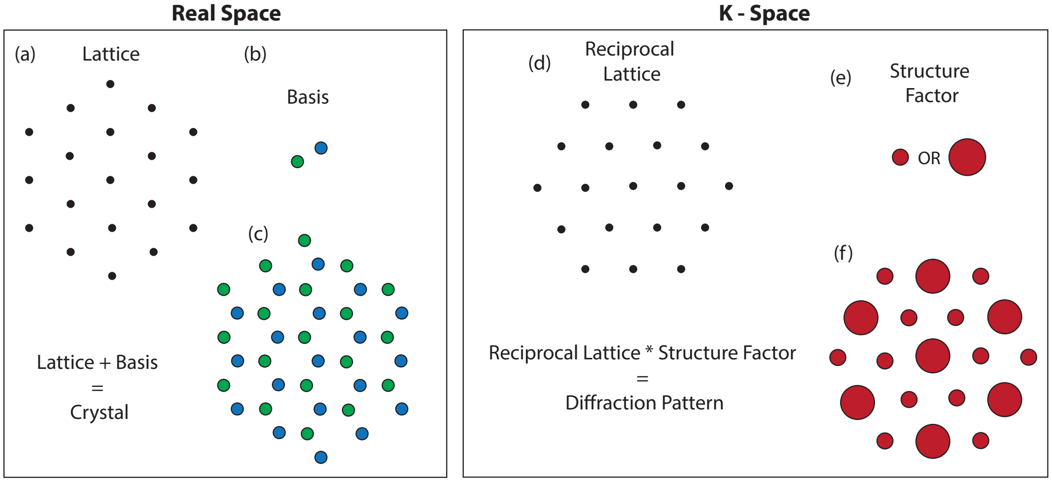

Figure 1.10: Cartoon of Basic crystallography and diffraction concepts. (a)-(c) illustrate how a crystal is defined by the addition of a basis to each point of a spatially periodic lattice. The reciprocal lattice (d), along with the structure factor (e) for each point gives the diffraction pattern. In this cartoon, the atomic form factor has been neglected.

In general, the atoms in a crystal are not periodic; that is an arbitrary atom is not connected to every other atom by a linear combination of lattice vectors. In order to describe the atoms in a crystal, a basis is attached to each lattice point (see figure 1.10(a)) using a basis vector, $\boldsymbol{\delta}$. In this way, any atom in the crystal can be indexed by first indexing the lattice point (u, v, w) and then specifying the basis point (i), resulting in:

$$\mathbf{R}_{\text{atom}_i} = \mathbf{R}_{uvw} + \boldsymbol{\delta}_i. \tag{1.10}$$

Another closely related fundamental solid-state concept is the reciprocal lattice. While the regular lattice describes a periodic system in real space, the reciprocal lattice describes the system in reciprocal space (usually referred to as k-space). The reciprocal lattice vectors are analogous to the the regular lattice vectors (any reciprocal lattice point can be reached by a linear combination of reciprocal lattice vectors) and are defined by the following orthogonality relation:

$$\mathbf{a}_i \cdot \mathbf{b}_j = \delta_{ij} \tag{1.11}$$

where $\mathbf{a}_i$ is a lattice vector, $\mathbf{b}_j$ is a reciprocal lattice vector, and δ_{ij} is the Kronecker delta. Common notation uses the indices h, k, and l to refer to a reciprocal lattice point,

$$\mathbf{G}_{hkl} = h\mathbf{b}_1 + k\mathbf{b}_2 + l\mathbf{b}_3. \tag{1.12}$$

1.7 Electron Diffraction

Serious study in the field of solid state physics began with the discovery in 1912 by Max von Laue, that x-rays are diffracted by solids [14]. This confirmed the long-held belief that atoms in crystals were arranged in a periodic manner (inferred from observations of symmetry in macroscopic crystals and the angles between crystal facets). This discovery led to von Laue being awarded the 1914 Nobel prize in physics. Over 100 years later, diffraction from crystals remains an indispensable tool for studying new condensed matter systems.

Due to their wavelike nature and short wavelength, electrons can also be diffracted by crystals. The diffracted intensity of electrons scattered from a crystal can be found using the first Born approximation [15, 16] to calculate the far-field scattered electron wavefunction,

$$\psi_s(\mathbf{q}) = \sum_{\text{atoms}} f_a(q)\, e^{i\,\mathbf{q}\cdot\mathbf{R}_{\text{atom}}} \tag{1.13}$$

where $\mathbf{q}$ is the momentum transferred to the electron from the crystal ($\mathbf{q}$ is also the k-space coordinate for the wavefunction and is proportional to the scattering angle), and $f_a(q)$ is the atomic form factor, which describes the scattering from an individual atom.

Under the first Born approximation, the atomic form factor is the Fourier transform of the atomic potential, $\mathrm{V}(r)$, of the particular atom in question, given by:

$$f_a(\mathbf{q}) = \left| \frac{\gamma m}{2\pi\hbar^2} \int \mathrm{d}^3\mathbf{r}\; \mathrm{V}(r)\, e^{2\pi i\,\mathbf{q}\cdot\mathbf{r}} \right|^2 \tag{1.14}$$

where γ is the Lorentz factor of the fast electrons in the beam, m is the electron rest mass, and $\hbar$ is the reduced Planck constant. An approximate, analytical solution can be obtained for the atomic form factor by using the screened Coulomb or Yukawa potential in equation 1.14, given by:

$$\mathrm{V}(r) = \frac{\mathrm{Z}\, e^2\, e^{-\mu r}}{r} \tag{1.15}$$

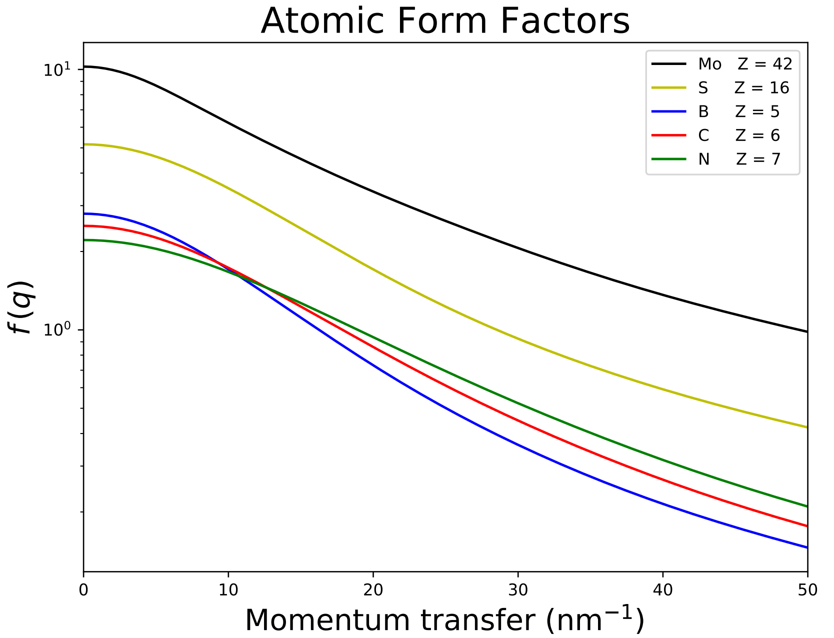

Figure 1.11: Plot of numerically generated atomic form factors for selected elements. Heavier elements generally scatter more than lighter ones and scattering is suppressed for high momentum transfers.

where Z is the atomic number of the atom, μ is a characteristic screening length, and e is the electronic charge. In this model the atomic form factor is [17]:

$$f_a\left(\mathbf{q}\right) = \left(\frac{2\gamma\ \alpha mc^2}{\hbar c}\right)^2 \frac{\mathrm{Z}^2}{\left(\mu^2 + \left(2\pi q\right)^2\right)^2} \tag{1.16}$$

where α is the fine structure constant and c is the speed of light. Inspection of equation 1.16 reveals that $f_a\left(\mathbf{q}\right) \sim \mathrm{Z}^2/q^4$. This shows two intuitive results, heavier elements scatter more than lighter ones and scattering is suppressed for higher momentum transfers.

Generally speaking, form factors are not calculated using analytical models such as the one presented above. It is much more common to calculate atomic form factors from tabulated results that use more complex theoretical models. The most common approach is to approximate $f_a\left(\mathbf{q}\right)$ by a weighted sum of Gaussians [18] according to:

$$f_a\left(\mathbf{q}\right) = \sum_i a_i\ e^{-b_i q^2} \tag{1.17}$$

where a_i and b_i are tabulated values for each element.

Figure 1.11 shows the atomic form factor for five elements using this numerical approach. At first glance, the numerical method has the same general features as the analytical model presented earlier (heavier elements scatter more and scattering is suppressed at high q). However, closer inspection reveals that at low q, some lighter elements scatter more than heavier ones, demonstrating the need for more sophisticated models in calculating scattering intensities.

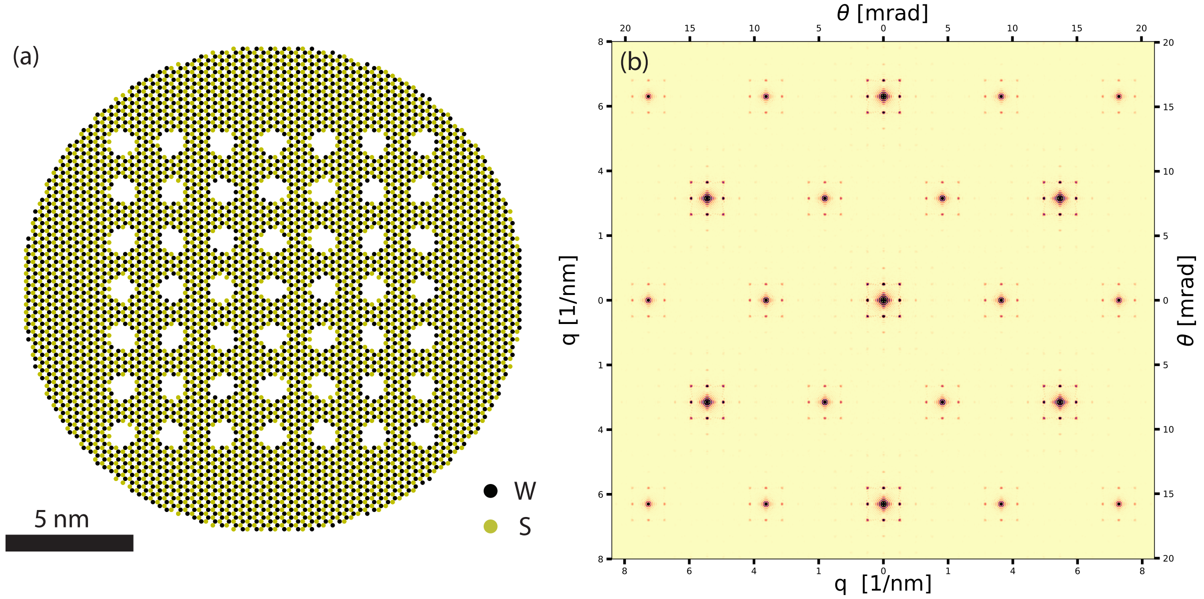

Figure 1.12: Cartoon graphic and numerical diffraction simulation of a 20 nm area of WS_2 with an array of holes with 1 nm diameter and 2 nm pitch.

Equations 1.13 and 1.17 can be used directly to calculate diffraction intensities for arbitrary arrangements of atoms. This is especially useful in the case of nanostructures, such as nanotubes, heterostructures, and ion milled arrays of holes in 2D materials, as shown in figure 1.12. These systems generally have a lower degree of symmetry and higher complexity compared to traditional bulk systems, which makes simulation of their diffraction patterns difficult or impossible using most commercially available crystallography software tools.

Equation 1.13 can be further simplified to make calculation of diffraction intensities more efficient. Substitution of equations 1.9 and 1.10 into equation 1.13 gives:

$$\psi_s\left(\mathbf{q}\right) = \sum_{\text{lattice}} e^{i\,\mathbf{q}\cdot\mathbf{R}_{\text{atom}}} \sum_{\text{basis}_i} f_i\left(q\right) e^{i\,\mathbf{q}\cdot\boldsymbol{\delta}_i} \tag{1.18}$$

Furthermore, relation 1.11 leads to the following identity:

$$\sum_{\text{lattice}} e^{i\,\mathbf{q}\cdot\mathbf{R}_{\text{atom}}} = \delta\left(\mathbf{q} - \mathbf{G}_{hkl}\right) \tag{1.19}$$

where δ is the Dirac delta function. This indicates that the only places in k-space with appreciable intensity are points on the reciprocal lattice. This fact is used to infer the crystal structure of a material from an experimental diffraction pattern.

Putting everything together, simplifying, and squaring the wavefunction leads to the following expression for the intensity of a diffraction spot with indices (hkl):

$$\psi_s^* \psi_s = I_{hkl} = \left| \sum_{\text{basis}_i} f_i \left(\mathrm{G}_{hkl} \right) e^{i\, \mathbf{G}_{hkl} \cdot \boldsymbol{\delta}_i} \right|^2 \tag{1.20}$$

Equation 1.20, numerical atomic form factors (equation 1.17), and symmetry arguments are generally how diffraction patterns of bulk crystals are simulated. The quantity in equation 1.20 is usually called the structure factor of the crystal, and along with the reciprocal lattice, defines the diffraction pattern of a crystal, as illustrated in figure 1.10(d).

1.8 Dark-Field TEM (DF-TEM)

Dark-field TEM (DF-TEM) is a useful TEM operation mode for imaging crystalline systems. The general concept is outlined in figure 1.13. In DF mode, an image is formed with electrons that scatter into a small range of angles. This results in an image that has bright contrast in regions that have a specific crystallographic phase and orientation defined by an aperture in the back focal plane. This imaging technique is especially useful for visualizing the spatial distribution of individual crystalline grains in a polycrystalline sample [19, 20].

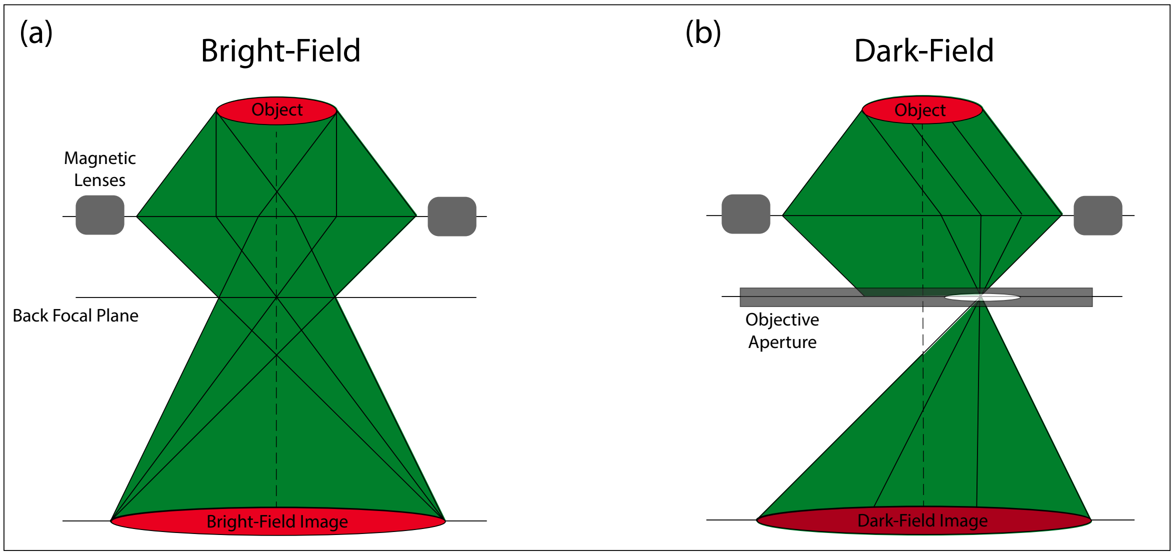

Figure 1.13: Cartoon Illustrating dark-field TEM. In conventional TEM (a), the image is formed by all scattered electrons. In dark-field mode (b), only those electrons in a small range of angles, defined by a small aperture in the back focal plane, contribute to the image intensity.

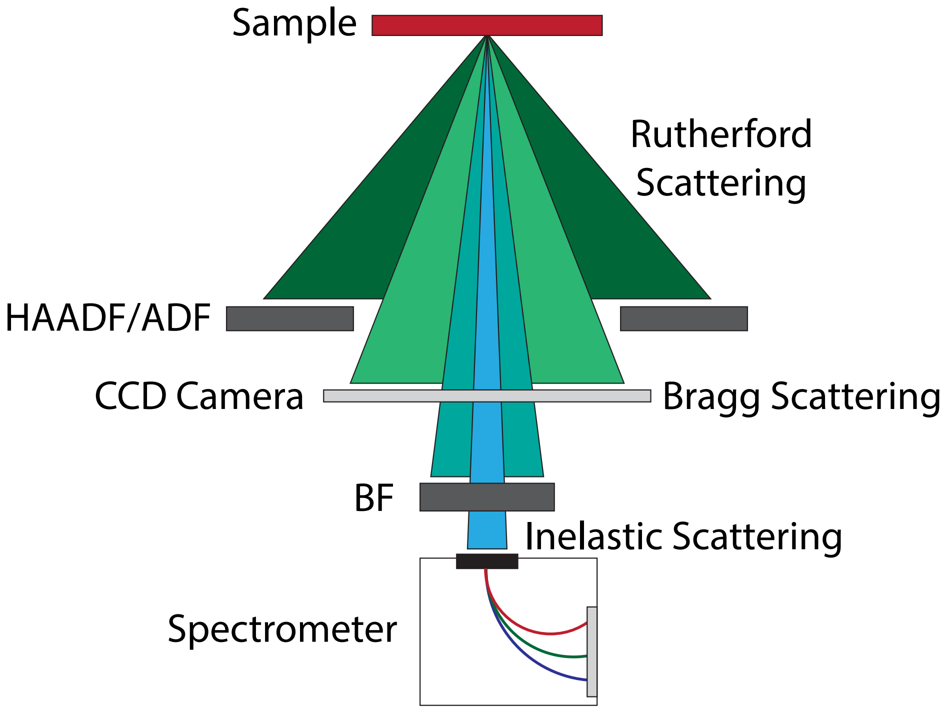

Figure 1.14: Summary of STEM detection channels and scattering types. The most common imaging mode uses an annular pixel detector to record the intensity of scattering in a well-defined angular range. The range of scattering angles can be varied by changing the camera length between the sample and the detector. The angular scattering distribution can be fully captured at each pixel using a CCD camera, revealing the local crystallography at each point. Using a pixel detector aligned with the central beam results in a bright-field image which can have higher resolution than the dark-field image. The energy distribution of the central beam can be analyzed resulting in an EELS spectrum image.

1.9 Scanning Transmission Electron Microscopy (STEM)

In STEM operation, a small, convergent probe of electrons is rastered across a specimen and the response is recorded using a variety of detectors, as shown in figure 1.14. STEM can use both elastically and inelastically scattered electrons to form an image. A summary of detection channels and scattering types is given in table 1.1.

We begin our discussion of STEM imaging with the most common detection channel, the annular detector. Hyperspectral STEM imaging using alternative detection channels will be discussed in detail in the following sections. An annular dark-field (ADF) detector records the intensity of elastic scattering from a sample in a well-defined range of angles. The specific range of angles can be controlled by changing the effective distance between the

Detector	**Scattering Type**	**Number of Dimensions**
BF	Elastic+Inelastic	2
ADF	Elastic	2
HAADF	Elastic Rutherford	2
4DSTEM	Elastic Bragg	4
EELS	Inelastic	3

Table 1.1: Table of STEM detection channels and scattering types, along with the number of dimensions in the final data.

sample and detector (called the camera length). At high angles (HAADF), the scattering is well-approximated by elastic Rutherford scattering.

The count rate, R, of electrons scattered from a specimen of thickness t, with areal density of atoms n, at the HAADF detector is:

$$\mathrm{R} = \frac{I}{e} n t \sigma \tag{1.21}$$

where I is the beam current, e is the electron charge, and σ is the scattering cross-section. To a first approximation, the Rutherford elastic scattering cross-section can be used to determine how the STEM contrast depends on material parameters. The Rutherford cross-section is:

$$\sigma_R = \frac{e^4\,\mathrm{Z}^2}{16\mathrm{E}_0^2} \frac{\mathrm{d}\Omega}{\sin^4{(\theta/2)}}. \tag{1.22}$$

Here Z is the atomic number of the atom in question, E_0 is the kinetic energy of the electrons, θ is the scattering angle, and $\mathrm{d}\Omega$ is the solid angle subtended by the detector. Combining equations 1.21 and 1.22 reveals that the contrast in STEM scales in the following way:

$$\mathrm{R} \sim \mathrm{Z}^2\, t\, n. \tag{1.23}$$

Contrast in HAADF STEM reveals variations in average atomic composition, density, and thickness across a sample. This intuitive contrast mechanism, as well as the strong dependence on atomic number, makes STEM an incredibly useful imaging technique for understanding complex material systems.

For very thin samples composed of light elements, it is often useful to use ADF imaging (as opposed to HAADF) to create an image with reasonable signal to noise. By increasing the camera length, counts from high intensity Bragg spots are recorded by the detector. This makes the quantitative analysis of intensities in the STEM image more difficult (the $\sim Z^2$ dependence breaks down and interference effects enter into images) but does not alter the positions of features recorded in the image. ADF STEM at high camera lengths is particularly useful for imaging few-layer h-BN and graphene, as presented in Chapter 3.

The spatial resolution of STEM imaging is dictated by the smallest probe that can be formed by the imaging system. For normal microscopes, the smallest probe is limited by the spherical aberration of the probe-forming objective lens and is

$$d \approx 0.4\sqrt[4]{C_s\lambda^3}. \tag{1.24}$$

The STEM resolution of the JEOL 2100-F microscope (the primary TEM used in this thesis) at 200 keV is in the 5-10 angstrom range. Aberration-corrected microscopes are able to reduce the spherical aberration to nearly zero and are able to form probes that are nearly diffraction limited (as defined by equation 1.1). In practice, the probe size is slightly larger than the diffraction limit due to higher order aberrations, but still allows for straight forward atomic resolution imaging. The resolution of the TEAM microscopes at the Molecular Foundry, used for the atomic resolution imaging presented here, is $\sim$ 50 pm.

1.10 STEM Electron Energy-Loss Spectroscopy (STEM-EELS)

Electron energy-loss spectroscopy (EELS) is the analysis of the energy distribution of electrons transmitted through a specimen. The forward-scattered electrons are fed into a magnetic electron spectrometer and the resulting energy distribution is captured with a CCD camera (see figure 1.14). The electrons in the EEL spectrum that have inelastically interacted with phonons or electrons in the material reveal information about the chemistry, electronic structure, dielectric response, thickness, vibrational properties, and band gap of the specimen.

The great power of STEM EELS is the ability to simultaneously collect spectral information at each point in a sample. This is useful for mapping spatial variations of material properties across a heterogeneous sample. For homogeneous samples, STEM mapping allows for the fast iteration of many, nearly identical, experiments. This allows for high-fidelity measurements with increased signal to noise, and enables statistical analysis of the material property under study.

The mechanisms that produce contrast in an EELS HI are numerous and complex. The low-loss region of the EEL spectrum ($\lesssim$ 50 eV) contains information about phonons, interband transitions, plasmons, and other optical phenomena in the material. Features in the higher-energy-loss region of the spectrum come from transitions between the atomic orbitals to the bands of the material, revealing details about the local chemistry of the material. The relevant physics are discussed in greater detail in each section that makes use of this technique.

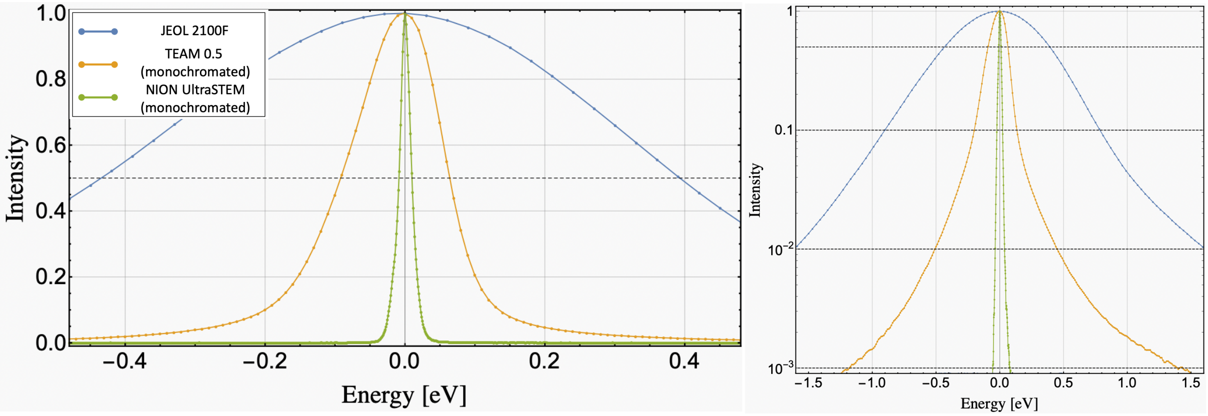

Figure 1.15: Zero-loss peaks extracted from experimental data for three classes of microscope.

Microscope	**FWHM (eV)**	**FW 10^{-1} Max (eV)**	**FW 10^{-2} Max (eV)**	**FW 10^{-3} Max (eV)**
JEOL	0.83	1.69	3.22	7.36
FEI	0.16	0.33	0.96	2.57
NION	0.019	0.045	0.074	0.134

Table 1.2: Zero-loss peak characteristics extracted from experimental data for three classes of microscope.

The spatial and spectral resolutions are both important parameters for STEM-EELS measurements. There are two flavors of spectral resolution, the energy resolution, and the lowest energy feature that can be reliably measured. The spectral resolution of an EELS measurement determines how much detail can be observed in a spectrum and is dictated by the energy distribution of electrons in the incident beam. The zero-loss peak (ZLP) of the EEL spectrum reflects the energy distribution of electrons in the beam; the FWHM of the ZLP is usually used as the metric for the energy resolution of an EELS setup.

The lowest energy feature that can be measured is generally larger than the ZLP FWHM as the ZLP has long tails and spectral features usually have very low intensity compared to the ZLP. An important limiting factor for EELS imaging is the dynamic range of the spectrometer detector. The cross-section for inelastic scattering from the sample is quite small due to the high energy of the incident electrons, compared to the energy losses suffered. The majority of electrons transmitted through the sample do not lose any energy and contribute to the ZLP. For nanomaterial samples, the intensity of features in the EEL spectrum is $\sim 10^3$ - 10^4 times less than the intensity of the ZLP.

The ZLP for three classes of microscope are shown in figure 1.15. Unmonochromated microscopes (such as the JEOL 2100-F) are useful for reliably measuring energy loss above

∼5 eV and give spectral resolution somewhere close to 500 meV. A standard monochromated TEM (like the TEAM microscopes at the Molecular Foundry) can reliably measure band gaps and other optical and electronic properties above ∼1 eV, with spectral resolution around 100 meV. Ultra-monochromated NION microscopes can be used to measure vibrational and low-energy optical properties above ∼100 meV, with spectral resolution around 10 meV [21].

The spatial resolution of EELS is somewhat of a subtle topic and depends on both the size of the electron probe, and the energy-loss of the spectral feature of interest [4]. Figure 1.16 shows how the spatial resolution depends on the energy-loss of interest. For spectral features in 100 eV range (core-loss edges that give information about the chemical elements and bonding in a specimen), spatial resolution in the several angstrom range is possible. However, for losses in eV range (optical properties of solids), delocalization limits the spatial resolution to the tens of nanometers.

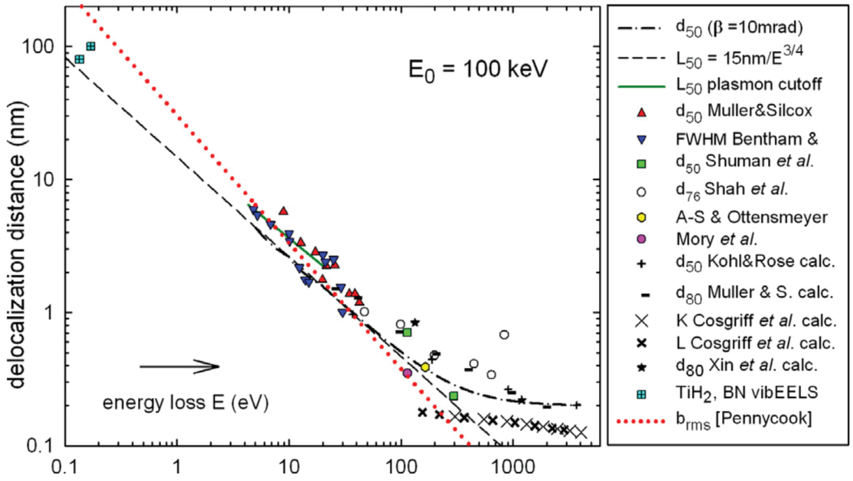

Figure 1.16: Delocalization distance in EELS as a function of energy loss based on experimental and theoretical results. Low-energy mechanisms can be excited at distances much greater than the size of the electron probe. Figure taken from "Scattering Delocalization and Radiation Damage in STEM-EELS", *Ultramicroscopy* (2017) [4].

1.11 Energy-Dispersive X-Ray Spectroscopy (EDS)

Energy-dispersive x-ray spectroscopy (EDS) is a technique that allows for the identification of atomic species in a specimen. The high-energy electrons in the STEM beam can eject an inner shell, or core electron. To replace the lost core electron, an electron from a higher shell drops down. This process results in the releases of a photon with energy equal to the difference between the two atomic energy levels.

The energy resolution of EDS is generally in the 10s of eVs and has much higher sensitivity to higher Z elements. The spatial resolution is limited by either the size of the probe or the size of the interaction volume, whichever is greater.

In STEM EDS, the x-ray emission intensity is collected at each pixel of a scan and results in an HI image. An example of an EDS HI is shown in figure 1.17. Slicing and integrating the spectra over well-defined energy windows at each pixel of the image results in maps of the local chemical composition, which can be used to quantify the local chemistry of a sample. EDS is a very useful synthesis feedback tool for determining the stoichiometry and nanomorphology of newly synthesized materials.

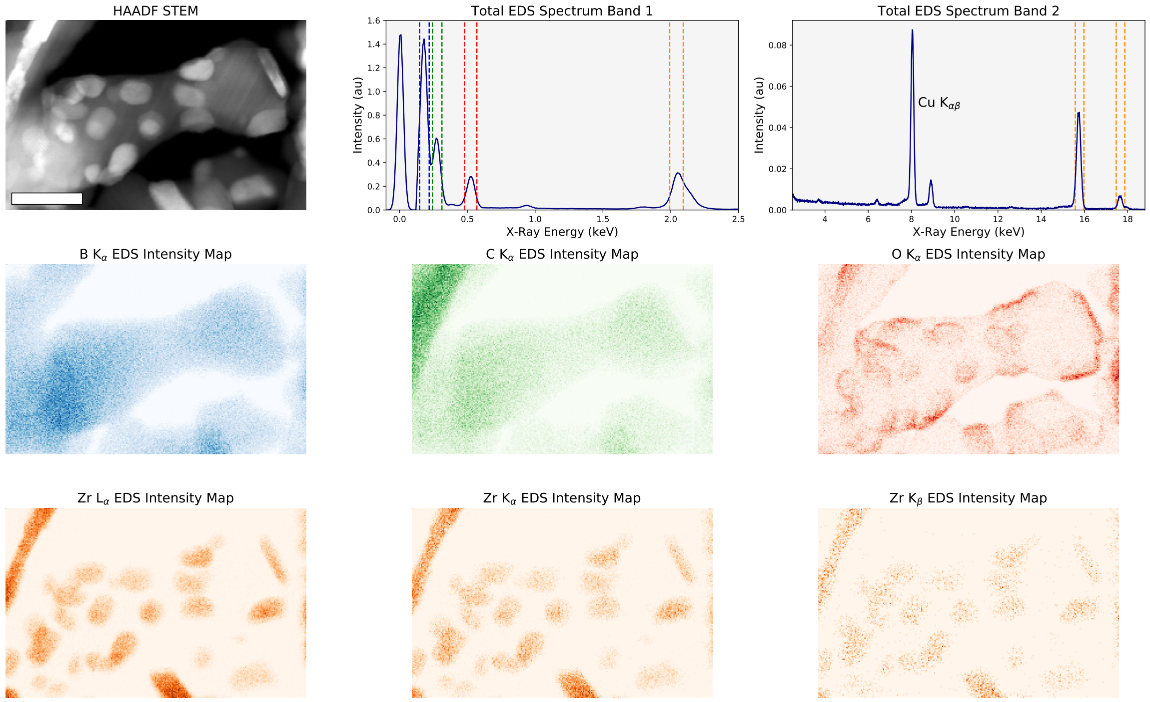

Figure 1.17: EDS characterization of Zirconium-Boron ceramic aerogels. Slicing and intergating the spectra at each pixel results in maps of the local chemistry in the material.

1.12 Scanning Nanobeam Electron Diffraction (4DSTEM)

The STEM beam can be used as a probe of local crystallography if the back focal plane (diffraction pattern) is recorded at each location of a scan, illustrated in figure 1.18. The stem probe is slightly defocused and the convergent beam electron diffraction (CBED) pattern is collected from each raster point of a scan. This technique, generally referred to as 4DSTEM, results in a wealth of information that can be used to determine local strain, crystal domain structure and texture, and even enable advanced ptychographic imaging methods. 4DSTEM is also useful for beam-sensitive materials because the electron dose can be greatly reduced and precisely controlled.

The spatial and spectral resolution of 4DSTEM are two closely linked quantities. Increased spatial resolution generally results in decreased spectral reolution and *vice versa*. A smaller electron probe has a higher convergence angle which causes diffraction spots to enlarge into disks. For samples with a high degree of local crystallinity, the spectral resolution can be greatly increased by fitting the diffraction disks.

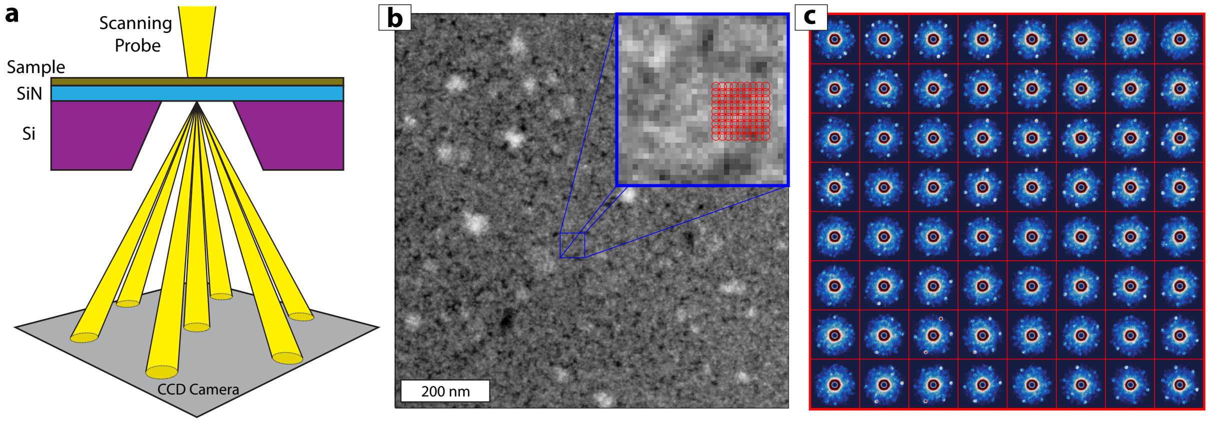

Figure 1.18: Panel (a) shows a schematic of the basic 4DSTEM experimental configuration. A small convergence angle beam of electrons is rastered across the specimen. A CCD detector in the back focal plane records the electron count (reflecting the diffraction pattern) at each probe location, thus measuring the local crystallography of the sample with nanometer scale resolution. Panel (b) shows a high-angle annular dark-field (HAADF) signal for a suspended thin sample of WS_2. The inset blue box is a zoom in (7X magnification) of the small blue square area outlined in the center of the image. 64 representative diffraction patterns acquired for the sample at the spatial locations identified by the red grid in (b) are shown in (c). The diameter of the red circles in (b) indicates the approximate probe size. In (c), each red box represents a spatial pixel of size 2 nm sampled by a 2.7 nm probe; the field of view of the diffraction pattern within each red box is 10.8 nm^{-1}.

1.13 Scanning Electron Microscopy (SEM)

SEM is very similar to STEM in that a focused beam of electrons is rastered across a sample and an image is formed using a variety of detectors. The SEM generally doesn't use transmitted electrons to form an image (although transmitted electron detectors do exist), so a much wider variety of samples can be studied. SEM is particularly useful as a feedback channel for synthesis because it allows a user to quickly and easily assess the morphology and chemistry of a material.

The most common detection channels are the secondary electron (SE) detector and the backscattered electron in-lens (IL) detector. Spectroscopic information channels, like EDS and cathodoluminescence (CL), can also be captured. In addition, because the SEM allows for an easy electrical connection to a sample, electron beam-induced current (EBIC) images can be created. The electrical connection also allows for transport dependent imaging as well as heating and cooling experiments. A schematic of the various detection channels available in the SEM is shown in figure 5.1.

Contrast in SE images results from low-energy ($\lesssim$ 50 eV) secondary electrons that are ejected from the band structure of a specimen by inelastic interactions with the beam.

Contrast in images from the IL detector comes from high-energy (keV) backscattered electrons from the beam that are reflected or back-scattered out of the specimen interaction volume by elastic scattering interactions with specimen atoms.

SEM optics are a greatly simplified version of TEM optics operating at much lower accelerating voltages (in the 1-20 keV range). As such, the SEM has spatial resolution significantly lower than in in TEM. Typically, an SEM can form an ~ 1 nm probe, but the resolution of the instrument is often hindered by the extended size of the electron interaction volume, as shown in figure 1.3. Reducing the energy of the beam reduces the size of the interaction volume. When used in conjunction with the IL detector, a lower energy electron beam can produce high resolution images of surface features on a sample. However, this results in a larger electron wavelength and often leads to lower signal to noise.

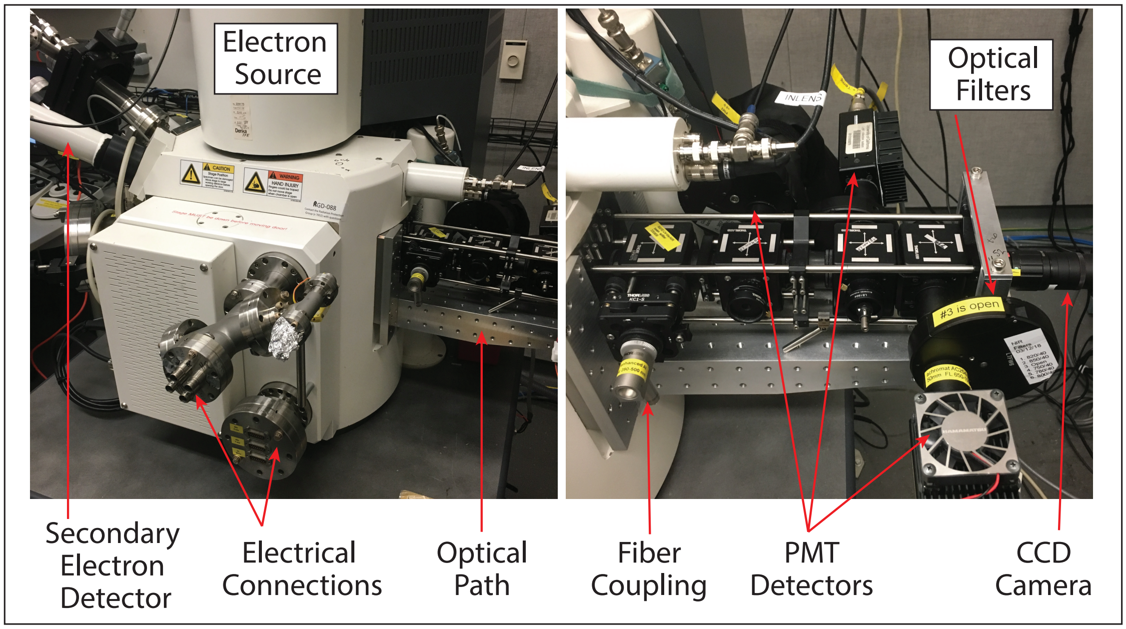

Figure 1.19: Zeiss Supra *in situ* SEM at the Molecular Foundry.

1.14 SEM Cathodoluminescence

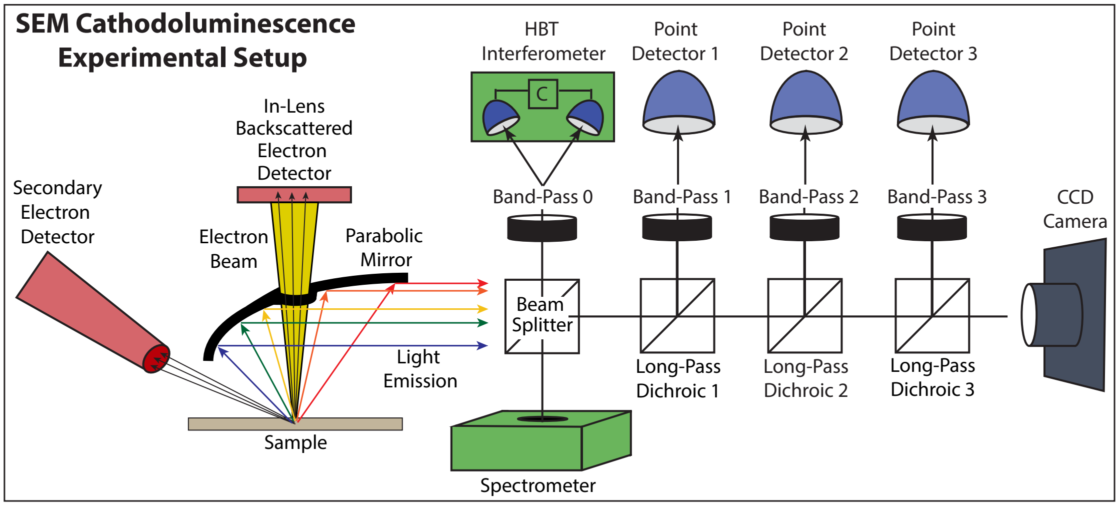

Figure 1.20: Overview of CL setup in the SEM. A more detailed discussion of this setup is given in Chapter 5

.

When high-energy electrons strike a specimen, they generate numerous electron hole pairs which can radiatively recombine and emit photons. The emitted light contains information about the band gap and defect states in a semiconductor. CL has several distinct advantages for studying the optical properties of semiconductors.

In contrast to photons, which have negligible momentum, electrons are able to easily probe indirect transitions that are not accessible using photoluminescence. Also, unlike laser excitation where an incident photon creates a single electron-hole pair, CL excitation results in the generation of many $e - h$ pairs, leading to emission from transitions that would not be observable otherwise.

CL also has the advantage of not being limited to studying optical transitions with energies less than the energy of a laser. This makes CL a useful tool for studying UV phenomena in wide-gap semiconductors, without the need for a specialized UV PL microscope.

One final advantage of using CL is it provides the ability to study the relationship between morphology and chemistry and optical properties on the nanometer length scale (opposed to the 100 nm length scale of diffraction limited PL).

The resolution of SEM CL depends on the size of the electron probe, the size of the interaction volume, and the diffusion length of carriers in the material. The CL data presented in Chapter 5 show how emissive features in different spectral regions can appear to have different sizes, although they all most likely originate from atomic scale defects much smaller than the electron probe.

Chapter 2

Image Analysis and Machine Learning

> *"With four parameters I can fit an elephant, and with five I can make him wiggle his trunk."*
>
> — John von Neumann

2.1 Chapter Introduction

One main unifying theme of this dissertation is digital image data analysis. These data originate from a variety of sources with each source requiring special consideration and the application of an assortment of analysis techniques. This section outlines various image analysis techniques used throughout this thesis. The goals of image analysis can be roughly grouped into two categories: altering images to make them more appealing to a human viewer and preparing images for measurement of features and then measuring those features. These methods can be found in any introductory text on image analysis [22].

In this section, I also outline the various machine learning techniques used in subsequent chapters. These techniques generally serve to automate data analysis or provide a quick and intuitive statistical outlook of the data. All of the machine learning methods used are open source packages in the Python programming language.

2.2 Kernel Operations

Perhaps the most fundamental concept in digital data analysis is the kernel operation. An image kernel operation is carried out by modifying the value of each pixel in an image using the values of neighboring pixels and a mathematical transformation. For example, a Gaussian blur or smoothing operation replaces each pixel value by the weighted sum of the original pixel with a neighborhood of nearby pixels. The new value of a pixel, P_{new}, with indicies (i, j) is obtained using:

$$P_{new}(i,j) = \sum_{\alpha,\beta=-\ell}^{\ell} w_{\alpha\beta} P_{old}(i+\alpha, j+\beta), \tag{2.1}$$

where P_{old} is the original pixel value and the weights, $w_{\alpha\beta}$, are elements from a $(2\ell+1) \times (2\ell+1)$ matrix sampled from a Gaussian distribution.

There are a huge variety of different kernel operations that can be applied to an image according to the application. Kernel applications are useful for denoising (smoothing), highlighting edges and features, and applying geometric transformations to images.

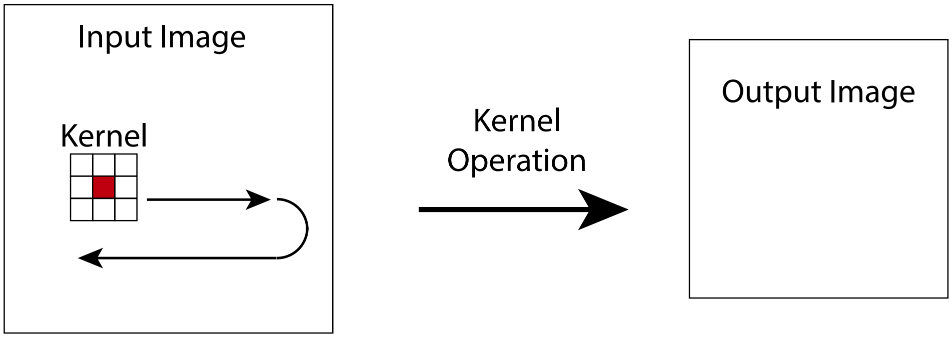

Figure 2.1: Illustration of kernel operations on an image. A kernel operation alters the value of each image pixel based on the values of surrounding pixels.

2.3 Frequency Space Operations

The discrete Fourier transform (FT) of an image, $F\left(i,j\right)$, is defined as:

$$f\left(p,q\right) = \sum_{i,j=0}^{N_{x,y}-1} F\left(i,j\right) e^{-2\pi\imath(p*i)/N_x} e^{-2\pi\imath(q*j)/N_y}. \tag{2.2}$$

For an image with $N = N_x N_y$ pixels, direct calculation of equation 2.2 runs in $\mathcal{O}(N^2)$ time (N sums of N terms). Fast, efficient algorithms used to calculate DFTs with sufficient precision in $\mathcal{O}(N \log N)$ time were discovered in the 1960s. DFTs calculated using these algorithms are generally called FFTs (fast Fourier transforms). Generally speaking, the terms DFT, FFT, and FT are used interchangeably.

FTs contain the exact same amount of information as their accompanying real space image, with the information displayed in a different way. Depending on the data to be displayed, either the FT or the real space image may be more enlightening. For example, displaying the FT of an image of a periodic structure is useful for clearly demonstrating the periodicity.

One great power of working in frequency space is that the FT and many of the common kernel operations are linear. This fact, coupled with the fact that many operations are more simple to compute in frequency space than in real space, means that working in frequency space can make analysis quicker and more intuitive. For example, the cross-correlation, $F \star G\left(\mathbf{x}\right)$, (see next section) between two real space functions, $F(\mathbf{x})$ and $G(\mathbf{x})$, is equal to the inverse FT of the product of their FTs, $f(\mathbf{q})$ and $g(\mathbf{q})$. Explicitly:

$$F \star G\left(\mathbf{x}\right) = \mathrm{FT}^{-1}\left[f\left(\mathbf{q}\right) * g\left(\mathbf{q}\right)\right] \tag{2.3}$$

Frequency space is very useful for making images more appealing to human perception. This is usually accomplished by taking an image's FT, multiplying the FT by some masking function image which passes frequencies within a specified band, and taking the inverse FT.

2.4 Cross-Correlation

The cross-correlation (CC) coefficient between two images, $F\left(x, y\right)$ and $G\left(x, y\right)$, is defined as:

$$\gamma\left(\tilde{x}, \tilde{y}\right) = F \star G\left(\tilde{x}, \tilde{y}\right) = \sum_{x,y} F\left(x + \tilde{x}, y + \tilde{y}\right) G\left(x, y\right). \tag{2.4}$$

If two images are shifted with respect to one another by an amount $\left(s_x, s_y\right)$, the coefficient $\gamma\left(\tilde{x}, \tilde{y}\right)$ will have a maximum at $\left(\tilde{x} = s_x, \tilde{y} = s_y\right)$. Cross-correlation is an invaluable tool for analysis of time-series image data because these data usually contain spatial drift due to instrument instability, thermal fluctuations, etc. Image registration using cross-correlation is shown in figure 2.2. First, the cc image, $\gamma\left(\tilde{x}, \tilde{y}\right)$, is computed for the the reference image and the shifted image. Next, the peak in the CC image is identified. Finally, the shifted image is moved into registration using interpolation and the values obtained from the CC image. The time-series data presented in figure 5.4 was aligned using this procedure.

Cross-correlation is also useful for finding specific features and sub-regions in images. The CC image, $\gamma\left(\tilde{x}, \tilde{y}\right)$, is calculated between the host image and a smaller template image. The CC image will have a maxima at $\gamma\left(x_0, y_0\right)$ at the location where a feature in the host image is similar to the template. A demonstration of this technique is presented in section 2.15.

2.5 Thresholding

Thresholding is the operation of turning a normal image into a binary image by setting all pixels above (below) some threshold value to 1 and all pixels below (above) to 0. It is often useful to threshold an image in order to quantify the spatial distribution of unique objects in the image. There are two main classes of thresholding operation: global, histogram-based thresholding and local, kernel-based thresholding.

In the histogram based approach, the pixel intensity values are analyzed and a threshold value is determined from the statistical properties of the data. Nearly any statistical metric can be used to set the threshold, and the flavor of thresholding can be tuned to fit the

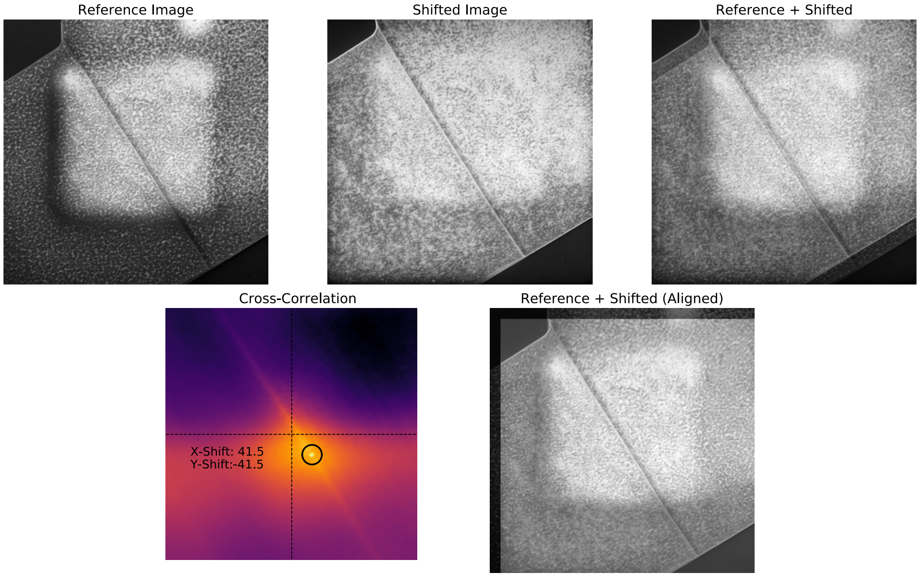

Figure 2.2: Demonstration of image registration using cross-correlation

application. Figure 2.3 shows the results of three different global threshold metrics on a STEM image of semiconductor nanoparticles.

Local thresholding is especially useful for images that have uneven illumination or several different intensity values of interest. Figure 2.4 shows the difference between the two threshold methods for the same image. The local threshold image does not suffer from the artefact caused by uneven intensity distribution that the global image contains.

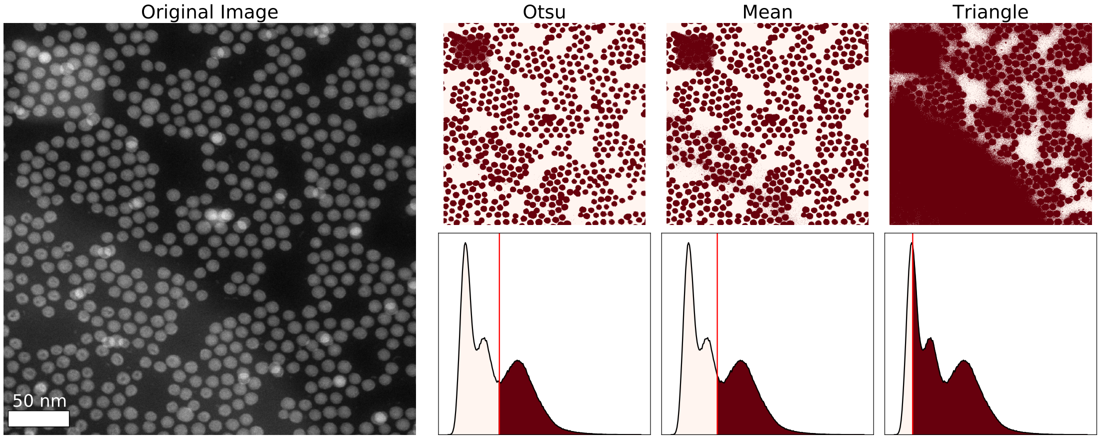

Figure 2.3: Demonstration of histogram-based thresholding on STEM image of semiconductor nanoparticles.

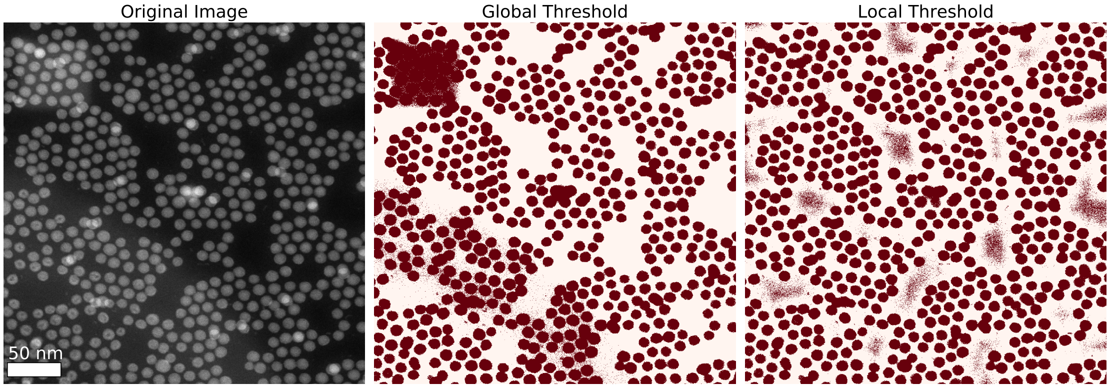

Figure 2.4: Demonstration of local thresholding on STEM image of semiconductor nanoparticles, compared to global thresholding. The local threshold avoids the artefact in the upper left corner present in the global threshold image.

2.6 Machine Learning

Machine learning can be roughly grouped into two categories, supervised and unsupervised. The key difference between the two flavors of machine learning is that supervised machine learning uses pre-labeled data to tune the parameters of the model. Machine learning models which aim to classify new data based on training data fall into the supervised learning category. While supervised machine learning models are important and ubiquitous in modern society, they are not used in this thesis.

In unsupervised learning, there is no ground truth and the researcher must tune the model and pre-treatment of data to achieve the desired results. Unsupervised learning is not an automatic process but rather an iterative process of discovery that involves trial and error to gain insight and knowledge from complex data. The two types of unsupervised learning used in this thesis are multivariate statistical analysis (MVA) and cluster analysis.

2.7 Multivariate Statistical Analysis (MVA)

The following three sections were written in conjunction with Alex Zettl and are part of a publication in the process of being written, hence the use of "we" and "our" throughout.

One of great challenges of scientific discovery is separating the wheat from the chaff, i.e. knowing which interactions and observational inputs might be relevant and which not. To keep things tractable and computationally manageable, researchers strive for a simplified model, which then guides further inquiry. Figure 2.5 shows schematically this traditional model-driven sequential approach to experimental scientific discovery. Once a trial model is formulated (often by a combination of intuition, inspiration, experience, and perhaps luck), it is tested via appropriate experiment and analysis.

To avoid data overload, model-specific filtering is applied to the data collection input channels, and highly model-specific data treatment and analysis follow (after all, wasting time and computational power collecting "useless" data or performing the "wrong" analysis is not desirable). If, after the analysis, the model fully fails, it is discarded. If the model

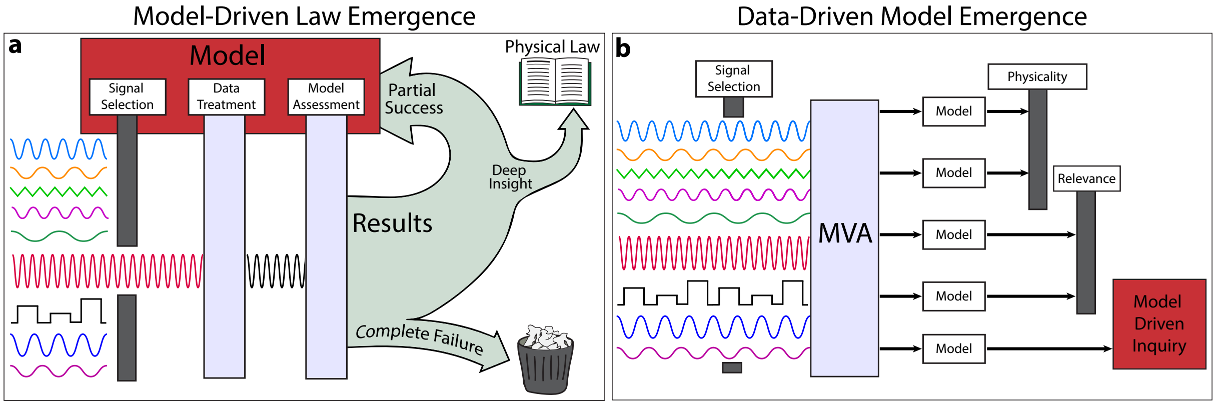

Figure 2.5: Overview of the model-driven approach versus the data-driven approach to scientific inquiry. (a) Flow chart for traditional model-driven law emergence. Experiments are performed using model-dependent bandwidth constrained signals. The incoming data are further filtered and analyzed in a model-dependent manner. The model is assessed and is either completely discarded (and a new model chosen) or refined. The cycle is repeated until data and model are consistent. Ideally, deep insight and a physical law are produced. (b) Flow chart for data-driven model emergence. Here, experiments are designed such that they collect the widest band of signals with no model-dependent data throttling. The data sets are rapidly statistically analyzed using Multivariate Statistical Analysis (MVA). MVA suggests possible models that may be discarded for physicality and relevance. Deep insight and physical laws may be immediately at hand, or the emergent model can serve as a refined trial model in the traditional approach. The data-driven approach immensely streamlines the overall scientific discovery process.

partially succeeds, it is refined and re-tested, possibly with modification of the data input channels. Ideally, after enough cycles or iterations, a suitably deep understanding of the system is gained and a physical law may emerge. More efficient data collection and analysis methods help move this serial and lossy cycle along, but initial formulation of the test model is often the bottleneck.

Fig. 2.5(b) shows schematically the data-driven approach. No model is assumed *a priori*. Rather than restricting data input, all available input channels are collected at the outset. The incoming data sets are fed into the analysis and models self-emerge. The set of models is reduced, filtering for physicality and relevance according to the questions being asked. In some cases the emergent models may already be suitably refined to provide deep understanding, or they can provide critical input to the complementary model-driven cycle of inquiry. Ideally, meaningful results of the data-driven process are obtained virtually in real time during the experiment.

The great power of the data-driven method is the ability to quickly assess large, multidimensional scientific datasets. The ubiquity of computers with high storage and memory capacity, as well as advancements in sensor technology, enable massive parallelization. Hyperspectral imaging (HI) leverages this computing and sensor power. The data-driven approach borrows tools from contemporary information theory and statistics to discriminate which data might be useful and which not. Throughout this thesis multivariate statistical analysis (MVA) is used to quickly decompose datasets into a basis whose members have the highest information density. MVA effectively generates a set of possible models based on the statistical properties of entering data.

2.8 Principal Component Analysis (PCA)

For concreteness (and no loss in generality) we consider 2x2 dimensional input datasets (2 spatial, 2 spectral dimensions). We first decompose the data into a new basis using Principal Component Analysis (PCA). The Principal Components (PCs) are orthogonal and describe which parts of the data contain the most variance. The first PC accounts for the most variance in the data, the second PC accounts for the second most variance, and so forth. The PC basis is constructed from the data covariance matrix, $\mathbf{C}(\mathbf{k})$, given by:

$$\mathbf{C}(\mathbf{k}) = \sum_{\mathbf{x}} \left(\mathbf{D}(\mathbf{x},\mathbf{k}) - \bar{\mathrm{D}}(\mathbf{k})\right)\left(\mathbf{D}(\mathbf{x},\mathbf{k}) - \bar{\mathrm{D}}(\mathbf{k})\right)^{\mathbf{T}}. \tag{2.5}$$

$\mathbf{D}$, the as-acquired data set, is a function of two spatial directions ($\mathbf{x}$) and two spectral dimensions ($\mathbf{k}$), $\bar{\mathrm{D}}(\mathbf{k})$ is the mean over the spatial dimensions, and $\mathbf{T}$ denotes the matrix transpose. The PC basis vectors, $\mathrm{P}_\alpha(\mathbf{k})$, are the eigenvectors of $\mathbf{C}$. In the PC basis, the data are represented as:

$$\mathbf{D}(\mathbf{x},\mathbf{k}) = \sum_{\alpha=1}^{N} a_\alpha(\mathbf{x})\mathrm{P}_\alpha(\mathbf{k}) \tag{2.6}$$

where a_α are the spatially varying weight coefficients and N is the dimension of the raw data. N is either the total number of spatial pixels or total number of spectral pixels, whichever is smaller. Traditionally, the weights (which, in the examples to be discussed below, are real-space images) are called the PC loadings, and the PCs (which, in the examples to be discussed below, are diffraction patterns) are called the PC factors. Equation 2.6 is reminiscent of Fourier decomposition, and the PCA decomposition indeed has qualitatively similar features (for example, the first few components describe longer wavelength features).

The decomposition in equation 2.6 is exact when the sum extends fully to N, the full size of the dataset. A fundamental feature of PCA is that a data set can be described to a high degree of precision by retaining only $N' \ll N$ components. It is assumed that the most important parts of the data (those with the highest variance) reside in the earlier components, while the later components contain primarily high-frequency noise, very similar to Fourier decomposition and compression. In this case the reconstructed model of the data, $\mathbf{M}_{PCA}$, is given by:

$$\mathbf{M}_{PCA}(\mathbf{x}, \mathbf{k}; N') = \sum_{\alpha=1}^{N'} a_\alpha(\mathbf{x}) \mathrm{P}_\alpha(\mathbf{k}). \tag{2.7}$$

The number N' can be estimated using a variety of metrics. Our procedure is to identify the N' that yields a root mean square reconstruction error (RMSE) equal to the noise floor of the relevant measurement. The mean square reconstruction error (MSE), is given by:

$$e_M^2 = \frac{1}{\mathrm{N}_\mathbf{x} \mathrm{N}_\mathbf{k}} \sum_{\mathbf{x},\mathbf{k}} \left| \mathbf{D}(\mathbf{x}, \mathbf{k}) - \mathbf{M}_{PCA}(\mathbf{x}, \mathbf{k}; N') \right|^2 = \frac{1}{\mathrm{N}_\mathbf{k}} \sum_{\alpha=N'+1}^{N} \lambda_\alpha \tag{2.8}$$

Here λ_α are the eigenvalues of the data covariance matrix ($\mathbf{C}$), $\mathrm{N}_\mathbf{x}$ and $\mathrm{N}_\mathbf{k}$ are the number of spatial and spectral pixels, $\mathbf{D}$ is the data set, and $\mathbf{M}_{PCA}$ is the reconstructed PCA model. The last expression in equation 2.8) can be quickly calculated for all values of N' and is used to determine the cutoff for the PCA decomposition. This decomposition can be used for lossless data compression and storage when N' is chosen such that the RMSE is equal to the noise floor. The resulting data representation has increased signal to noise and decreased data size with the same information content.

The principal components are orthogonal and thus, in general, do not necessarily describe physical processes.

2.9 Independent Component Analysis (ICA)

The next step of the analysis is to use Independent Component Analysis (ICA) to perform Blind Source Separation (BSS). BSS adopts the conjecture that if signals are from distinct physical processes, those signals will be statistically independent. The crux of the method is the reasonable (but logically unwarranted) assumption that this conjecture can be reversed; namely, BSS assumes that if signals are statistically independent, then they originate from different physical processes.

Two signals, X and Y, are uncorrelated if $\langle XY\rangle = \langle X\rangle\langle Y\rangle$ where the brackets denote the expectation value. Two signals are statistically independent if $\langle X^pY^q\rangle = \langle X^p\rangle\langle Y^q\rangle$ for all positive integers p and q. Statistical independence is related to correlation but is a stronger condition. For example, the x and y coordinates of a body in uniform circular motion are uncorrelated but not statistically independent.

The goal of ICA is to un-mix a set of components into a new basis that has maximal statistical independence. We use the PCA loadings (real space images) as the set of components for separation. In ICA, the model of the data is given by:

$$\mathbf{M}_{ICA}(\mathbf{x}, \mathbf{k}; N'') = \sum_{\alpha=1}^{N''} c_\alpha(\mathbf{k}) I_\alpha(\mathbf{x}). \tag{2.9}$$

where $\mathbf{M}_{ICA}$ is the new ICA model which is again a function of two spatial directions $\mathbf{x}$ and two spectral dimensions $\mathbf{x}$,$c_\alpha(\mathbf{k})$ are the spectrally varying weight coefficients, $I_\alpha(\mathbf{x})$ are the spatially varying independent component maps, and N'' is the reduced dimension of the independent component space. Each new independent component is constructed as a linear combination of principal components,

$$I_\alpha(\mathbf{x}) = \sum_{\beta=1}^{N'} w_{\alpha\beta} a_\beta(\mathbf{x}) \tag{2.10}$$

where $a_\beta(\mathbf{x})$ are the principal component loadings and $w_{\alpha\beta}$ are entries of the mixing matrix. The FastICA algorithm is a reliable method to efficiently determine the mixing matrix, which gives the set of independent components that have maximal statistical independence from one another.

After the mixing matrix has been computed using FastICA, the complementary k-space independent components $c_\alpha(\mathbf{k})$ are easily determined from:

$$c_\alpha(\mathbf{k}) = \sum_{\beta=1}^{N'} w_{\alpha\beta} P_\beta(\mathbf{k}) \tag{2.11}$$

The independent components of Eqs. 2.10 and 2.11 underpin the model emergent from the original experimental data, and as such provide a method to rapidly examine the major features of a large, high-dimensional data set.

2.10 Non-Negative Matrix Factorization (NMF)

Non-negative matrix factorization (NMF) is a popular flavor of MVA, particularly for decomposition of 3D hyperspectral data (*e.g.* Scanning PL, EELS, EDS, and CL). NMF decomposes the data into a new basis, with the constraint that the resulting components contain only positive values [23, 24, 25]. This non-negative constraint makes the decomposition particularly appealing as the resulting components lend themselves to easy physical interpretation. For concreteness, NMF is discussed here in the context of 2+1 dimensional spectral image data, but the formalism presented here can be easily generalized to any number of dimensions.

NMF assumes that a dataset $\mathbf{D}(\mathbf{x}, \varepsilon)$ can be factorized into a reduced set of spectral weight components, $\mathbf{W}(\varepsilon)$, multiplied by a reduced set of spatial abundances, $\mathbf{H}(\mathbf{x})$, with a residual noise component, $\mathbf{R}(\mathbf{x}, \varepsilon)$, in the following way (see figure 2.6 for illustration):

$$\mathbf{D}(\mathbf{x}, \varepsilon) = \mathbf{W}(\varepsilon)\mathbf{H}(\mathbf{x}) + \mathbf{R}(\mathbf{x}, \varepsilon) \tag{2.12}$$

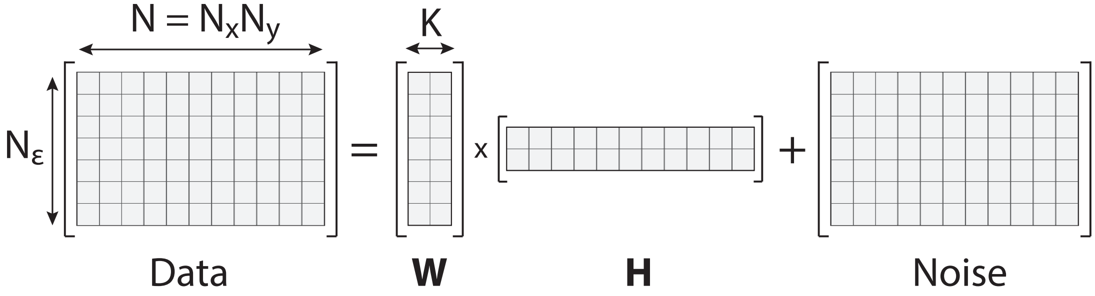

Figure 2.6: Illustration of NMF decomposition. The original data is unraveled into a matrix where the columns are spectra and the rows are spatial locations of size $N_\varepsilon \times N_x N_y$. This matrix is factorized into two matrices with a reduced number (K) of rows (columns) along with a residual component.

The data is unraveled into a 2D matrix such that the columns are spectra and the rows are spatial locations. When the decomposition is complete, each row of $\mathbf{H}$ is reshaped to reconstruct an image. NMF is generalized to a higher number of dimensions in a similar way by placing all measured variables into the columns and all observations of these variables into the rows of the 2D matrix $\mathbf{D}$.

The number of components, K, is a free parameter and must be chosen by the user. Determination of this number is made in the same way as described for PCA and ICA.

The factors are found numerically by minimizing the cost function:

$$C = \big|\big|\mathbf{D}(\mathbf{x}, \varepsilon) - \mathbf{W}(\varepsilon)\mathbf{H}(\mathbf{x})\big|\big|_F \tag{2.13}$$

where $||...||_F$ denotes the Frobenius norm,

$$\big|\big|\mathbf{A}\big|\big|_F = \sqrt{\sum_{i,j} a_{ij}^2} \tag{2.14}$$

and $\mathbf{W}(\varepsilon)$ and $\mathbf{H}(\mathbf{x})$ are subject to the constraints of normalization and non-negativity of all elements:

$$\begin{gathered} w_{mk} \geq 0 \,, h_{kn} \geq 0 \\ \sum_{k=1}^{K} h_{kn} = 1 \end{gathered} \tag{2.15}$$

The primary drawback of NMF is that convergence is slow and the complexity of matrix factorization scales linearly with the number of data points. Decomposition of a data set with N spatial pixels and N_ε spectral pixels into K components runs in $\mathcal{O}(NN_\varepsilon K)$ time,

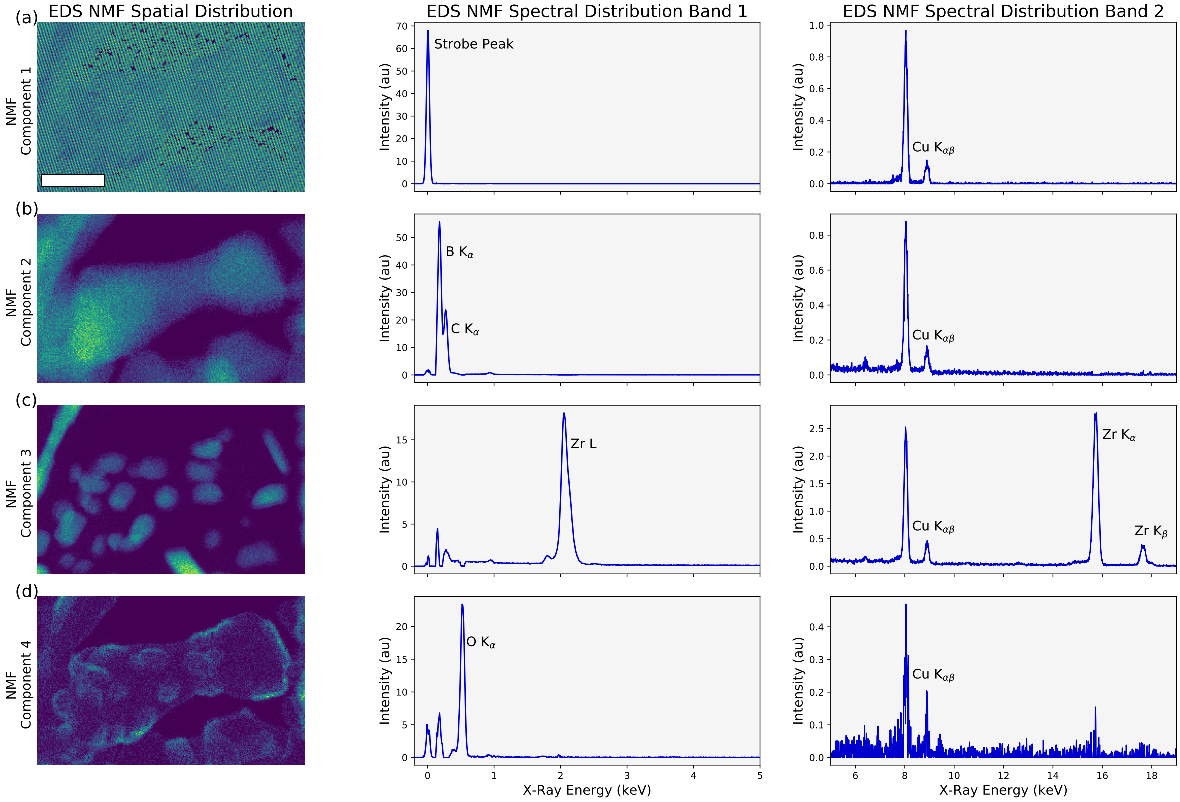

Figure 2.7: NMF decomposition of EDS characterization data from Zirconium-Boron ceramic aerogels. NMF separates the spectral data into 4 distinct components. The first component is composed of a peak centered at 0 eV which originates primarily from the readout noise of the detection electronics. The second component shows that bulk of the material is a boron and carbon matrix. The third component consists of small phase-segregated zirconium particles with no appreciable boron or oxygen. The final component shows that the majority of the oxygen in the sample is concentrated at the surfaces of the matrix and nanoparticles. A peak from copper is present in all spectra due to the copper TEM grid used to support the sample.

although slightly faster algorithms do exist [26]. For this reason, NMF is best suited to small to medium-sized data sets.

A key example of NMF appears in Chapter 5, where hyperspectral CL data is decomposed to show the spectral contribution of distinct physical processes. NMF is also used extensively in quickly assessing EDS spectral maps of ceramic aerogel materials synthesized by Marcus Worsley and Sally Turner. An example of how NMF is used as a feedback mechanism for synthesis is shown in figure 2.7. The spectral components pictured clearly show that the synthesis was not successful, and that the precursor materials are phase segregated into zirconium nanoparticles and a boron and carbon matrix.

2.11 Image Featurization

When classifying images, how to represent the images to the computer must be taken into consideration. This process is called featurization. In general, this process serves to reduce the image from an $N_x \times N_y$ array to a one-dimensional array of length $N' \ll N_x \times N_y$. The one-dimensional array is called the feature vector of an image.

Constructing feature vectors is the most time-consuming part of computer vision. Many algorithms exist that automatically construct features based on edges that are invariant under translation, scale, rotation, and other geometric transformations. In the work presented here, the feature vectors are generally much simpler and are constructed in such a way that each feature can be simply explained.

PCA Features

Image featurization is essentially a problem in dimensional reduction, one of the hallmark applications of MVA techniques. The PCA or ICA coefficients (equations 2.6 or 2.9) are often used as a feature vector for the classification of images. Results using this technique are shown in section 2.16.

Structural Similarity Index (SSIM)

The aptly named structural similarity index (SSIM) is a metric of similarity between two images. The SSIM between images, I_1 and I_2 is:

$$\mathrm{SSIM}(I_1, I_2) = \frac{(2\mu_1\mu_2 + c_1)(2\sigma_{12} + c_2)}{(\mu_1^2 + \mu_2^2 + c_1)(\sigma_1^2 + \sigma_2^2 + c_2)} \tag{2.16}$$

Here, μ_i is the average of I_i, σ_i^2 is the variance of I_i, σ_{12} is the covariance between I_1 and I_2, and c_i are small constants to stabilize the output for small divisors.

The SSIM is useful for clustering (see section 2.12) a set of images into groups. The feature vectors are constructed by calculating a matrix of SSIM values, $\mathbf{S}$, where S_{ij}, is the SSIM of images i and j. The final feature vectors for image i is the ith column of $\mathbf{S}$.

Image Moments

Image moments are a convenient and intuitive representation of images in a greatly reduced parameter space. The entries in the raw image moment matrix, $\mathbf{M}$, of an image, $I(x, y)$ are:

$$M_{pq} = \sum_{x,y} x^p y^q I(x, y) \tag{2.17}$$

A set of related quantities, the central moments, have more useful symmetry properties than the raw moments. The entries in the central moment matrix, $\boldsymbol{\mu}$, are:

$$\mu_{pq} = \sum_{i,j} (x - \bar{x})^p (y - \bar{y})^q I(x, y) \tag{2.18}$$

where $\{\bar{x}, \bar{y}\} = \{M_{10}/M_{00}\, M_{01}/M_{00}\}$.

Linear combinations of central moments can be constructed that are invariant with respect to translation, rotation, and scale. These combinations of central moments, called the Hu moments [27], are useful for creating feature vectors for grouping images with similar symmetry properties. The Hu moments are used as the feature vectors for clustering ICA diffraction pattern components from 4DSTEM data of TMD polycrystalline thin-films in section 7.4.

2.12 Feature Clustering

Clustering is the process of grouping a set of feature vectors such that vectors in the same group, or cluster, are more similar to each other than to those in other clusters. Clustering can be achieved using numerous algorithms, each with different metrics of what constitutes a cluster, such as minimizing distance between cluster members or aiming for a specific statistical distribution within each cluster. The two types of clustering procedures used in the thesis are discussed below.

K-Means

The K-Means algorithm [28] clusters data by trying to separate data points into groups of equal variance, minimizing the within-cluster sum-of-squares (WCSS), also called the inertia. K-Means divides the data, $\mathbf{X} = \{\mathbf{x}_1, \mathbf{x}_2, \mathbf{x}_3, ..., \mathbf{x}_N\}$ into K clusters, $C = \{C_1, C_2, ..., C_K\}$. Each cluster is parameterized by its mean, or centroid, $\boldsymbol{\mu}_{C_i}$. The clusters are determined by minimizing the total squared Euclidean distance between the points in each cluster and the cluster centroid.

$$\text{WCSS} = \sum_{C_i}^{K} \sum_{j}^{N_i} \left|\left|\mathbf{x}_{ij} - \boldsymbol{\mu}_{C_i}\right|\right|^2 \tag{2.19}$$

Figure 2.8 illustrates the results of K-Means for a simple data set. K-Means is used in chapter 5 to sort light emitting defects in h-BN, identified using automatic peak detection. An in-depth look at this procedure is presented in section 2.16.

Affinity Propagation

Affinity propagation is a clustering routine that operates by sending "messages" between pairs of data points [29]. Messages are sent between data points until a set of *exemplars* are found. The exemplars are data points that are representative of each cluster as a whole, similar to the cluster means from K-Means clustering. Unlike K-Means, Affinity Propagation does not assume the number of clusters is known. The algorithm has the favorable property of automatically detecting the optimum number of clusters.

The algorithm takes as input a collection of similarities between data points, where the similarity, $s(i, k)$, indicates how well the data point with index k is suited to be the exemplar for the data point with index i. Usually the similarities are set to be the negative squared Euclidean distance between points ($s(i, k) = -||\mathbf{x}_i - \mathbf{x}_k||^2$). Messages are sent between pairs of samples until convergence (when the number of clusters does not change after multiple iterations).

Figure 2.9 illustrates the results of Affinity Propagation for a simple data set. Affinity Propagation is used in chapter 7 to sort ICA diffraction pattern components extracted from 4DSTEM data from polycrystalline TMD thin films.

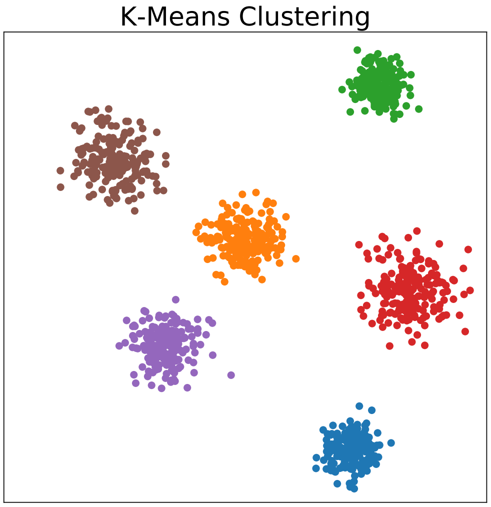

Figure 2.8: Illustration of K-Means clustering. The colors show which data points belong to the same cluster, as determined by the K-Means algorithm.

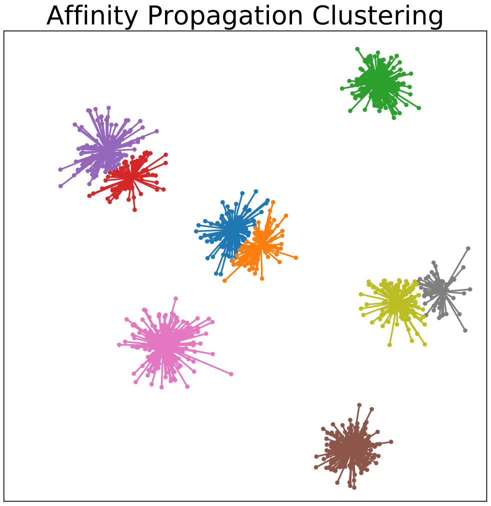

Figure 2.9: Illustration of Affinity Propagation clustering. The colors show which data points belong to the same cluster, with the lines joining the data to the cluster exemplars.

2.13 Applications: Determining Nanoparticle Size Distributions

Metallic [30] and semiconducting [31] nanocrystals (NCs) display strong, size-dependent optical and electronic properties due to quantum confinement of the electronic wavefunctions [32]. Tuning and harnessing these size-dependent material properties requires synthetic routes to prepare nanometer-size crystals that are monodisperse in terms of size, shape, internal structure, and surface chemistry. Recent advances in NC synthesis have enabled atomic-scale control of composition, size, size dispersion, shape, and crystal structure of the resulting colloids [33].

Accurate determination of NC size is an essential step in the iterative process of developing a new synthetic routine or designing a new experiment that leverages the flexible nature of NC optical and electronic properties. STEM imaging allows for the rapid acquisition of images of a statistically significant number of individual NCs in a very short period of time. Automated data analysis techniques for such image data enables high-throughput NC discovery, synthesis, and experiments.

Figure 2.10 shows the basic workflow of the measurement. First, a series of STEM images are collected for each synthetic run of NCs. STEM is an excellent imaging mode for these experiments because of the intuitive contrast mechanism and enhanced Z-contrast. Next, each STEM image is thresholded to create a binary image of connected regions that represent the individual nanoparticles. Each connected region can then be labeled and extracted, and the size of the region can be determined. Finally, a size distribution histogram is created using the extracted data to accurately determine the nominal NC size and degree of monodispersity.

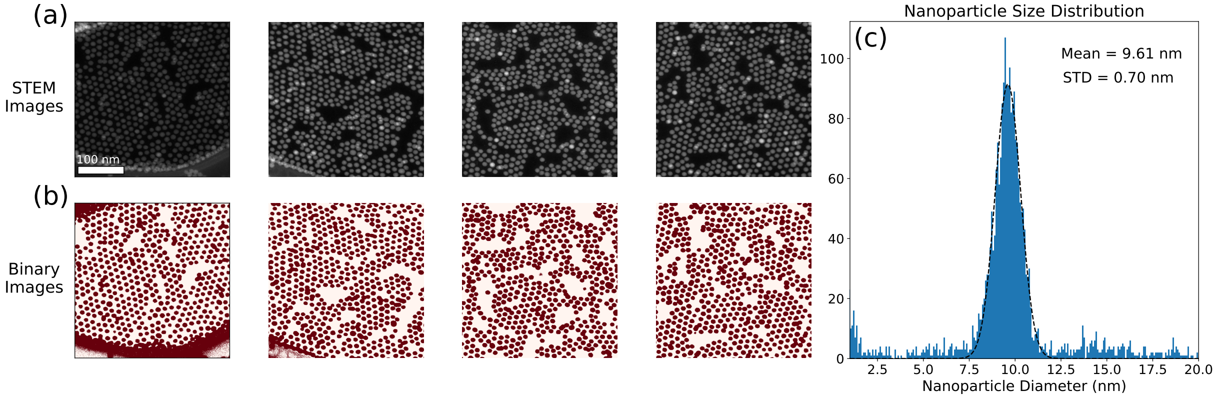

Figure 2.10: Determination of nanoparticle size distribution using image thresholding and region segmentation. The STEM images in (a) were automatically thresholded using the Otsu method to produce the binary images in (b). Each connected region from the binary images was extracted and the equivalent diameter of the region was measured to create the size distribution histogram in (c).

2.14 Applications: Morphology of Nanoparticle Superlattices

The figure presented here appeared in the article "Long-Range Order in Nanocrystal Assemblies Determines Charge Transport of Films" in *ACS Omega* [34]. In this work, a novel method to fabricate PbS nanocrystal (NC) solids and FET devices is presented. Important aspects of this work were determining which routes produced glassy (disordered) NC solids, which produced NC superlattices (ordered), and characterizing relevant material properties of each type.

Like atoms or molecules, NCs may be used as the building blocks of condensed matter systems, leading to emergent and collective phenomena not seen in the individual constituents of the system. Controlled manipulation of NCs into glassy and ordered solids is possible [32], opening up the possibility of fabricating new solid-state materials and devices with novel physical properties.

Figure 2.11 shows a simple procedure for clearly visualizing the size of superlattice (SL) domains in these materials. The TEM image in 2.11(a) contains all of the relevant information, but does not visually convey that information in a clear way. A small pass band is masked over the peaks in the FFT for different SL orientations (figure 2.11(a), inset) and a forward Fourier transform of the masked FFT is taken. False color is applied to the forward transform images and they are recombined, creating a clear visualization of SL domains (2.11(b)).

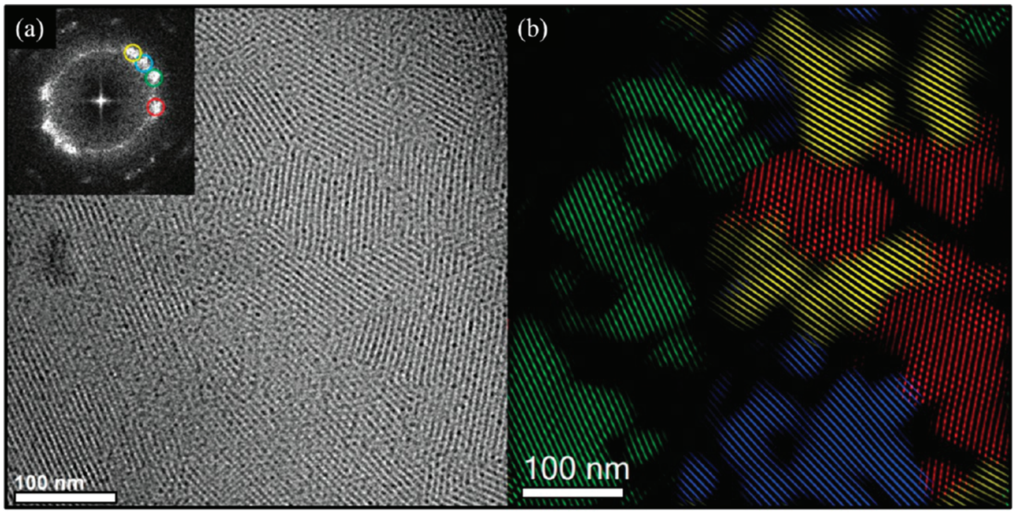

Figure 2.11: Superlattice (SL) domains in a PbS ordered nanocrystal solid. Panel (b) shows a false-color composite image of (a) made by masking the colored circles in the FFT (inset). The false-color image illustrates the typical domain size of ∼100 nm observed in the SL membranes.

2.15 Applications: Unit Cell Averaging of Filled Carbon Nanotubes (CNTs)

Recent work in the Zettl group has focused on confining quasi-1D chain materials and 2D material nanoribbons inside of nanotubes [35, 36]. When confined, these materials display new properties such as torsional waves, metal-insulator transitions, and new crystalline phases. Identification of the material phase is a challenging imaging problem due to the small number of atoms present in the specimens and instability of nanostructures under the electron beam.

Figure 2.12(a) shows a HRSTEM image of carbon nanotubes filled with HfTe material. An unexpected segmented unit cell was observed in the data. In order to identify the locations of each atomic species in the new structure, unit cells were automatically extracted from ~ 50 STEM images and averaged to create a high-fidelity image of the new structure.

The STEM images were first rotationally aligned so that all nanotubes were parallel. Then, a candidate unit cell was manually identified and extracted. Cross-correlation was run between the template and all images. Peaks in the cross-correlation image were detected and a threshold was set to discriminate between true matches and false-positives. Each matching unit cell was automatically extracted and the matches were averaged together, resulting in the high signal to noise image.

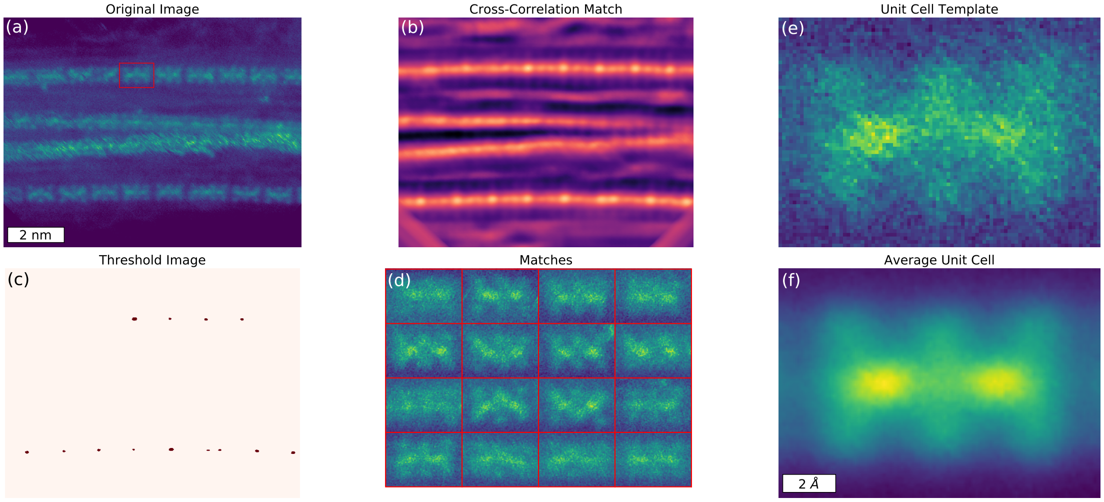

Figure 2.12: Unit cell averaging using STEM images of HfTe chain materials, confined inside of carbon nanotubes. Images from this synthesis showed the presence of a new type of unit cell and ordering in the material.

2.16 Applications: Detecting and Clustering Light-Emitting Color Centers in h-BN

This section is derived from work done as part of a paper published in *Physical Review B*, titled "Blue-Light-Emitting Color Centers in High-Quality Hexagonal Boron Nitride" [37], based on work done as part of my Ph.D. research at the Molecular Foundry. The scientific consequences of this analysis are presented in Chapter 5.

Figure 2.13 shows an overview of the time series image data in which the features of interest appear as bright spots on a dark background. The features were automatically detected using the difference of Gaussians (DoG) blob detection method. DoG works by applying a series of Gaussian filters with increasing standard deviations to each image and stacking the results into a data cube. Local maxima in this cube were tagged as potential features of interest.

As seen in the top row of figure 2.13 (a-c), There were many false-positive peaks identified in the extended line-like feature that runs through the images. The inclusion of this data in

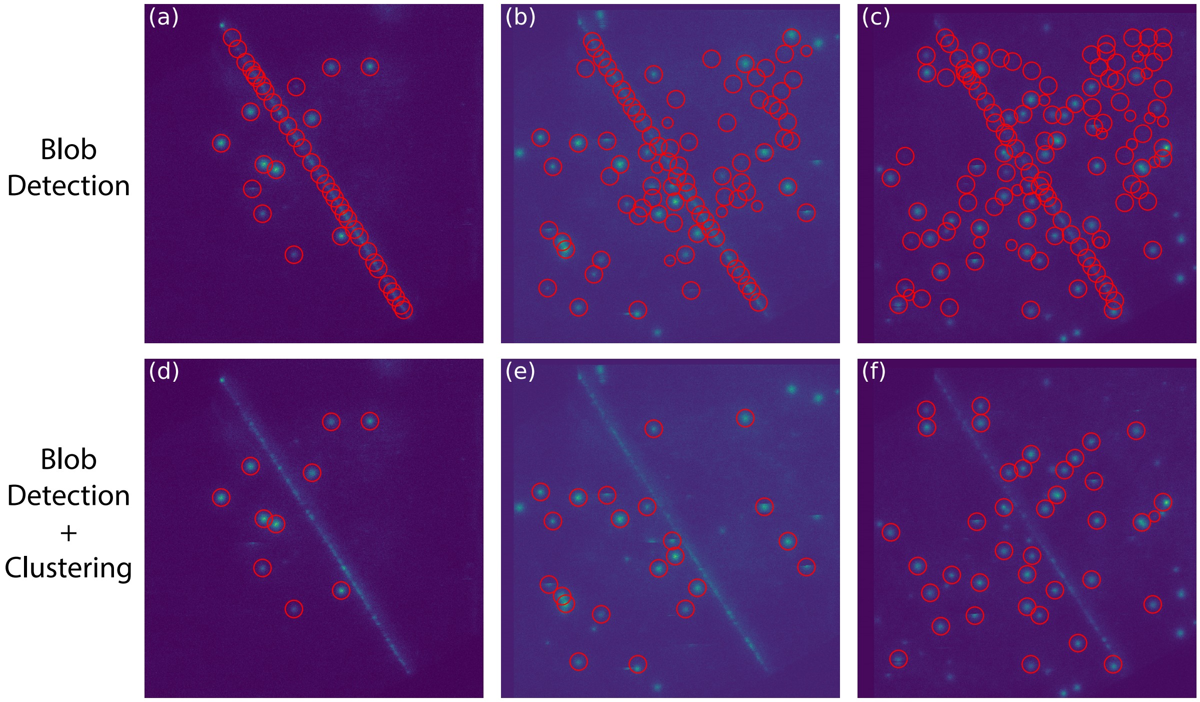

Figure 2.13: Automatic blob detection of light-emitting color centers in hBN with and without cluster filtering. The top row of images (a-c) show the detected blobs in the raw data (red circles) for three images in a set of time series data. The bottom row (d-f) shows the same images, but with with the detected blobs filtered using clustering to remove blobs that result from the extended line-like features and from false-positives.

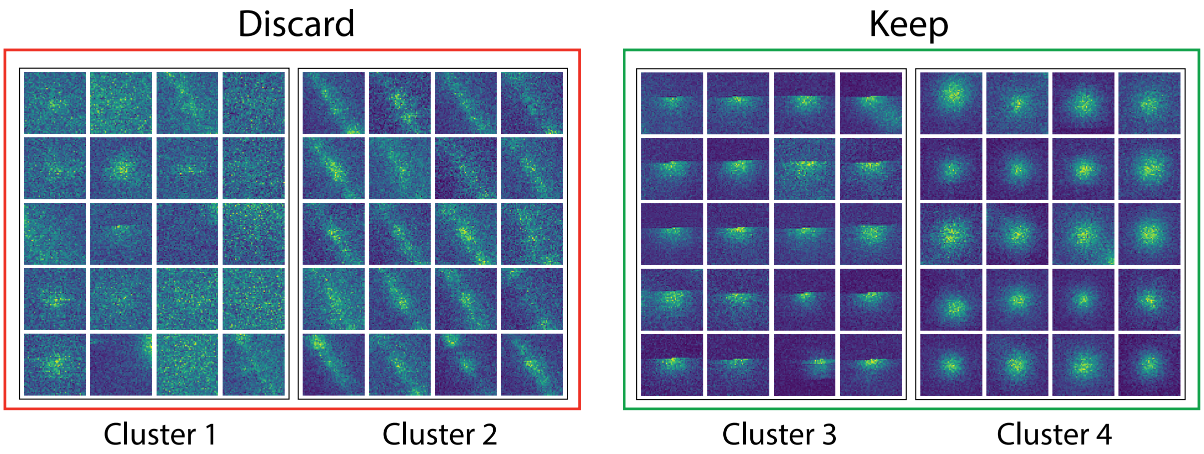

Figure 2.14: Clustering of extracted light-emitting color centers. K-means clustering allows for the easy removal of spuriously detected blobs from extended features and noise. Clustering is also able to separate the emitters into those that are on for the entire image and those that blink on mid-scan.

the analysis would have lead to incorrect results (the number of bright spots as a function of time).

In order to remove these false positives, a clustering analysis was performed on all extracted emitters using blob detection. First, each detected emitter was extracted from the parent time series data as a 50x50 pixel image. PCA decomposition was performed on these images and the first 50 PCA coefficients were used as the feature vector for the clustering analysis. The features were first grouped into six clusters using K-Means.

Inspection of the results revealed that the cluster with the most members was almost entirely composed of peaks from the extended feature, shown in figure 2.14. These emitters were then removed from the analysis and the analysis process was repeated. For the second iteration, 25 PCA coefficients were used as the feature vectors and the features were grouped into three clusters. Figure 2.14 shows the final results of the clustering analysis.

Inspection of the final clusters, shown in 2.14, reveals that PCA-enabled K-Means clustering is able to automatically group the data into four relevant classes of emitter. Members of the first group appear as either very faint emitters or random noise. Members of the second group were false positives from the previously mentioned line-like feature. The first and second group was omitted from further data analysis.

Groups 3 and 4 revealed that there are two distinct types of emitter in the data set, those that remain in the emissive state for the entire scan, which appear as bright disks, and those that turn on or off during the scan, appearing as truncated disks.

The final results of the peak detection with clustering is shown in the bottom of figure 2.13 (d-f). The number of peaks in each image was used to show that the number of light-emitting features scales linearly with exposure to the electron beam.

2.17 Applications: Counting Atoms in HR-STEM Images

This section is derived from work done as part of a paper published in *Physical Review B*, titled "Tunable Electronic Structure in Gallium Chalcogenide van der Waals Compounds", based on work done in collaboration with the MAESTRO group at Advanced Light Source at Lawrence Berkeley National Lab [38]. The scientific consequences of this analysis are presented in chapter 8.

In this research, atomic resolution HRSTEM data was acquired from a series of alloys of layered Gallium Sulfide Selendide $\mathrm{GaS}_x\mathrm{Se}_{1-x}$ materials. Atomic columns were automatically identified by first applying a 3×3 median filter followed by a Gaussian filter ($\sigma = 2$ pixels) to remove noise. Then atomic columns were detected using a local maximum filter with in a 10×10 neighborhood. A 40×40 region around each detected peak was extracted and the intensity distribution was fit to the following 2D elliptic Gaussian function.

$$I(x,y) = A\exp(-a(x-x_0)^2 - 2b(x-x_0)(y-y_0) - c(y-y_0)^2) + B$$

$$\begin{pmatrix} a & b \\ b & c \end{pmatrix} = \begin{pmatrix} \cos(\theta) & \sin(\theta) \\ -\sin(\theta) & \cos(\theta) \end{pmatrix} \begin{pmatrix} 1/2\sigma_x^2 & 0 \\ 0 & 1/2\sigma_y^2 \end{pmatrix} \begin{pmatrix} \cos(\theta) & -\sin(\theta) \\ \sin(\theta) & \cos(\theta) \end{pmatrix} \tag{2.20}$$

Here, x_0 and y_0 are the center coordinates for the distribution, σ_x and σ_y are the standard deviation along the major and minor axis, θ is the angle of rotation, A is the Gaussian amplitude, and B is a constant offset. The coefficients (a, b, and c) in the matrix on the left are obtained from matrix multiplication of the three matrices on the right.

The results of this routine are presented in figures 2.15 and 2.16 for two representative alloys. This analysis gave the crucial insight that for each of the alloys, there is no appreciable ordering of S and Se atoms in the basal plane of the material, indicating that the alloys form a solid solution. This is evidenced by the fact that the amplitude and standard deviations of each fit are approximately normally distributed in figure 2.15.

From a cursory glance at figure 2.16, it might be concluded that there is in-plane ordering for this alloy. However, a closer analysis reveals that these two alloys have different stacking configurations (see section 8.4). A two Gaussian fit to the amplitude histogram shows that there are approximately twice as many dim atomic columns compared to bright atomic columns. Inspection of the unit cell reveals that there are twice as many atoms in the A sites as in the B sites.

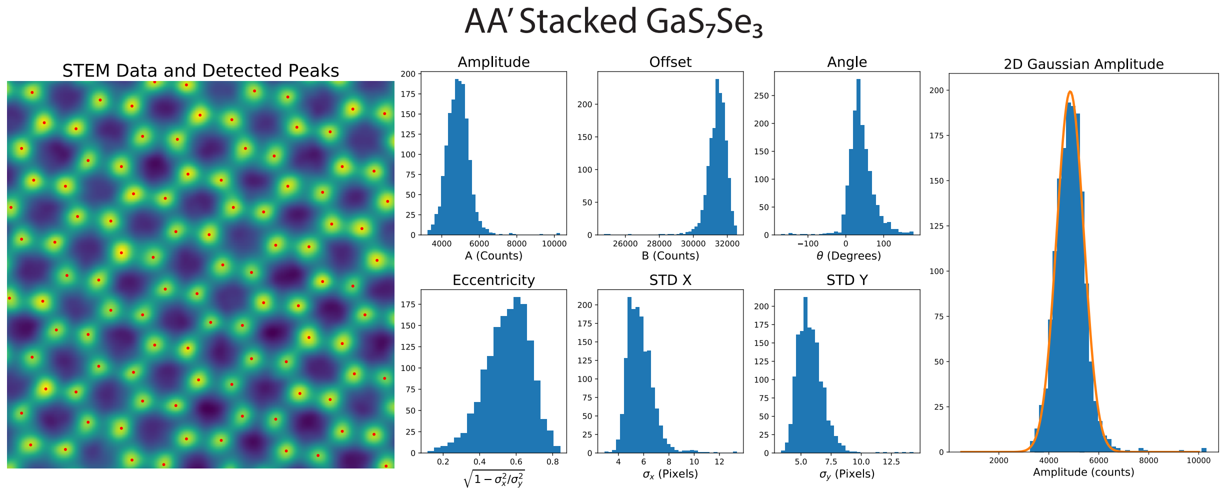

Figure 2.15: Detection and quantification of atomic columns in HRSTEM data from Gallium Sulfide Selendide alloys (GaS_7Se_3). The leftmost panel shows an HRSTEM image with detected peak location overlain as red dots. The intensity of each column was fit to a 2D Gaussian function; histograms of the fit parameters are shown in the middle. The rightmost panel shows a closer view of the fit amplitude histogram with an overlaid Gaussian distribution.

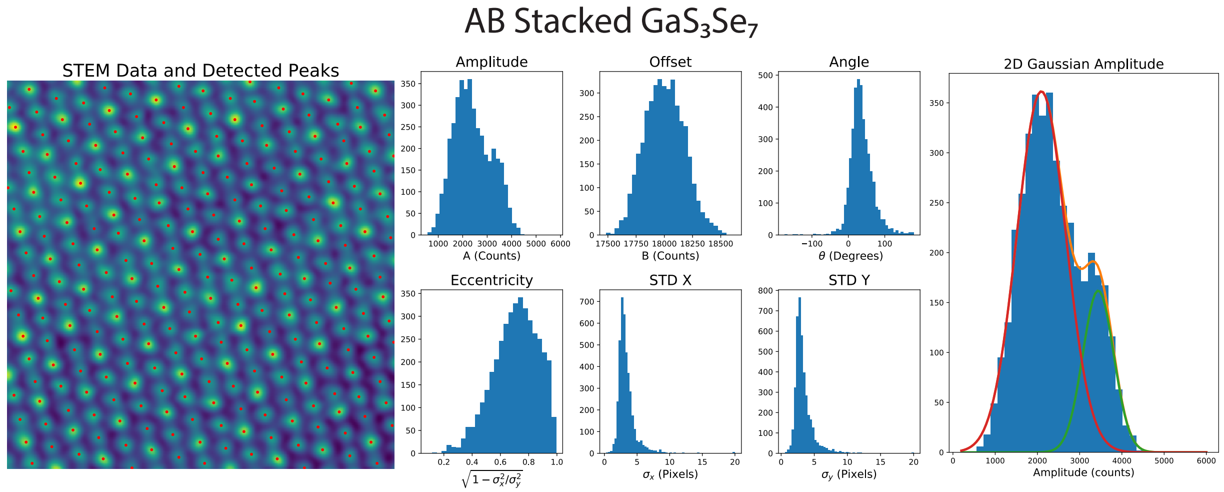

Figure 2.16: Detection and quantification of atomic columns in HRSTEM data from Gallium Sulfide Selendide alloys (GaS_3Se_7). The leftmost panel shows an HRSTEM image with detected peak location overlain as red dots. The intensity of each column was fit to a 2D Gaussian function; histograms of the fit parameters are shown in the middle. The rightmost panel shows a closer view of the fit amplitude histogram with an overlaid distribution composed of two Gaussians.

Chapter 3

Introduction to Hexagonal Boron Nitride

Nanoscience fun fact: carbon nanotubes, first observed in 1991, were named after their original discoverer: John Nanotubes.

3.1 Chapter Introduction

Hexagonal boron nitride (h-BN) is composed of stacked layers of sp^2 bonded boron and nitrogen (illustrated in figures 3.1 and 3.8). The intralayer bonding between adjacent atoms in a sheet is strong and ionic/covalent and the interlayer forces that couple adjacent sheets are weak and van der Waals. Adjacent layers can be stacked in several configurations (see section 3.4), but generally speaking, h-BN layers stack in the AA′ sequence, where the B (N) atoms in one layer have an N (B) directly above and below.

h-BN has remarkable mechanical, optical, thermodynamic, and electronic properties. It is a chemically inert, and atomically flat wide band gap semiconductor ($E_{gap} \sim 6$ eV), making it an excellent substrate for testing new physics in sensitive 2D material devices and an ideal encapsulation medium for air-sensitive 2D material devices [39, 40, 41]. Optically active defects inside of the band gap are of great interest (see chapters 4, 5, and 6) because they are single photon emitters, making h-BN a potential host material for optically addressable solid-state qubits [42, 43].

h-BN has many useful applications in a variety of industries. Due to the combination of high lubricity, high thermal conductivity, low electrical conductivity, chemical inertness, and low density, h-BN nanomaterials are promising for lubrication, heat shielding, and radiation shielding for aerospace applications. The cosmetics industry makes heavy use of h-BN in powder form because of its chemical inertness, high bio-compatibility, high lubricity, and optical transparency.

This chapter outlines the synthetic origin of the various h-BN polytypes studied throughout the thesis and presents original research related to each. The scientific results in this chapter are the product of collaborations with other members of the Zettl group, especially Matt Gilbert, Sally Turner, and Thang Pham. My supporting role in these projects was centered around imaging and characterization of materials and devices. The main thrust of my research on h-BN is presented in Chapters 5, and 6.

3.2 h-BN Polytypes: Bulk Crystals

Bulk h-BN Powder

Industrial scale production of h-BN powder generally uses a well-established synthetic route [44]. Boric acid and ammonia precursors react in the presence of a carrier substance at elevated temperature ($\sim$ 700 °C). After the reaction the carrier is leeched away with HCl and the remaining h-BN is washed with water. A second, higher temperature ($\sim$ 1500 °C) reaction with ammonia follows, resulting in h-BN powder of 0.1-0.5 μm thick platelets with lateral sizes of $\sim$ 5 μm. The resulting material is $\sim$ 97% pure.

High-Quality Bulk Crystals

A special high-pressure, high-temperature method is used to prepare h-BN single crystals with high-purity and large domain size [45]. h-BN powder, heated at 2100 °C for 2 hours under nitrogen flow (to drive off residual oxygen) is used as the growth precursor. Barium boron nitride ($Ba_3B_2N_4$) is used as a growth solvent. The precursor and solvent are combined in a dry nitrogen atmosphere (O_2 and H_2 concentrations < 1 ppm) and encapsulated in a molybdenum sample chamber. Then, the sample is compressed at 4 - 5 GPa and heated at 1500 - 1650 °C for 20 - 80 hours. The Mo sample chamber is then dissolved in hot aqua regia and the crystals are washed in DI water.

All high-quality h-BN used for the studies presented in this thesis was synthesized by K. Watanabe and T. Taniguchi at the National Institute for Materials Science (NIMS) in Tsukuba, Japan.

3.3 h-BN Polytypes: Chemical Vapor Deposition Grown Thin-Films

The material presented in the next three section is derived from research conducted in collaboration with several Zettl group members, most notably S. Matt Gilbert, Gabe Dunn, and Thang Pham. This section is adapted from two publications: "Fabrication of Subnanometer-Precision Nanopores in Hexagonal Boron Nitride", in *Scientific Reports* [46] and "Alternative Stacking Sequences in Hexagonal Boron Nitride", in *2D Materials* [47].

h-BN synthesized using chemical vapor deposition (CVD) has several markedly different properties than that grown using traditional methods. The resulting material can be grown much thinner than bulk material, as thin as a single monolayer. The layers of CVD grown h-BN stack in the AB sequence, different than bulk, which generally stacks in the AA′ sequence. This alternate stacking sequence slightly alters the optical properties of the material and allows for the controlled formation of nanopores with very precise sizes.

Few-layer h-BN is synthesized on copper and iron foils using low-pressure chemical vapor deposition (LP-CVD). Ammonia-borane powder was used as a stoichiometric B and N precursor, and a two-heating-zone system is used to separately control the temperatures of the solid precursor and transition metal catalyst. Prior to the LP-CVD process, the metal foil catalyst undergoes minimal pre-treatment. Copper foils are soaked in glacial acetic acid for 10 minutes, followed by rinsing with DI water. Iron foils are soaked for 10 minutes in acetone followed by rinsing with IPA and DI water.

The foil is annealed for 1-2 hours at low pressure with a flow of 100 sccm H_2 and 300 sccm Ar at 1025 °C for copper or 1100 °C for iron. After annealing, the argon gas flow is turned off, the hydrogen gas flow is set between 100-200 sccm, and 100 mg of ammonia-borane powder, loaded in a one-end sealed quartz tube upstream of the metal catalyst, is heated to 80 °C. The byproducts of the thermal decomposition of the ammonia-borane diffuse 6 inches before they are pushed downstream by the hydrogen carrier gas toward the transition metal foil. After 20-60 minutes of h-BN growth, the hydrogen flow is reduced to 10 sccm, the precursor is quickly cooled, and the metal foil is allowed to cool at a rate of $\sim$10 °C/min.

3.4 CVD h-BN Applications: Bernal Stacked h-BN

As mentioned previously, CVD grown h-BN tends to exhibit AB inter-layer stacking as opposed to the usually observed AA′ stacking sequence. This unique stacking order is caused by the copper foil used as a growth substrate for the material [47]. During growth, new h-BN layers form in between the bottom most h-BN layer and the copper foil. The crystalline order of the copper surface reduces the energy for Bernal stacking compared to AA′ stacking.

The electronic band structure of Bernal (AB) stacked h-BN is very close to that of bulk AA′ stacked h-BN. Both are indirect gap semiconductors and the band gap value of the two is within 20 meV. One key difference is that AB h-BN allows for an optical transition at the K point with an energy only 1% larger than the band gap. Due to the broken

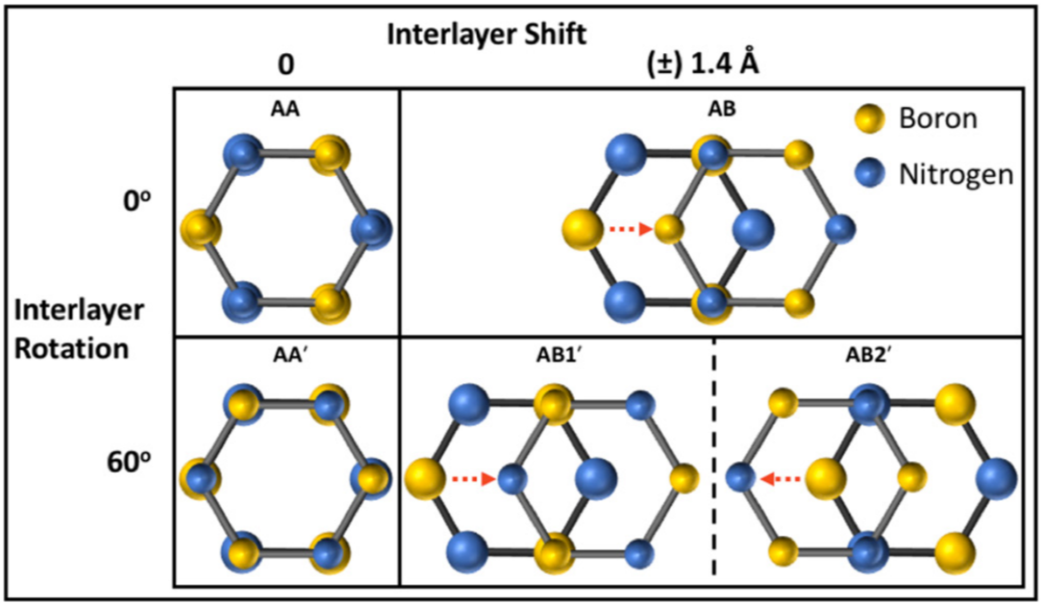

Figure 3.1: Schematics of the 5 high-symmetry stackings in h-BN. In the top half of the figure, the rotationally aligned stacking configurations, AA and AB, are shown. AA stacking has B to B and N to N in two aligned layers. AB is formed by translating one layer by a single bond length (1.4 Å) to stack N to B as shown by the red arrow. The rotationally anti-aligned stacking configurations, AA′, AB1′, and AB2′, are shown in the bottom of the figure. AA′ has two anti-aligned layers with stacking of B to N and N to B. AB1′ is formed by translating one layer such that the layers stack B to B while AB2′ has N to N stacking. Figure courtesy of Matt Gilbert: "Alternative Stacking Sequences in Hexagonal Boron Nitride", *2D Materials* (2019) [47]

inversion symmetry in AB stacked h-BN, this material shows an increased intensity for second harmonic generation [48].

The stacking order of h-BN can be identified with TEM using either aberration-corrected, atomic-resolution imaging or by analysis of the electron diffraction (SAED) pattern. Figure 3.2 shows representative data for each method.

Using atomic-resolution TEM to identify the stacking sequence is fairly straightforward with a few caveats. Similar to the images presented in back in section 2.17, the different stacking sequences can be clearly resolved with imaging. However, the presence of a stacking fault in thick AA′ material would cause the TEM image to appear as AB stacking. Also, because TEM only "sees" the total projection of all the atoms, imaging would not be able to tell if a region had both stacking sequences on top of one another. Luckily, the LP-CVD h-BN samples studied here were very thin with no stacking faults and did not exhibit any regions of AA′ stacking, making interpretation of the images straight-forward.

Figure 3.3 shows an SAED pattern for AA′ and AB h-BN. The stacking type is determined from the diffraction data by comparing the intensities of the first-order $\langle 0\,1\,0\rangle$ and second-order $\langle 1\,1\,0\rangle$ diffraction peaks. An approximate analytical calculation of equation 1.20, neglecting the atomic scattering factor by assuming $f_B = f_N = 1$, using the unit cells of both h-BN types reveals that the intensity ratio, $I_{110}/I_{100} = R$, is:

$$\begin{aligned} R_{AA'} &= 4 \\ R_{AB} &= 16 \end{aligned} \tag{3.1}$$

Equations 3.1 reveal that R for AB is 4 times larger than for AA′. The result of this naïve calculation are qualitatively visible in figure 3.2, where the intensity ratio is much larger in AB than in AA′ h-BN.

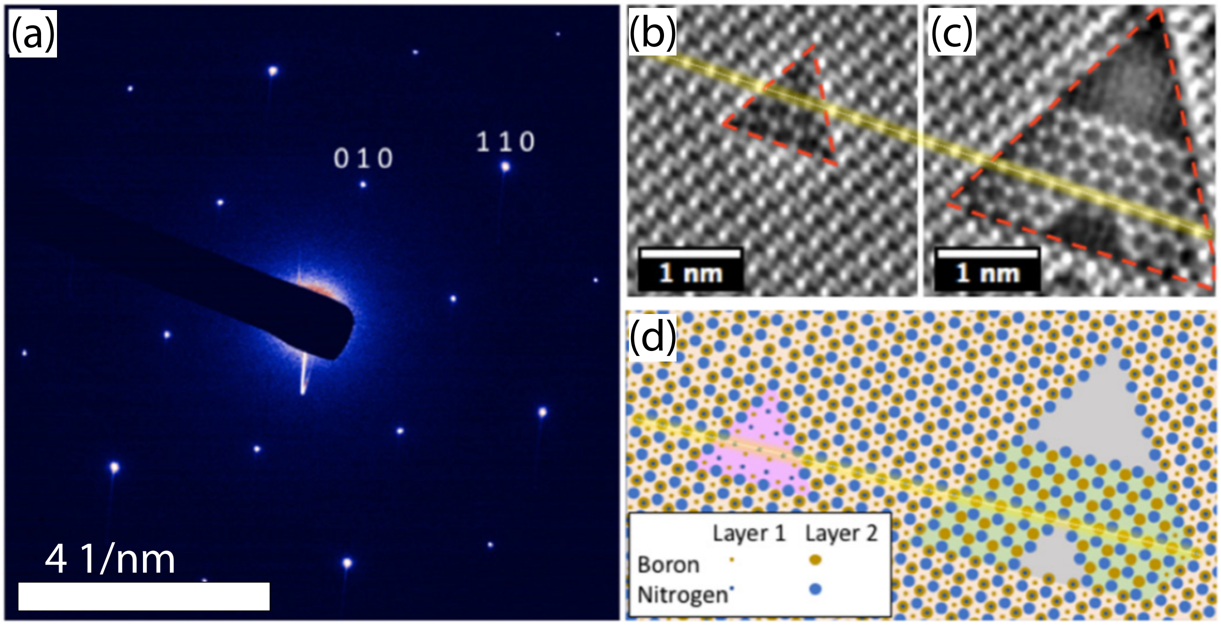

Figure 3.2: TEM characterization of AB h-BN. (a) Representative electron diffraction pattern for multilayer LP-CVD h-BN. The intensity ratio of the first order $\langle 0\,1\,0\rangle$ and second order $\langle 0\,1\,0\rangle$ peaks indicates the stacking order of the h-BN. (b) and (c) Aberration corrected HR-TEM focal series reconstruction of two bilayer/monolayer regions of h-BN. The red-dashed triangles denote the boundary between monolayer/vacuum(inner) and bilayer(outer) areas. (d) Schematic of the position of each atom in (b) and (c). The yellow lines in (b–c) trace a line of stacked atoms in the bilayer region to highlight the alignment of the left and right monolayer regions. Figure courtesy of Matt Gilbert: “Alternative Stacking Sequences in Hexagonal Boron Nitride”, *2D Materials* (2019) [47]

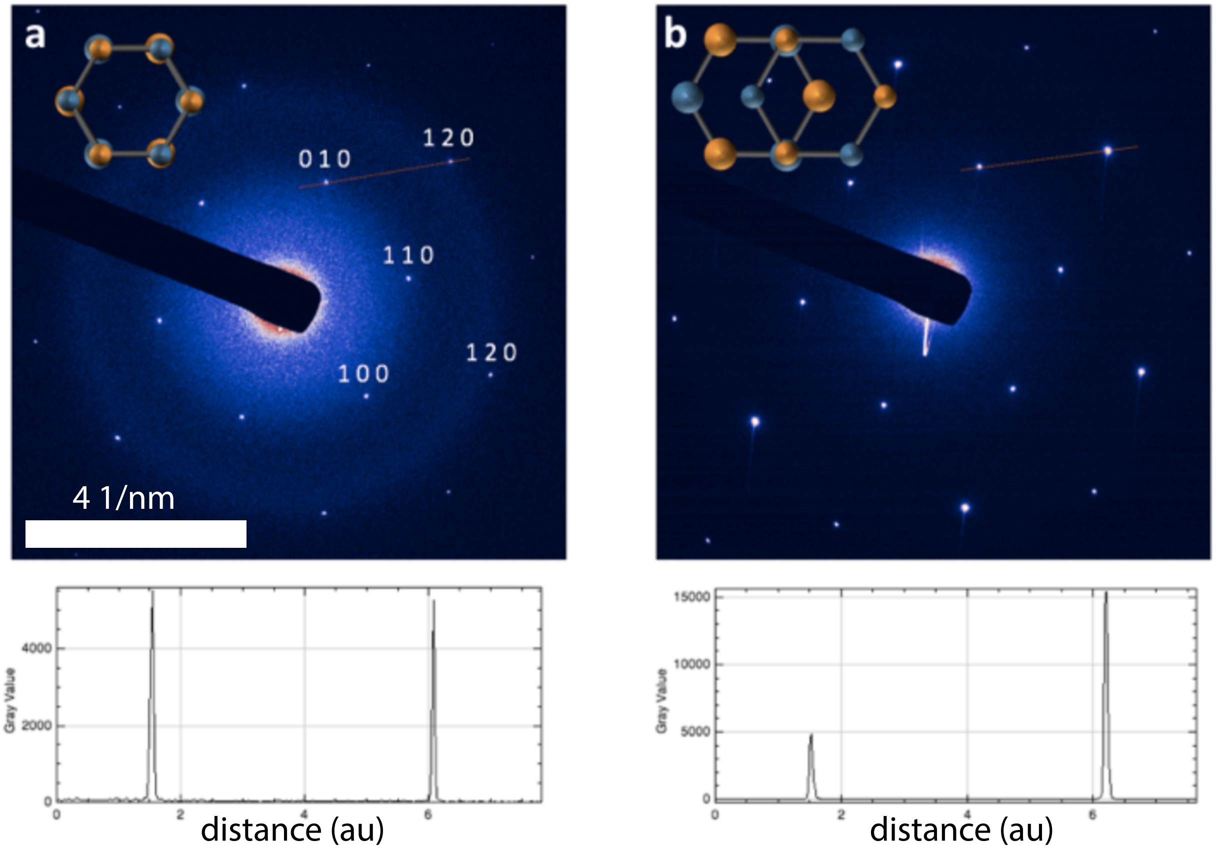

Figure 3.3: Electron diffraction characterization of AA′ and AB h-BN. (Top) Representative SAED pattern for exfoliated bulk AA′ stacked (a) and LP-CVD AB stacked h-BN (b). (Bottom) The ratio of the intensities of the first-order ⟨0 1 0⟩ and second order ⟨1 2 0⟩ peaks determine the stacking order of the h-BN. The ratio ~ 1.1 on the right indicates AA′ stacking and the ratio ~ 0.3 on the right indicates either AB, AB1′, or AB2′ stacking, as detailed in figure 3.1. The discrepancy between the Miller indices here compared to figure 3.2 is due to a different lattice vector convention. Figure courtesy of Matt Gilbert.

A more detailed simulation,using the Single Crystal software package for three types of h-BN (AA′, AB, and ABC) is shown in figure 3.4. This simulation accounts for the atomic scattering factors as well as random thermal motion of the atoms, two factors that cause intensity damping of peaks at with reciprocal space coordinates. The simulations in figure 3.4 and the experimental data in figure 3.3 closely match for the two assigned stacking polytypes (AA′ and AB). Rhombohedral h-BN was not observed experimentally.

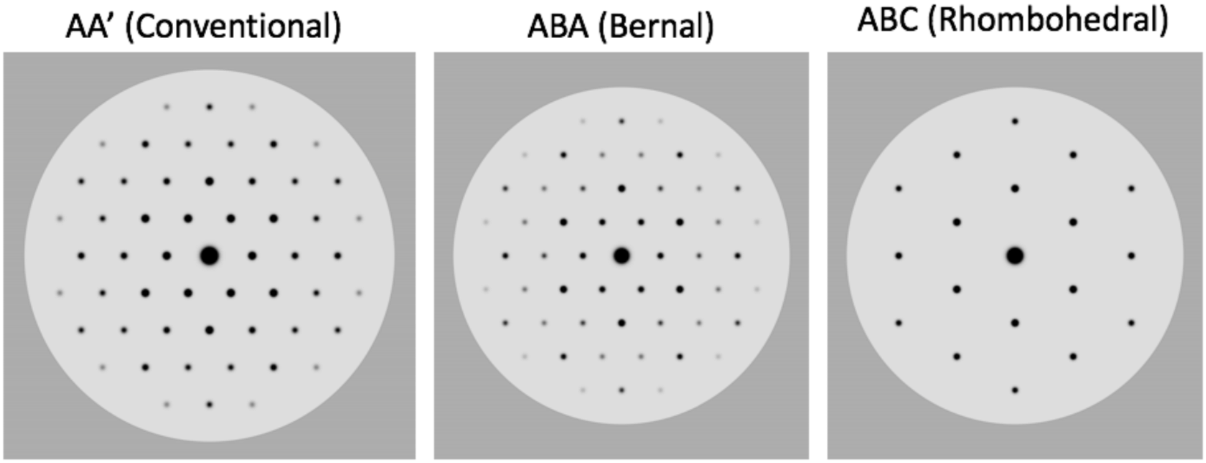

Figure 3.4: Simulated Electron Diffraction for h-BN using the Single Crystal software package. (Left) Simulation for bulk AA′ stacked h-BN (Center) simulation for bulk AB stacked h-BN. (Right) Simulation for bulk ABC stacked rhombohedral h-BN. For the AA′ stacked h-BN, the first-order $\langle 0\,1\,0\rangle$ and second order $\langle 1\,1\,0\rangle$ peaks are approximately equal. For the Bernal stacked h-BN the first order peak is less intense than the second order peak. For the rhombohedral h-BN there is no first order peak.

3.5 CVD h-BN Applications: Fabrication of h-BN Nanopores

In this work, we describe and establish a procedure for the fabrication of individual nanopores in few-layer h-BN with atomically precise control of pore size from few-atom vacancies to several nanometer side-length through careful control of TEM electron beam conditions. This process can be accomplished in a conventional TEM only by modifying the beam conditions and does not need an advanced aberration-corrected TEM.

It has been previously demonstrated that when h-BN is exposed under 80 kV electron irradiation that regular atomically precise triangle defects form [49, 50, 51, 52, 53]. Due to the preferential ejection of boron, attributed either to electron knock-on effects or selective chemical etching by atomic species present in the TEM, metastable nitrogen terminated zig-zag edges form and preserve a triangular shape under the electron beam. As these under-coordinated nitrogen atoms are ejected a new nitrogen zig-zag edge is exposed allowing for the precise quantized growth of triangle defects [53, 54].

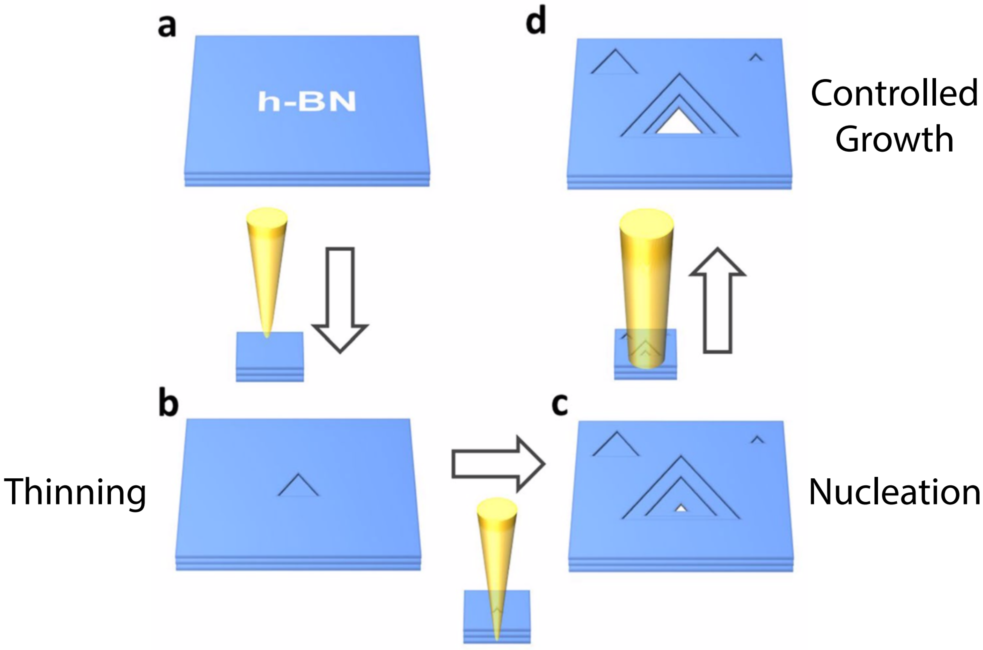

Figure 3.5: Schematic of h-BN nanopore fabrication methodology. (a) Pristine h-BN is irradiated with a TEM electron beam condensed to a 10-20 nm area. (b) Triangular defects form under the beam, stripping away the h-BN layer by layer. (c) After the formation of a single or few-atom vacancy in the final layer, the beam is spread. (d) The final size of the pore can be set by control of the exposed does under the decreased energy density beam. Figure courtesy of Matt Gilbert: "Fabrication of Subnanometer-Precision Nanopores in Hexagonal Boron Nitride", *Scientific Reports* (2017) [46]

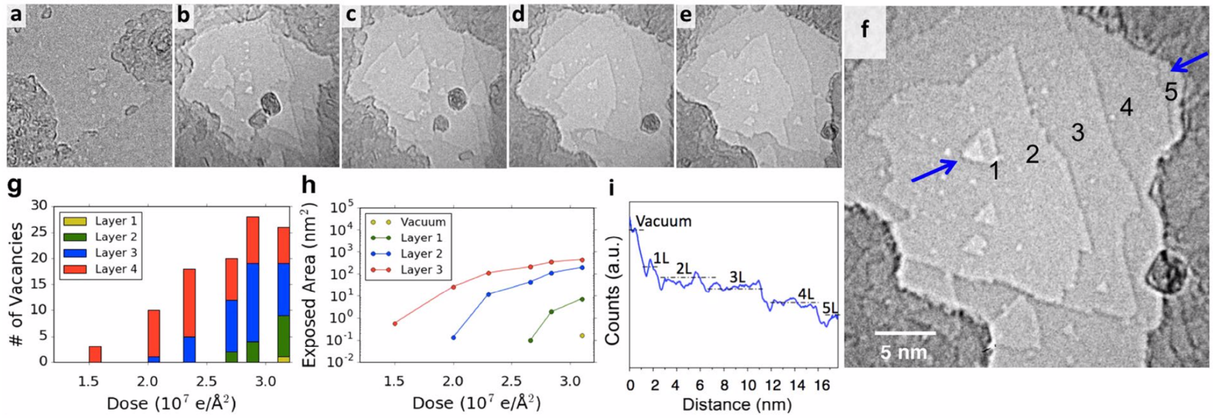

Figure 3.6: Layer by layer stripping of multilayer h-BN. (a–f) time series showing the formation of defects and stripping of layers after exposed doses (in $e^-/\mathring{A}^2$) of (a) 0, (b) 2.0×10^7, (c) 2.3×10^7 (11 min), (d) 2.8×10^7 (15 min), and (e) 3.1×10^7 (18.5 min) under a 10 nm condensed electron beam with a current density of 37 A/cm^2. After frame (e) the beam is expanded and the current density is reduced to 3 A/cm^2 to produce the single nanopore shown in (f). The numbers in (f) denote the number of h-BN monolayers in each region. (g) The number of continuous vacancies present in each layer of the sample as a function of dose. (h) Graph depicting the amount of area exposed of a given layer or below, note that the area exposed of each layer or below goes asymptotically towards probe size. (i) Grayscale count profile along the path between the two arrows in (f). The size in nanometers of frames (a–f) are constant. Figure courtesy of Matt Gilbert: "Fabrication of Subnanometer-Precision Nanopores in Hexagonal Boron Nitride", *Scientific Reports* (2017) [46]

The defects studied in previous work, despite growing at precise increments, were not controlled in number or size; many defects were formed and the rate of growth was left uncontrolled. In studies in which the number and position of the defects in h-BN were controlled, the defects formed were irregular in shape and larger than 5 nm due to the use of high currents or voltages [55, 56].

Our method, outlined in figure 3.5, consists of 3 steps: thinning, pore nucleation, and controlled growth. we first strip away layers in a localized region by milling with a condensed electron beam. As shown in figure 3.6(a–f), exposure to a 10–20 nm diameter condensed beam with a current density of 37 A/cm^2 results in the formation of vacancies in each sequential layer which steadily grow with dose (Fig. 2(g) and (h)), effectively stripping away material layer by layer. Vacancies in the final single-layer region of the h-BN are identified by a larger contrast difference (Fig. 3.6(i)), allowing us to stop the thinning after an isolated vacancy has been introduced in the single-layer region.

After a small vacancy has been produced, a lower energy density beam allows us to grow quantized size triangular nanopores, while new vacancy formation is inhibited. As the nanopore grows, it favors a triangular geometry and is metastable at each quantized triangle size, allowing for easily reproducible, highly regular pore geometry, as shown in figure 3.7(a).

Figure 3.7(b–i) show an example of growth of a single nanopore from a few-atom vacancy to 8 nm^2 with the beam current density reduced to 6 A/cm^2, where the pore growth as a function of dose can be seen in figure 3.7(j).

Electron knock-on effects and/or selective chemical etching due to gases present in the TEM column preferentially eject boron atoms and preserve nitrogen zig-zag edge termination [49, 50, 51, 52, 53]. Hence, each of the created pores is reliably nitrogen terminated, desirable for many nanopore applications where controlling end-group chemistry is critical. When the nanopore has reached its desired size, the beam can be fully expanded or blanked to cease pore growth.

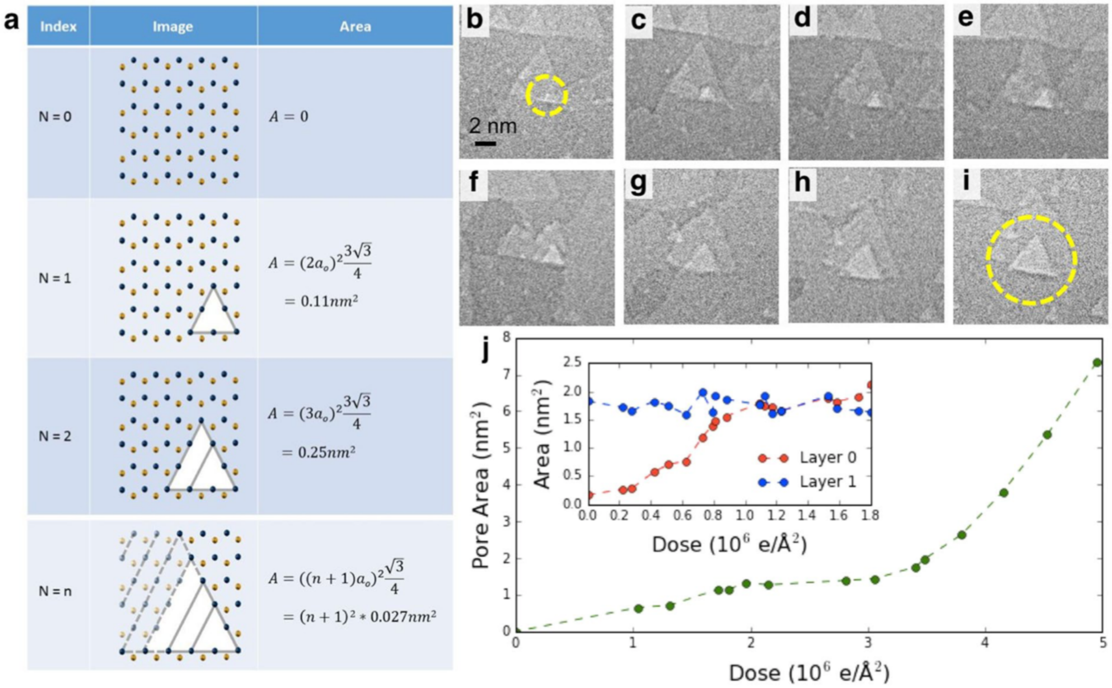

Figure 3.7: Quantized growth of triangular nanopores. (a) For each quantized pore size, the table shows the atomic configuration and pore area. Nitrogen and boron atoms are depicted in blue and gold respectively. The spacing between neighboring boron and nitrogen atoms, a_0, is 1.45 Å. (b–i) Time series showing the quantized growth of a triangular nanopore in h-BN under a beam current of 6 A/cm^2, images taken at 2 minute intervals. (b) Single to few atom vacancy formed in h-BN sheet, circled in yellow. (c–i) Metastable quantized growth of nanopore. (j) Pore area versus dose for the images shown in (a–h). The inset shows a similar growth of pore area versus dose for the nanopore shown in figure 3.6(f) and a neighboring vacancy of similar size in the second layer under a beam current of 3 A/cm^2. Figure courtesy of Matt Gilbert: "Fabrication of Subnanometer-Precision Nanopores in Hexagonal Boron Nitride", *Scientific Reports* (2017) [46]

3.6 h-BN Polytypes: Nanotubes

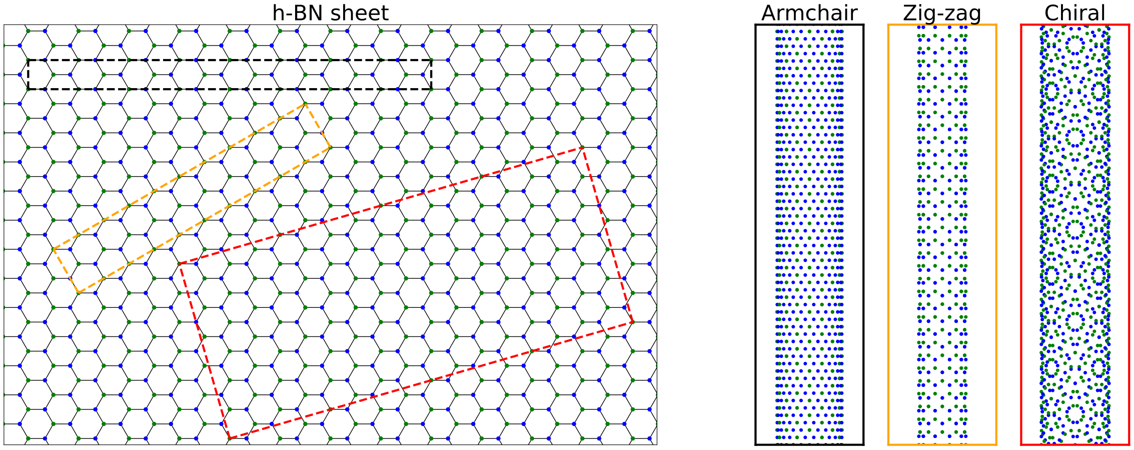

Figure 3.8: Graphic illustrating how nanotubes are related to the 2D h-BN lattice. Depending on the choice of chiral vector, the nanotubes can be armchair, zig-zag, or chiral, as shown in the right panels.

Boron nitride nanotubes (BNNTs) are the one dimensional allotrope of h-BN with similar mechanical, thermal, and electronic properties as the two and three dimensional variants. Unlike carbon nanotubes, whose electronic properties are sensitive to different tube geometries, BNNTs are all semiconducting, regardless of chirality or tube diameter. This fact, along with chemical inertness, makes BNNT's an ideal substrate for finding new structural phases and emergent physics via isolation and confinement of atoms in the one dimensional BNNT core [35].

Nanotube Type	**Indices**	**Tube Diameter**	**Chiral Angle**	**1D Unit Cell Length**
Armchair	(m,m)	$\frac{\sqrt{3}a}{\pi}m$	30°	a
Zig-Zag	$(m,0)$	$\frac{a}{\pi}m$	0°	$\frac{3\sqrt{3}a}{2}$
Chiral	(m,n)	$\frac{a}{\pi}\sqrt{m^2+n^2+nm}$	$\tan^{-1}\left[\frac{\sqrt{3}m}{m+2n}\right]$	$\mathrm{GCD}\left[2m+n, m+2n\right]$

Table 3.1: Table of boron nitride nanotube types and relevant quantities. a is the h-BN lattice constant (2.49 Å) and GCD denotes the greatest common divisor.

From a mathematical perspective, a nanotube is a finite cut from a 2D lattice, wrapped such that the new structure has periodic boundary conditions. A cut is taken from the 2D sheet and a chiral vector, $\mathbf{C} = m\mathbf{a}_1 + n\mathbf{a}_2$, is chosen such that an atom at position $\mathbf{R}$ is wrapped into the lattice point of an atom at position $\mathbf{R} + \mathbf{C}$. Table 3.1 outlines relevant nanotube quantities for the three different types of chiral vector (armchair, zig-zag, and chiral).

Filled h-BN Nanotubes

Material presented in this section is derived from research conducted in collaboration with Aidin Fathalizadeh and Thang Pham. This section contains graphics from the publication: "A Universal Wet-Chemistry Route to Metal-Filling of Boron Nitride Nanotubes", in *Nano Letters* [57]. This section also contains graphics from "Torsional Instability in the Single-Chain Limit of a Transition Metal Trichalcogenide", in *Science* by Thang Pham *et al.* [35].

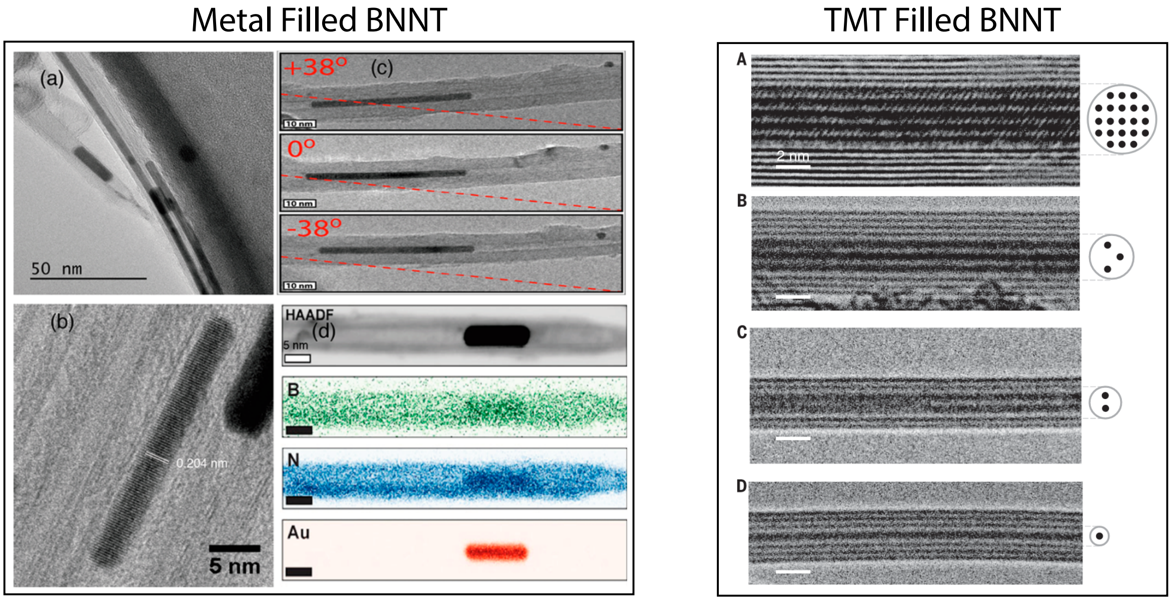

Figure 3.9: TEM characterization of 1D confined materials inside of BNNTs. The left shows TEM characterization of gold filled BNNTs. The gold tends to form long, highly crystalline nanorods (a-b). A series of TEM images, tilted about the red dashed line, confirms that the rods are indeed encapsulated within the tube (c). HAADF STEM image and complementary EDS chemical maps verify the composition of the nanorods (d). The right shows TEM images of BNNTs filled with the chain material $NbSe_3$. The material can be confined to several, triple, double, and single unit cell widths, as shown in A,B,C, and D, respectively. Figures taken from references [58](left) and [35] (right).

As discussed earlier, BNNTs are an ideal substrate for confinement of material in one dimension. The chemical inertness and large band gap of the BNNT allows for investigation of the effects of dimensional confinement and minimizes the effects of coupling to the confining medium. Figure 3.9 shows two examples of 1D confined materials inside of BNNTs, elemental metals (left) and transition-metal trichalcogenide (TMT) chain materials.

3.7 h-BN Polytypes: sp^2 Aerogels

The material presented in this section is derived from research conducted in collaboration with Sally Turner, adapted from two publications: “Self-Assembly and Metal-Directed Assembly of Organic Semiconductor Aerogels and Conductive Carbon Nanofiber Aerogels with Controllable Nanoscale Morphologies”, in *Carbon* [59] and “Density Tunable Graphene Aerogels Using a Sacrificial Polycyclic Aromatic Hydrocarbon”, in *Physica Status Solidi (b)* [60], as well as unpublished researched presented in Sally Turner’s P.h.D. thesis.

A gel is a material that is mostly liquid by weight, but behaves more like a solid, due to a three-dimensional cross-linked network within the liquid. An aerogel is a gel with the liquid in the material replaced with gas. The hallmark properties of an aerogel are high surface area, low density and hierarchical porosity. Hierarchical porosity, as the name implies, is the presence of micropores (pore size $\lesssim$ 2 nm), mesopores (2 nm $\lesssim$ 50 nm), and macropores ($\gtrsim$ 50 nm). Micro and mesopores are responsible for an aerogel’s high surface area and macropores provide accessibility to that large active surface area.

Aerogels are useful for any application that requires high surface area and low-density and have many uses in aerospace, catalysis, sensing, and energy storage. Furthermore, nanomaterial based aerogels can result in low-density bulk materials that retain the extraordinary properties of the nanomaterial building blocks.

This section presents TEM characterization methods applied to h-BN-based aerogels. These techniques were essential for understanding the relationship between synthetic parameters and the resulting morphology, crystallinity, and stoichiometry of the final synthesized aerogel.

3.8 Characterizing BCN sp^2 Aerogels with EELS

$B_xC_yN_z$ (BCN) materials have exciting potential applications due to their tunable electronic properties [61] between graphite (no band gap) and h-BN (wide band gap) and altered chemical properties. Coupling the electronic tunability of BCN with the textural properties of the aerogel morphology provides additional functionality to the material. BCN materials have been used for catalysis and yield impressive results approaching the industry standard platinum electrode [62, 63]. Perhaps the ultimate goal of BCN materials and heterostructures is their integration into electronics, enabling bottom-up synthesis of atomic scale circuitry [64, 65].

TEM EELS is an ideal method for quantifying the chemistry of BCN materials. EELS core-loss scattering has a high cross-section for lighter elements, and the B, C, and N core-loss peaks are at convenient, well-spaced energies. Figure 3.10 shows a representative EEL spectrum taken from a $\sim$ 100 nm region of BCN material. The spectrum displays distinctive B, C, and N K-edges, all with sp^2 fine structure. The fine structure of these peaks (in particular the sharp π^* and σ^* sub peaks) clearly indicates that the material contains a sp^2 bonded network of all three elements. The relative intensity of these peaks can be used to determine the chemical composition of the material.

The relative abundance, $N_{A(B)}$, of elements $A(B)$ in a specimen is related to the integrated EELS intensity of core-loss scattering, $I_{A(B)}$,by the relation [66]:

$$\frac{N_A}{N_B} \approx \frac{I_A\left(\beta,\Delta\right)\ \sigma_B\left(\beta,\Delta\right)}{I_B\left(\beta,\Delta\right)\ \sigma_A\left(\beta,\Delta\right)} \tag{3.2}$$

where, $\sigma_{A(B)}$ is the scattering cross section for element $A(B)$, β is the scattering collection angle and Δ is the width of the energy window. The collection angle, β, is a fixed param-

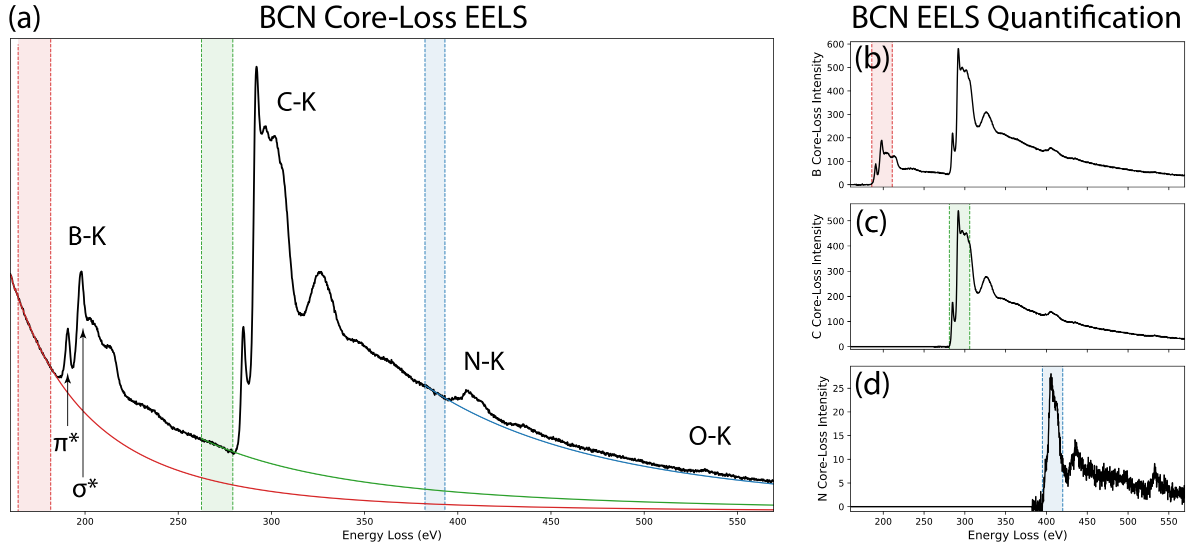

Figure 3.10: Quantification of chemical composition from EELS spectra. Panel (a) shows a typical core-loss EELS spectrum from a BCN material which displays strong peaks from the B, C, and N K edges. The fine structure of the edges (π^* and σ^* peaks) is indicative of sp^2 bonding in the material. The small O-K peak in the spectrum results from residual oxygen in the sample. The red, green, and blue regions indicate the regions of the spectrum that were used for determine the background of each edge. Panels (b-d) show the background-subtracted spectrum for each element.The colored window in each spectrum shows the 25 eV energy window used for integration of intensity. The integrated intensity is used in equation 3.2 to determine the relative abundance of each element.

eter in these experiments ($\sim$ 20 mrad) and is determined by the entrance aperture of the spectrometer.

Figure 3.10 (b-d) illustrates the quantification procedure. A power law background intensity is fit and subtracted from each spectrum, leaving only the scattering intensity from core-loss transitions, used to quantify the relative abundance of B, C, and N in the sample using equation 3.2.

The major challenge of BCN materials synthesis is preventing phase segregation. The two materials have high thermodynamic stability and at high temperature, a BCN solid solution will easily phase segregate into domains of C and BN [67]. In the case of nanotubes, radial phase-separation of discrete carbon and boron nitride shells has been observed when attempting to synthesize BCN nanotubes [68]. Because the system has a tenancy to phase segregate, it is important to use spatially resolved chemical characterization techniques to study BCN materials to confirm that the material is truly a ternary BCN alloy.

The single spectrum presented in figure 3.10 indicates a sp^2 BCN network and quantification of the spectrum reveals the average stoichiometry, but it does not specify if the material is a BCN solid solution or phase segregated C and BN. To answer this question, spatially resolved EELS hyperspectral maps are taken using a range of raster step sizes. The resulting spectra from each pixel location of the SI are quantified using equation 3.2, revealing the local chemistry and degree of phase segregation at the nanometer scale.

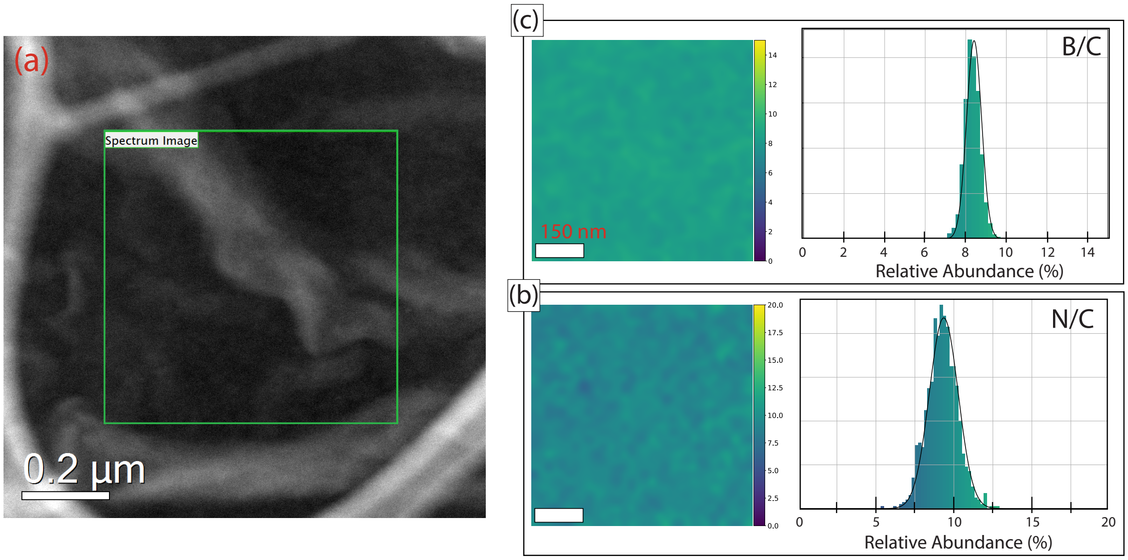

Figure 3.11: Spatially resolved chemical quantification of BCN sp^2 aerogels. The green square in the HAADF STEM image in (a) shows the region that the EELS SI was taken from. The EEL spectrum, similar to the one in figure 3.10, at each pixel of the SI is quantified, resulting in the spatially resolved chemical maps in (b) and (c). The relative abundance of B and N (normalized to the abundance of C) is approximately constant across the spatial region with a normal distribution of abundance values. No evidence of phase segregation is observed.

Figure 3.11 shows a representative STEM EELS dataset from a BCN aerogel. The results of chemical quantification for each spatial pixel are shown in figures 3.11(b) and 3.11(c). The relative abundance of B and N (relative to C) is fairly homogeneous with no obvious phase segregation at length scales above ∼ 10 nm. Histograms showing the measurement statistics are normally distributed about their mean value, further confirming that the material is a true BCN composite. The values obtained for each sample was in rough agreement with bulk chemical quantification using x-ray photoelectron spectroscopy (XPS), indicating that the bulk measurements were representative of the nanostructure of the material.

In order to quantify the length scales at which the sample is homogeneous, several SIs were acquired using different step sizes between pixels. Figure 3.12 shows the results of these measurements. The BCN aerogels showed no signs of phase segregation for spatial resolution down to 5 nm.

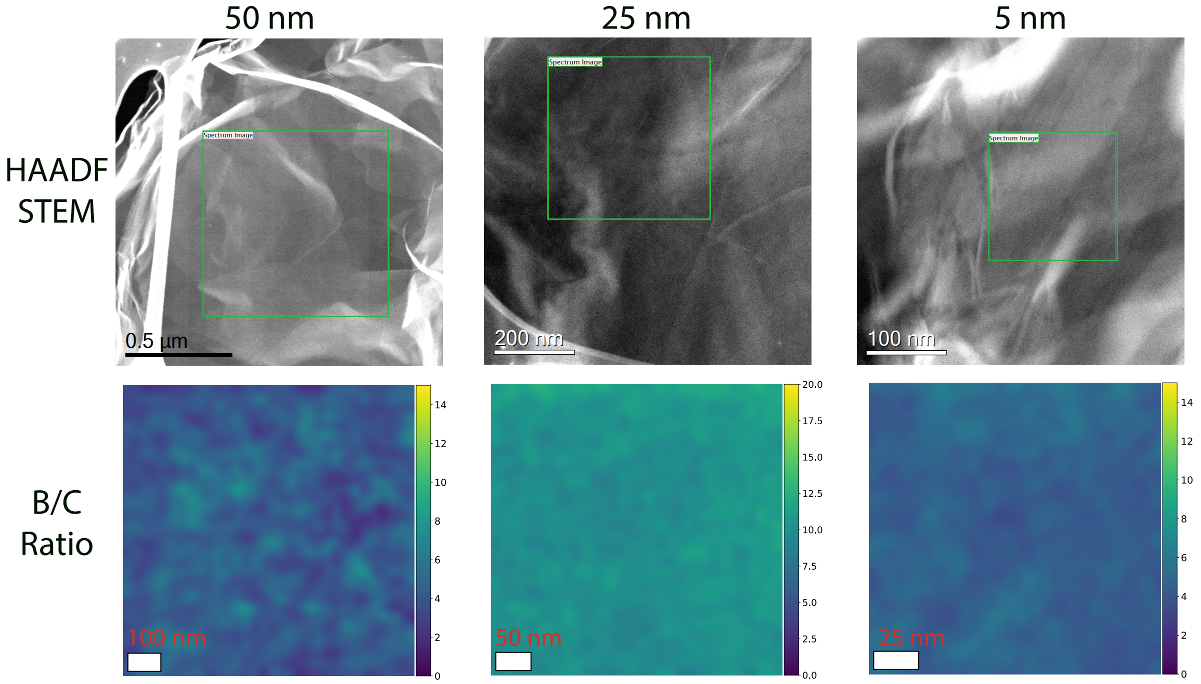

Figure 3.12: Spatially resolved chemical quantification of BCN sp^2 aerogels at three magnifications. The top row of images shows HAADF STEM images for three representative BCN aerogel samples. The green box in each top image indicates the region that an EELS SI was taken from. The corresponding images in the bottom row show the results of EELS quantification for each SI. The numbers above each column indicate the spatial resolution of each measurement. In each case, the B/C ratio is normally distributed about a mean value between 8-20 %. The images appear essentially homogeneous, indicating a lack of C/BN phase segregation.

Chapter 4

Single Photon Emitters

> *"A man provided with paper, pencil, and rubber, and subject to strict discipline, is in effect a universal machine."*
>
> — Alan Turing

4.1 Introduction

The emerging field of quantum information science (QIS) encompasses any information technology that uses quantum bits, or qubits, to process or transmit information. Quantum information processing can perform tasks that would be impractical (factoring large prime numbers using Shor's algorithm [69]) or impossible (accurate simulation of quantum many-body system time-evolution [70]) using a classical computer. Information transfer using qubits ensures that the security and privacy of the encoded information is guaranteed by fundamental physics [71]; classical cryptographic protocols rely on the assumption that brute force decryption is too time consuming to be practical [72]. When quantum computers become available, widely used public-key cryptographic schemes (most of which rely on the computational complexity of factoring large prime numbers) will become obsolete.

A qubit is any quantum system that can exist in a superposition of two distinguishable, orthogonal states. Potential qubits include the following:

- Electronic state of trapped, cold atoms or ions [73]
- Spin state of electrons or atomic nuclei [74]
- Charge, flux, or phase state of superconducting Josephson junctions [75]
- Polarization state of single photons [76]

Due to the absence of charge and mass, photons are weakly coupled to their environment and have small interaction cross sections, making photons in the optical region of the spectrum the best, and possibly only, candidate for long range transmission of quantum states. The majority of potential qubits only exhibit their desirable quantum properties at very low temperatures. Photon qubits have the great advantage of being able to operate at room-temperature.

4.2 What is a Single Photon Emitter?

As the name implies, a single photon emitter (SPE) is a system that emits single photons. The degree to which a photon source is an SPE is encoded in the time statistics of light emission from the system. Figure 4.1 illustrates the three types of time statistics a photon source can exhibit, bunching (classical light), random (coherent light), and anti-bunching (quantum light). Table 4.1 outlines the terminology associated with each type along with example systems.

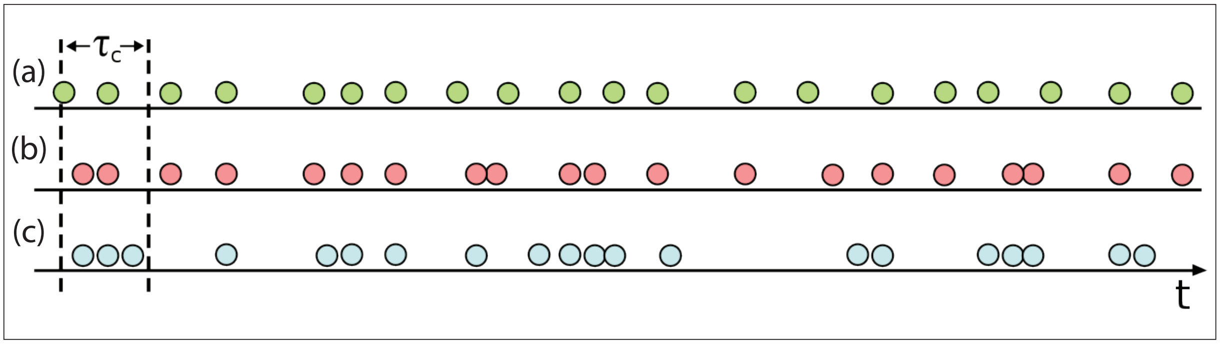

Figure 4.1: Photon detection events as a function of time for anti-bunched (a), random (b) and bunched light (c). Here, τ_c is the coherence time, the timescale for fluctuations of the light. Anti-bunched light from a single photon source contains a single photon per unit coherence time, whereas bunched light has a high probability of containing multiple photons in one coherence time interval. Photons from a coherent light source are randomly emitted as a function of time. © User:Ajbura / Wikimedia Commons / CC-BY-SA-4.0

Photon Statistics	**Other Terminology**	**Examples**
Anti-bunching	Single photon source Quantum emitter	Color centers Quantum dots Single atoms
Random	Coherent source	Laser
Bunching	Thermal source Chaotic light Classical light	Incandescent light bulb Arc-discharge lamp Blackbody radiation

Table 4.1: Table of terminology related to photon time statistics. Many of the terms used to describe each type of statistics are used interchangeably in the literature although they have slightly different meanings.

Photon anti-bunching is a result of the fact that a quantum emitter can only emit a single photon at a time. The process can be modeled as a two-level system, where the excited state requires a finite amount of time before relaxing to the ground state by emitting a photon. The temporal separation between emitted photons is therefore determined by the lifetime of the excited state.

4.3 Quantifying the Time Statistics of Light

The time statistics of a photon source are quantified by the second-order correlation function of the emitted light. The normalized second-order correlation function is given by:

$$g^{(2)}(\tau) = \frac{\langle I(t)I(t+\tau)\rangle}{\langle I(t)\rangle^2} \tag{4.1}$$

where $I(t)$ is the instantaneous intensity of the light and the angle brackets denote a time average. This function is mathematically equivalent to the autocorrelation function of a time dependent signal.

The $g^{(2)}(\tau)$ for each statistical distribution of light (bunched, anti-bunched, and random) has a distinct shape, illustrated in figure 4.2. SPEs have a $g^{(2)}(\tau)$ curve with a dip at short delays, coherent light has a flat $g^{(2)}(\tau)$ curve, and classical light has a peak in $g^{(2)}(\tau)$ at short delay times.

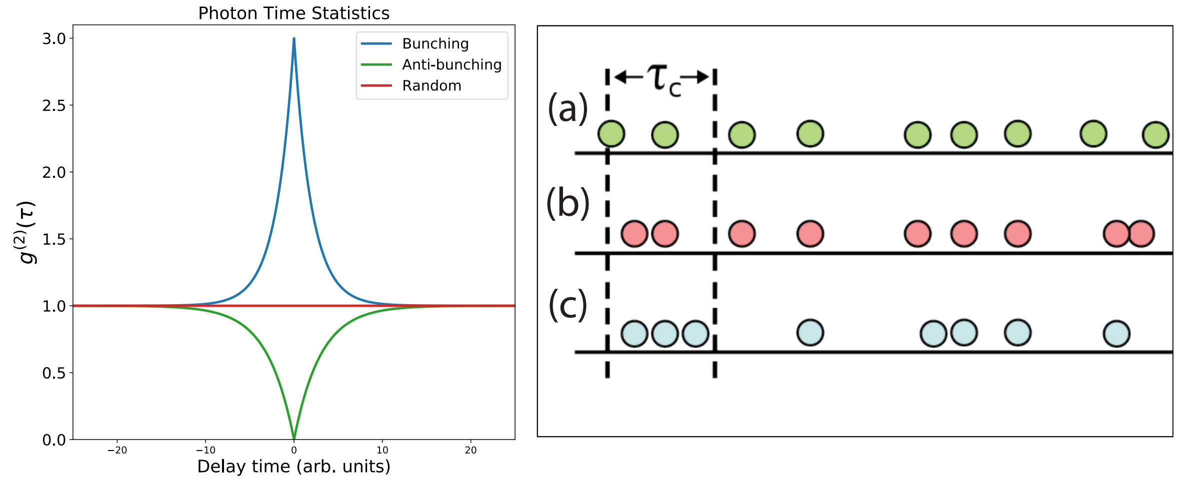

Figure 4.2: Second-order correlation for bunched, random, and anti-bunched light (left). The width of the bunching peak and anti-bunching dip are indicative of the excited state lifetime of the light emitter. The cartoon on the right shows the time dependence of photon emission for each $g^{(2)}(\tau)$ curve shown on the left (with matching colors).

The $g^{(2)}(\tau)$ measurement is the primary method used in the nano and quantum optics communities to determine if a light emitter is a single photon source. Generally speaking,

$g^{(2)}(\tau)$ is measured using PL excitation and if the curve shows an anti-bunching dip, the emitter under study is considered an SPE.

The situation is somewhat different when characterizing light emitters using cathodoluminescence (CL). In this case, $g^{(2)}(\tau)$ can exhibit large bunching peaks, even for confirmed single photon sources. An excellent, in-depth, discussion of photon bunching in CL is presented by Meuret *et al.* [77], and is also discussed in chapter 5. Essentially, probing a sample using an electron beam results in the simultaneous creation of tens to hundreds of electron-hole pairs. The $e - h$ pairs can then radiatively recombine in any nearby color centers or defect levels. This means that all SPEs in the local environment will simultaneously emit a single photon, giving a sharp peak in the zero delay light correlation.

4.4 Hanbury-Brown-Twiss Interferometry

Figure 4.3 outlines the experimental setup used to measure the time correlations of light emission. In principle, a single, perfect photon counter could be used to record the arrival time of each photon in an incoming stream of light, and the time correlations between photons could be calculated directly, as shown in figure 4.3(a). In practice, photons counters are not perfect and usually have dead times that are larger ($\sim$ 100 ns) than the relevant time scales of excited state lifetimes of photon emitters ($\sim$ 10 ns).

To overcome the limitations of detector dead time, two photon counters and a 50/50 beam splitter are used in the Hanbury-Brown and Twiss configuration shown in figure 4.3(b). This detection scheme is used to record the histogram of time intervals, $K(\tau)$, between consecutive photon detection events. The histogram is equivalent to $g^{(2)}(\tau)$ after normalization to a

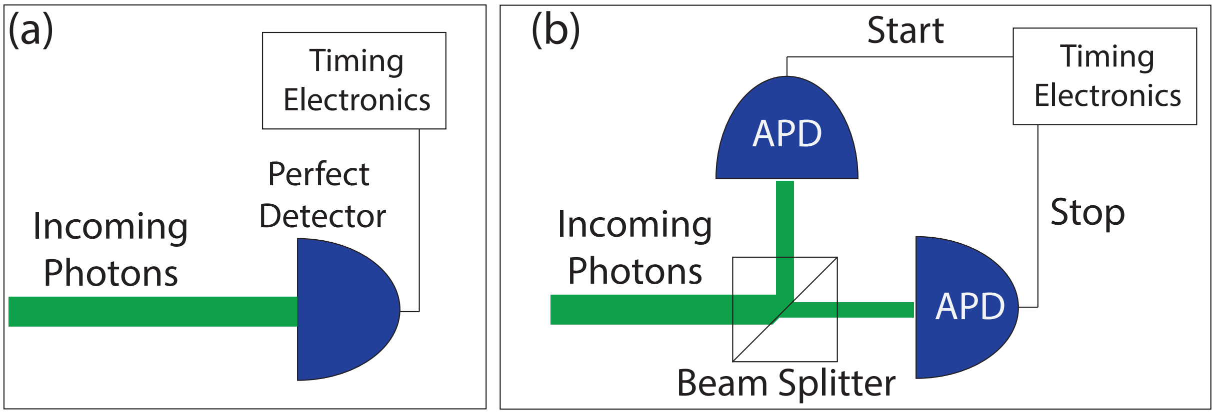

Figure 4.3: Apparatus for measuring second-order photon correlation function. In principle, a detector with no dead time could be used to measure the arrival times of all incoming photons, and the time correlation could be calculated, illustrated in (a). In reality, detectors have a finite dead time, so a start-stop setup (b) is used to measure correlations for times much less than the detector dead time.

Poissonian light source using the average histogram counts at long delay times, K_∞ [78, 79].

$$g^{(2)}(\tau) = \frac{K(\tau)}{K_\infty} \tag{4.2}$$

The start-stop configuration and Equation 4.2 are appropriate provided two conditions. First, the relevant time scale of correlations in the photon emission must be less than the detector dead time ($\tau \ll \tau_{dead}$). Second, the average time between photon arrivals (or the inverse of the average photon count rate, R^{-1}), must be greater than the correlation time scale ($\tau \ll R^{-1}$).

Chapter 5

Blue-Light-Emitting Color Centers in High-Quality h-BN

"I don't believe in astrology; I'm a Sagittarius and we're skeptical."

— Arthure C. Clarke

5.1 Chapter Abstract

This chapter is adapted from a paper published in *Physical Review B*, titled "Blue-Light-Emitting Color Centers in High-Quality Hexagonal Boron Nitride" [37], based on work done as part of my Ph.D. research at the Molecular Foundry.

Light emitters in wide band gap semiconductors are of great fundamental interest and have potential as optically addressable qubits. Here we describe the discovery of a new color center in high-quality hexagonal boron nitride (h-BN) with a sharp emission line at 435 nm. The emitters are activated and deactivated by electron beam irradiation and have spectral and temporal characteristics consistent with atomic color centers weakly coupled to lattice vibrations. The emitters are conspicuously absent from commercially available h-BN and are only present in ultra-high-quality h-BN grown using a high-pressure, high-temperature Ba-B-N flux/solvent, suggesting that these emitters originate from impurities or related defects specific to this unique synthetic route. Our results imply that the light emission is activated and deactivated by electron beam manipulation of the charge state of an impurity-defect complex.

5.2 Introduction

Luminescent defects in wide band gap semiconductors are of great importance for both fundamental physics and future technological applications. Many of these defects are single photon emitters (SPEs), a likely component of next-generation information technologies, especially quantum cryptography[80, 81] and information processing[82, 83, 76]. SPEs embedded in solid state systems are particularly significant for widespread adoption of these emerging technologies as they offer a promising route toward scalable deployment of new integrated quantum circuits. The diamond nitrogen-vacancy (NV) center has been the leading candidate for solid-state SPE applications because it can easily be manipulated and readout at room temperature using existing optical methods[84, 85]. Due to the technical difficulty of synthesizing and fabricating diamond-based devices, greater attention has been placed on finding new solid-state SPE systems[86, 87] with particular emphasis placed on 2D material systems, especially sp^2-bonded hexagonal boron nitride (h-BN))[43, 42, 88, 89, 90].

h-BN or "white graphite" has been of great interest to the nanoscience community over the last several decades, in part because it is isostructural to graphite and forms many of the same types of nanostructures as sp^2-bonded carbon, but with different electronic and thermodynamic properties[91, 92, 39, 40, 93]. h-BN is especially important to the expanding study of 2D materials because it is atomically flat, inert, and electrically insulating, making it an ideal substrate for testing new physics in low-dimensional materials[41]. Recently it has been shown that the local structure of h-BN can be controlled via electron irradiation[94, 46] and synthetic methods[47], allowing for additional material control.

In this communication we report the discovery of a new color center in high- quality h-BN, activated and characterized by an electron beam. We show that these emitters are highly localized, are spectrally pure, and have an emission signature indicative of weak lattice coupling at room temperature. These properties make the new color center a promising candidate for future applications in quantum information science.

5.3 Experimental

Ultra-high-quality h-BN crystals used in this study (generally accepted as the best substrates available for sensitive device applications and scanning probe measurements) are synthesized using a Ba-B-N solvent precursor at high temperature and high pressure at the National Institute for Materials Science (NIMS) by Watanabe and Taniguchi[45]. We refer to this material throughout the text as NIMS-BN. Millimeter size crystallites are mechanically exfoliated using blue wafer dicing tape and transferred onto p++ silicon substrates (0.001-100 Ω-cm) with a few nm thick native oxide layer. Samples of commercially available h-BN (Alfa Aesar 040608) are similarly exfoliated and transferred, and then annealed at 850 °C in argon at one Torr for one hour before characterization.

We use CL in a scanning electron microscope (SEM) to activate and characterize light emission from the h-BN. CL measurements are performed using a home-built SEM CL system shown in FIG. 5.1 The system is built around a Zeiss Gemini Supra 55 VP-SEM operated at accelerating voltages between 2-10 keV with beam currents in the 100-1500 pA range. Light emission from the sample is collected by a parabolic mirror and directed down an optical path for characterization. Synchronous data from SEM (secondary electron and in-lens detectors) and optical (photon counting point detectors and spectrometer) channels are acquired using the Molecular Foundry ScopeFoundry software[95]. All experiments are conducted at room temperature.

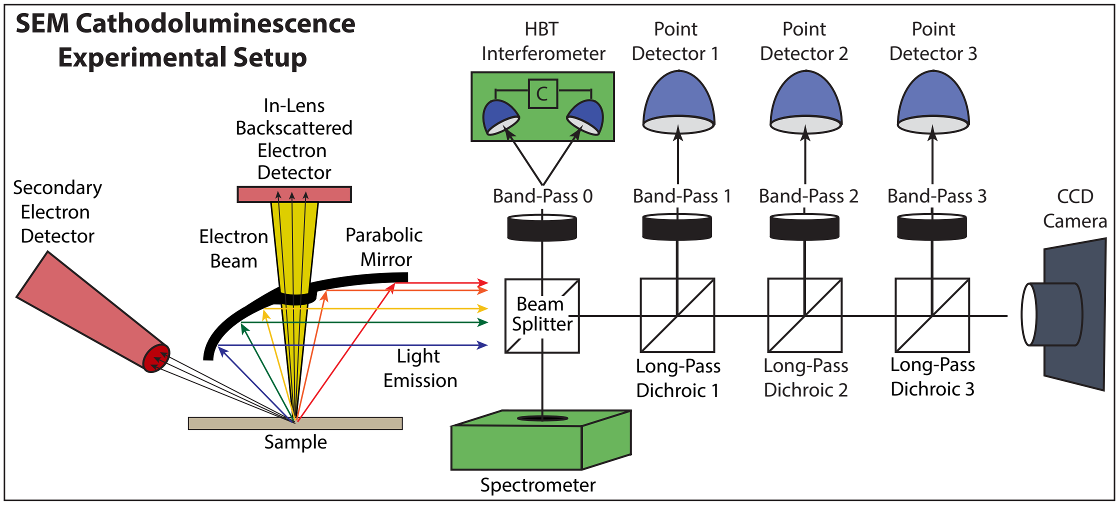

Figure 5.1: Experimental setup for measuring cathodoluminescence (CL) in the scanning electron microscope (SEM). The electron beam excites the sample and causes it to fluoresce. The resulting light is then used for hyperspectral imaging by a spectrometer (slow acquisition, low signal to noise, high spectral resolution) and point detectors (fast acquisition, high signal to noise, low spectral resolution). A Hanbury-Brown Twiss (HBT) interferometer is used to measure the second order coherence function ($g^2(\tau)$) of the light emission.

As the electron beam is rastered across the sample, the light emission from each point of the scan can be coupled into an optical fiber (Thorlabs FG200UEA) using a UV-enhanced parabolic aluminum reflector and recorded using a spectrometer (Princeton Instruments SP2300i) with CCD camera (Andor 970-UVB) to capture the spectral distribution of the light at each pixel, resulting in a three-dimensional data set we refer to as a spectral image (SI). The spectra are not intensity corrected for the wavelength dependent efficiency of the spectrometer grating and CCD camera.

Alternatively, the light can be directed through a series of dichroic mirrors and bandpass filters to an array of photon counting photomultiplier tube point-detectors (Hamamatsu H7360-01, Hamamatsu H7421-40, and Hamamatsu H7421-50), resulting in intensity images of well-defined wavelength bands. We refer to such data throughout the text as bandpass (BP) images.

Time-correlation of the emitted light can be measured by coupling to a Hanbury-Brown-Twiss (HBT) setup. The arrival times of photons at the detectors in both arms of the apparatus are recorded with 50 ps resolution and a coincidence histogram as a function of delay time between the two detectors is made. The raw coincidence histogram is then normalized by the number of coincidences at long delay times. A background correction is performed using the signal to background ratio estimated independently for each measurement[78], resulting in a measurement of the second-order auto-correlation function ($g^2(\tau)$) of the emitted light (See section 5.7 for more details).

All data analysis is performed using common open-source packages in the Python programming language. Multivariate statistical analysis (MVA) of hyperspectral images is carried out using the HyperSpy Python package[96].

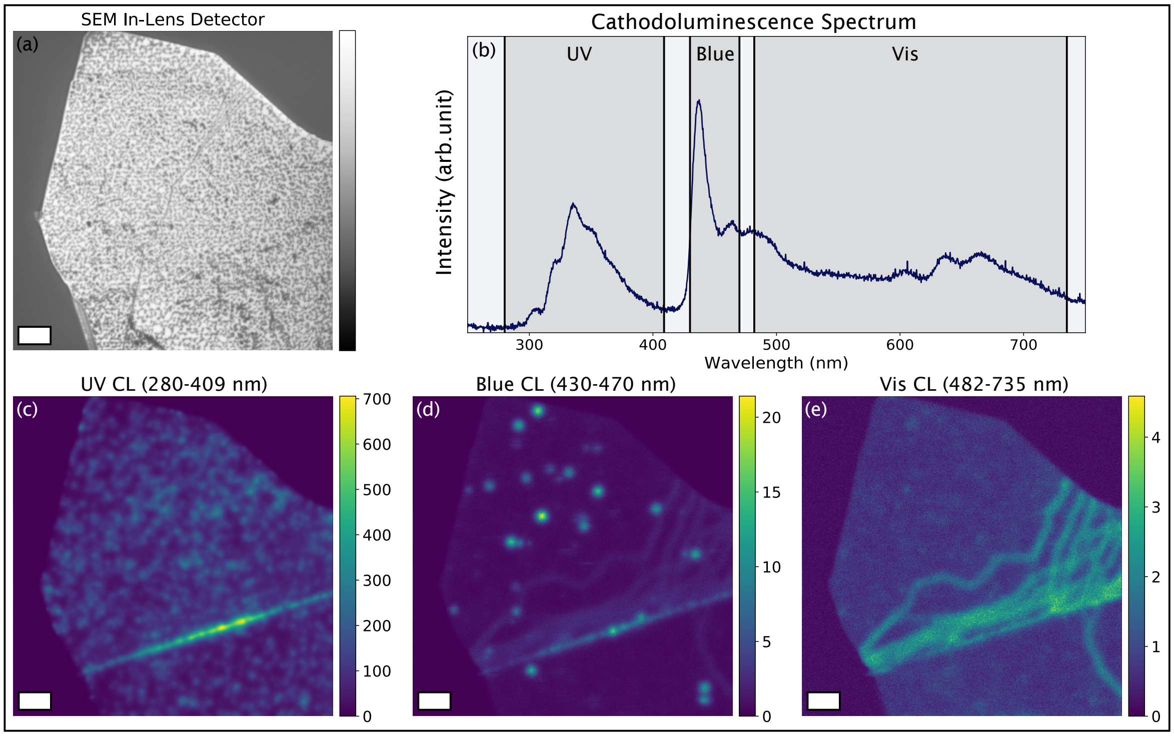

Figure 5.2: Overview of light emission from h-BN. An SEM image of a flake of h-BN is shown in (a), scale bar is 1 μm. Panel (b) shows the mean Cathodoluminescence (CL) response from the sample, with the three main spectral bands of interest indicated by vertical lines and shaded regions. Panels (c-e) show the light emission from the flake in each of these 3 spectral bands (wavelength range listed above each image, intensity scale in counts/pixel). Panel (c) shows UV light emission from a high density of point-like emitters as well as bright emission from a large line-like feature. The intensity in the Blue band arises mostly from the new point-like emitters, shown in Panel (d). Panel (e) shows the spatial distribution of intensity from the green to red region of the spectrum (Vis). Emission in this band arises mostly from extended defects in the crystal. The images are generated by averaging 17 consecutive scans, each with a pixel dwell time of 28.6 μs/pixel.

5.4 Results

We first describe results from NIMS-BN. In order to activate and characterize individual emitters, we initially identify large (lateral size of 10-100 μm) flakes of h-BN using the raster scan images from the SEM electron detectors, shown in FIG. 5.2(a). Optical and atomic force microscopy (AFM) observations of our samples indicate that the flakes generally have thicknesses of tens to hundreds of nanometers. Relevant spectral bands for BP imaging are determined by inspection of the average CL spectrum, shown in FIG. 5.2(b), obtained by integrating spectra while continuously scanning a single flake. We isolate the primary spectral regions of interest (indicated by the vertical lines and shaded regions in FIG. 5.2(b)): 280-409 nm (UV), 430-470 nm (Blue), and 485-735 nm (Vis) for BP imaging with appropriate dichroic and bandpass optics.

There are several striking features in each channel of the BP images. FIG. 5.2(c) shows the spatial distribution of the previously reported UV emitters in the h-BN flake[90]. The emitters have a point-like character and are densely and uniformly distributed across the entire h- BN crystal, with enhanced emission along line-like features that are likely associated with extended line defects[97] or strain caused by a wrinkle or fold in the crystallite[98]. FIG. 5.2(e) shows very weak extended features in the Vis band (485-735 nm) as previously reported[97]. These features are localized at grain-boundaries and dislocations within the h-BN crystal. No localized, point-like sources of light emission are observed within this band using CL BP imaging.

The bright, point-like features in the Blue BP image between 430-470 nm in FIG. 5.2(d) show the new color centers in NIMS-BN, which are the focus of this study. They appear slightly larger and less dense compared to the UV emitters in the previous panel. Also present is the line-like feature from the UV band, as well as a very weak signal from extended features in the Vis band. The broad spectral character of these extended features results in residual intensity "leaking" into the Blue band.

We further characterize electron-stimulated light emission from NIMS-BN using hyperspectral CL imaging by collecting a CL spectrum from each pixel in a raster scan. To isolate the unique spectral signature of each type of emitter we perform a non-negative matrix factorization (NMF) decomposition[25] of the spectra in the SI into four components that visualize the main features present in the dataset. FIG. 3(a-f) show the results of the decomposition. Each image (also called the decomposition loading or decomposition weight) shows the relative abundance of each associated spectral component (also called the decomposition factor) below. The vertical red lines in FIG. 5.3(a), 5.3(c), and 5.3(e) show the pass band used for BP imaging in FIG. 5.2(c), 5.2(d), and 5.2(e), respectively.

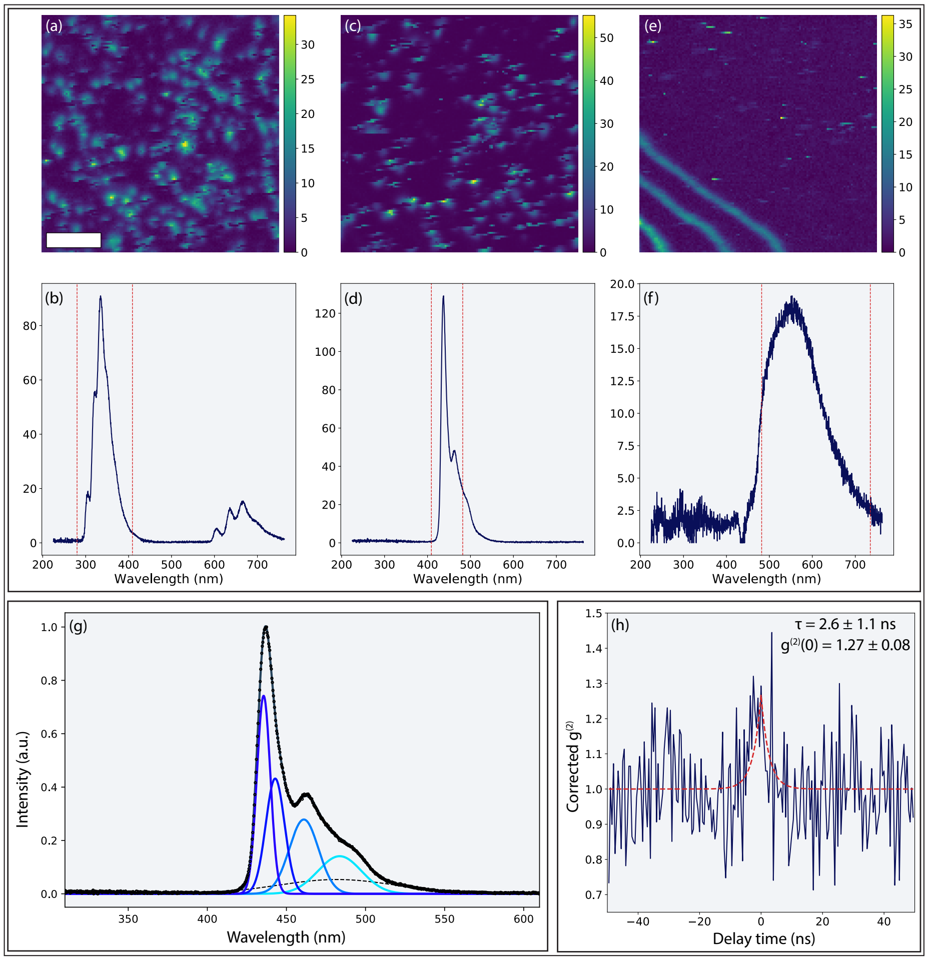

Figure 5.3: Hyperspectral characterization of a dense array of emitters across three spectral regions in h-BN. Hyperspectral CL data are decomposed using Non-Negative Matrix Factorization (NMF) to display the main features of the data. Each image component (top row, scale bar 1 um) shows the spatial distribution of the associated spectral component below (middle row). The red lines on the spectral components in panels (b), (d), and (f) show the edges of the bandpass filters used in bandpass imaging from FIG. 5.2. The spatial (a) and spectral (b) distributions of the first component show point-like UV emitters from 300-400 nm. The peaks between 600-700 nm are artefacts due to the second-order reflections of the UV light from the spectrometer grating. Panels (c) and (d) show the spectral signature of the newly discovered blue color centers between 400-500 nm. Panels (e) and (f) show extended emission features between 500-700 nm, likely caused by extended defects and/or strain. Panel (g) shows a rescaled view of the blue emission component as well as the results of multi-gaussian fitting of the peak. The fitted components show a Zero-Phonon Line (ZPL) followed by several phonon replicas with decreasing amplitude, an indicator of a single-photon emitter weakly coupled to the lattice. The photon-correlation curve in (h) shows a bunching peak, a signature of quantum emission in CL. Fitting to a single exponential decay model gives a lifetime of several nanoseconds, similar to lifetimes observed from SPE in other defects in h-BN.

The first component (see figure 5.7 for an overview of MVA decomposition of the data) is a spatially uniform background that reflects dark counts, noise, and non-localized light emission. The component shown in FIG. 5.3(e) and 5.3(f) shows the light emission of extended line defects, as well as a small number of highly localized features with appreciable intensity that are consistent with previous photoluminescence (PL) studies[43, 42] of SPE in h-BN. FIG. 5.3(a) shows a dense collection of point-like emitters, similar to the UV BP image in Fig. 5.2(b). The spectral features in the component in FIG. 5.3(b)) are a close match to UV SPEs in h-BN seen in previous CL studies[90].

The most striking feature, shown in FIG. 5.3(c) and 5.3(d), closely resembles the spectral and spatial signatures of a typical color center in a wide bandgap semiconductor[43, 88]. Specifically, they are highly localized, spectrally sharp, and the first peak is followed by additional spectral features shifted by tens of meV that are interpreted as evidence of electron-phonon coupling. This component is investigated further in FIG. 5.3(g) using multi-Gaussian fitting of the spectral component. Fitting reveals a series of peaks, decreasing in intensity and increasing in width with increasing wavelength. The spectrum is dominated by a sharp, well-defined zero phonon line (ZPL), centered at 436 nm (2.84 eV), with a FWHM of 10 nm (65 meV), contributing a spectral weight of $\sim 26\%$, followed by several phonon replicas at 443, 461, and 484 nm (2.80, 2.69, and 2.56 eV). There is also a small, broad, background component centered at 482 nm (2.57 eV). In contrast to the UV emission described above (where the phonon replicas have higher intensity than the ZPL), the relatively high intensity of the ZPL compared to the phonon replicas suggest that this emitter's coupling to the lattice is significantly weaker, a desirable quality for possible applications in future quantum information technologies. The density of emitters in FIG. 5.3(c) is higher than in the BP image in FIG. 5.2(d) and is related to the higher electron dose required for hyperspectral imaging, which will be discussed later.

Spectral information from the hyperspectral imaging can be used to perform time-correlation measurements of light from the blue emitters. A bandpass filter is selected that covers a large portion of the emission peak from FIG. 5.3(d) in order to measure the second-order autocorrelation function using HBT intensity interferometry. FIG. 5.3(h) shows the result of this measurement from an ensemble of emitters (See section 5.7 for more experimental details).

The majority of previous studies of light emission in h-BN have measured $g^{(2)}_{PL}(\tau)$ using PL. In stark contrast, $g^{(2)}_{CL}(\tau)$, measured in this study, exhibits a bunching peak as opposed to an anti-bunching dip. This behavior, which has been explored previously[99, 100], is attributed to simultaneous excitation of multiple color centers by the electron beam. In PL studies of defects in wide band gap semiconductors, such as SPEs in h-BN and NV centers in diamond, the excitation energy is typically less than the band-gap of the material, resulting in the production of a single e-h pair per photon. In CL, the excitation energy is much higher than the band-gap of the material, resulting in the excitation of many e-h pairs. A semi-empirical relation predicts that approximately $N_{e-h} = \frac{E_0}{3E_g}$ e-h pairs are excited per incident electron[101], where E_0 is the beam energy and E_g is the band gap of h-BN. For

$E_g = 6$ eV and $E_0 = 3$ keV, $N_{e-h} = 111$.

Previous work[77] has shown that if the bunching peak of the $g^{(2)}_{CL}(\tau)$ function can be attributed to simultaneous excitation of an ensemble of emitters, that the lifetime of the defect state can be extracted similar to an analogous PL measurement of the lifetime from the anti-bunching dip. An exponential fit to the time correlation data using $g^{(2)}(\tau) = 1 + \mathrm{a}\exp\left(-\left|\tau\right|/\tau_{lifetime}\right)$, with a and $\tau_{lifetime}$ as free parameters, gives a lifetime of $\tau_{lifetime} = 2.6$ ns and $g^{(2)}(0) = 1.27$. This lifetime is close in value to previous measurements of SPEs in h-BN[90, 77, 43, 88, 42, 89]. The $g^{(2)}(0)$ value is quite low, but it has been shown that at high current, the bunching effect becomes washed out, resulting in a decreased apparent value of $g^{(2)}(0)$. While the observed bunching peak and extracted fit parameters are not incontrovertible proof that the new color center is a quantum emitter, the presence of this peak is consistent with the newly discovered blue emitter being a potential single photon source.

There are two striking differences between the Blue emitters shown in FIG. 5.2(d) and those shown in FIG. 5.3(c) that are associated with the higher electron dose required to acquire an SI compared to a BP image. First, the number and density of features is higher in the SI, indicating that we are creating new emitters by electron irradiation. Second, a variation in the shape of individual emitters appears. The emitters are round and symmetric in the BP image in FIG. 5.2(d), while many emitters appear to have a truncated shape in the SI component in FIG. 5.3(c). This truncation, discussed below, is associated with a sudden activation or deactivation event while the beam is over an emitter.

To further investigate this, we acquire a 2.5-hour time series of long scan time (262 seconds per image) BP images over a flake of h-BN. Each image corresponds to an exposed dose of $2.3 \times 10^7\ e^-/\mathring{A}^2$ per image, with a total exposed dose of $5.7 \times 10^8\ e^-/\mathring{A}^2$. Time-series data are aligned and registered using template matching and cross-correlation to correct for sample drift during the experiment. Individual emitters were automatically identified in each frame of the time series using the difference of Gaussian blob finding algorithm. 50x50 pixel regions around emitters were extracted and image feature vectors were calculated using the PCA weights of each image. Finally, false positives were removed by inspection of the output of k-means clustering on the feature vectors.

FIG. 5.4 summarizes the results of this experiment. The top row shows the first (FIG. 5.4(a)), middle (FIG. 5.4(b)), and last (FIG. 5.4(c)) images from the time series at full spatial resolution. The colored boxes in the full resolution images indicate regions where we have cropped the data and displayed the entire time series in a 300 nm region around four emitters (FIG. 5.4(d-g)). FIG. 5.4(d) shows an emitter that is suddenly activated by the electron beam (indicated by the truncated disc shape of the emitter), remains in the emissive state for 5 frames, then suddenly switches off for the remainder of the time series. FIG. 5.4(e-f) show emitters that switch on and off several times throughout the scan. Some of these activation/deactivation events appear as truncated discs (shown in detail in FIG. 5.4(h-i)), while some appear as the sudden appearance or disappearance of a bright spot from one frame to another. FIG. 5.4 illustrates that not only are the emitters activated and

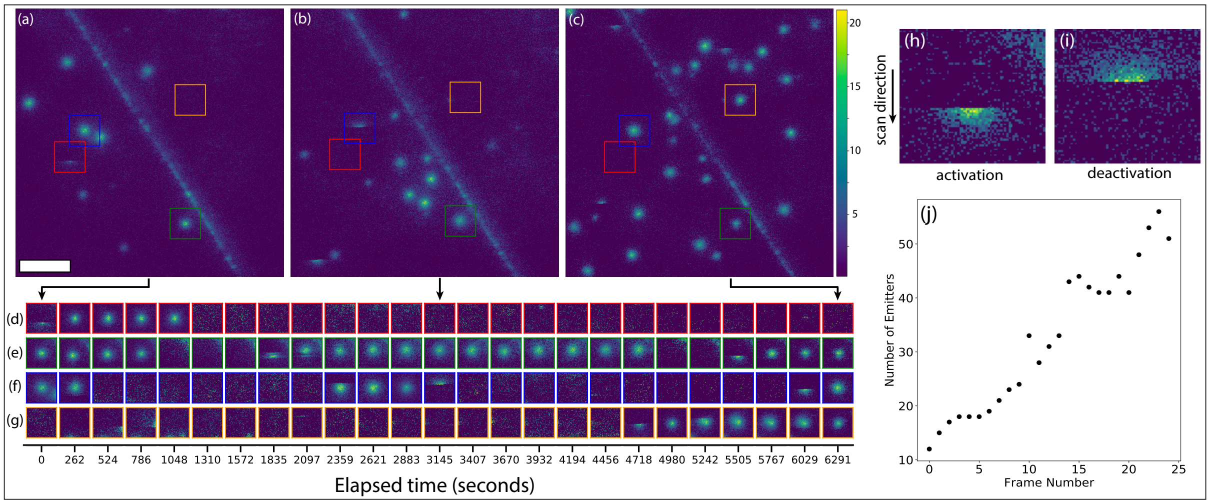

Figure 5.4: Overview of switching behavior in h-BN emitters. A series of CL bandpass images (409- 482 nm) are taken over 1.5 hours at 4.5 minutes per image, with each time point corresponding to a single image scan with an electron beam dose of $2.3 \times 10^7\ e^-/\text{Å}^2$. The top row shows the first, middle, and final images in the series at full spatial resolution (scale bar is 500 nm, color scale in units of counts/pixel). The bottom row shows the dynamic behavior of 4 separate 300 nm regions (indicated by the colored boxes in the top panel) over the entire time series. The emitters exhibit clear switching behavior, turning on and off between frames of the time series. Examples of emitters that suddenly turn on or off as the beam is passing over are shown in panels (h) and (i), respectively. Panel (j) shows that the number of emitters in each frame grows roughly linearly with electron beam dose.

deactivated by the electron beam, but they also disappear and reappear in identical spatial locations (within the accuracy of our measurement)

We note that we have also attempted characterization of these emitters using PL. NIMS-BN samples on indexed Si substrates are seeded with emitters using the SEM, characterized using CL, and then transferred to a CW PL setup using 1 mW 349 nm, 10 mW 405 nm, and 30 mW 532 nm excitation focused to a diffraction limited spot. No emission is observed in the Uv-Vis range using the available excitation energies and intensities within reasonable integration times. This fact, in conjunction with the activation/deactivation behavior observed under the electron beam, hints that the origin of this emission is associated with the charge state of an electron irradiated point defect, similar to SPE in other semiconductor systems[102, 103, 104].

Furthermore, we note that the Blue 435 nm emission is not observed using PL or CL in any samples of commercial h-BN powder. This implies that the new emission may be closely related to the unique synthetic origin of NIMS-BN.

5.5 Discussion

We consider possible mechanisms for the new emission. We immediately rule out the direct creation of defects via knock-on damage and electron-beam-induced heating. The electron energy threshold for knock-on damage in h-BN is in the range of 70-80 keV[50, 105], far greater than the 1-10 keV energy range of the SEM beam. Electron-beam-induced heating is unlikely due to the high thermal conductivity of h-BN along with the relatively low current of the electron beam.

The change in temperature of the sample can be estimated[3] assuming that energy from the electron beam is uniformly deposited in a sphere of radius R using $\Delta\mathrm{T} = 3\mathrm{IV}f/2\pi\mathrm{R}\kappa$, where I is the beam current, V is the beam accelerating voltage, f is the fraction of incident energy that is absorbed, and κ is the thermal conductivity of h-BN (600 W/m K). Assuming that 100% of the incoming power is absorbed in a spherical interaction volume of radius R = 30 nm, a 2 keV electron beam with 1 nA of current causes a temperature increase of $\Delta\mathrm{T} = 0.05$ K. This value would be even lower at increased accelerating voltage[106] because the interaction size scales approximately as $\mathrm{V}^{1.75}$. Furthermore, due to the finite thickness of an h-BN flake, the fraction of energy from the beam deposited into the sample decreases at higher beam energies.

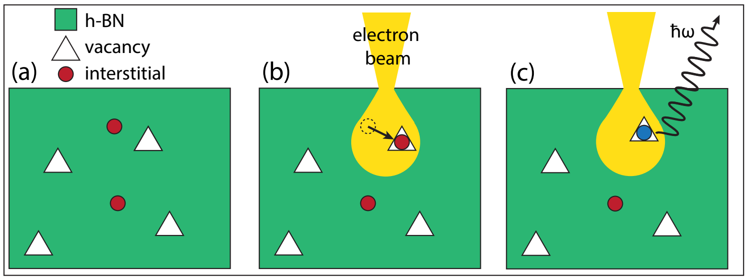

Figure 5.5: Proposed model for formation and activation of blue color centers in NIMS-BN. The as-synthesized material has some intrinsic density of interstitial impurities and lattice vacancies, as shown in (a). When stimulated by the electron beam, the impurity atoms are driven into the vacancies and due to the energy provided by the beam a substitutional defect complex is formed. The charge state of the new defect is changed by the beam causing it to emit photons. The charge state of the defect is sensitive to the intense stimulus from the electron probe and can jump between emissive and non-emissive states, resulting in a blinking effect.

We propose that the origin of this new emitter is electron-beam-induced defect chemistry, outlined in FIG. 5.5. The as-synthesized NIMS-BN crystal has some initial concentration of vacancies and intercalated interstitials, illustrated in the cartoon in FIG. 5.5(a). Electron beam induced diffusion increases the mobility of the interstitials causing the impurities to diffuse towards the naturally occurring vacancies within the material, resulting in the interstitial and vacancy combining into a defect complex[107, 108] (FIG. 5.5(b)). We propose that the activation/deactivation behavior results from electron beam induced charge state switching of the color centers, similar to previous observations of NV centers in diamond[109]. In our model, the electron beam modifies the charge state of the defect causing it to change from a non-emissive to an emissive state, resulting in the production of photons (FIG. 5.5(c)). The charge state of the defect can also be modified in the opposite sense, resulting in emitters switching on and off during a measurement. We do not see any evidence of emitters switching or blinking to a different emission band in our experiments. This effect would be fairly obvious in the SIs and would appear as a distinct component, complementary to the one shown in FIG. 5.3(c) and 5.3(d). The spatial loading would appear as a collection of point-like emitters accompanied by a set of truncated disks (truncated in the opposite sense compared those in FIG. 5.3(c)).

This change in charge state has two possible origins. One scenario is that incident beam and secondary electrons are captured by the defect complex, resulting in a negative charge state. Alternatively, the incident or secondary electrons ionize the defect, resulting in a positive charge state. Currently, neither possibility can be excluded suggesting future experiments and calculations. Previous studies have shown that a low energy electron beam can cause diffusion of impurities or vacancies, vacancy-impurity defect reconstruction, and charge state switching in other wide band gap semiconductors. While speculative, our proposed model is consistent with previous findings of electron beam induced luminescent diamond NV centers[110].

We propose that this emission has not been previously observed in h-BN for several reasons. Past studies of color centers in h-BN have typically not used NIMS-BN which has a unique synthetic origin, but rather commercially obtained h-BN. We surmise that the Ba-B-N solvent precursor used in the NIMS-BN synthesis could produce barium impurities in these samples, which would not be present in commercially obtained material synthesized using different growth precursors. Under the assumptions of our model, the new emission would not be observed in the absence of this unique impurity. PL studies of color centers in h-BN that do use NIMS-BN have used a 532 nm laser excitation to probe the sample and have focused on light emission in a high wavelength range. This excitation energy is too low to probe a state that emits at 435 nm. It is likely that the charge recombination dynamics in this regime are dominated by non-radiative transitions. It is possible that the 435 nm emission is only present using CL because of the large number of electron-hole pairs created per incident electron, as well as the high intensity of the electron probe. A final, more speculative reason that this emission has not been observed to date is the possibility that the particular defect complex responsible for the emission needs the high energy density of the electron beam in order to drive interstitial-vacancy recombination.

Our experimental results of the spectral and spatial character of this new emitter in h-BN show many features observed in quantum emitters, suggesting that this new color center is a potential source of single photons. The emission is highly localized, spectrally pure, exhibits a ZPL with phonon replicas, and can be modified with an electron beam, all features of SPEs in other solid state systems. The bunching behavior seen in the $g^{(2)}(\tau)$ measurement, while not proof of single photon emission, is not inconsistent with electron beam induced light emission from an ensemble of quantum emitters. While all observations are *consistent with* the behavior of a two-level-like system capable of single photon emission, further study is required to unambiguously confirm the quantum nature of this emitter.

5.6 Conclusion

We have identified a new color center unique to high-quality hexagonal boron nitride using cathodoluminescence in the SEM. The emission is peaked at 435 nm and has spectral characteristics indicative of weak lattice coupling. The electron beam activates and deactivates emission from point defects in the crystal. We propose that this emission originates from a barium atom interstitial impurity forming a defect complex with a vacancy driven by the energy of the electron beam. The charge state of this defect is changed by the electron beam resulting in the emitters switching on and off.

5.7 Supplemental Information

Description of $g^{(2)}$ measurement via HBT Interferometry

The electron beam is continuously scanned over a 500 nm square subsection of a h-BN flake containing emissive features in the relevant spectral band. Emitted light is first filtered using a 460/50 bandpass filter (Semrock). The filtered light is coupled to a 50/50 split fiber (Thorlabs TM105R5S1A) using a parabolic reflector. Each end of the split fiber is directed toward a Silicon avalanche photodiode (MPD PD-100-CTE-FC). A 470/100 bandpass filter (Semrock) is placed before each detector to reduce the silicon afterglow effect. Photon timing data are acquired using a PicoHarp 300 (PicoQuant) operated in T2 mode. Timing data are acquired for 30-60 minutes. We monitor the total number of timing events recorded and stop integration between 10-100 million events. Coincidences from the raw timing data are placed into bins between 50-500 ps. We assume that events at long delay times are dominated by the Poissonian statistics of the electron beam and normalize the raw coincides at this level to 1. Finally, we obtain the $g^{(2)}$ correlation function using:

$$g^{(2)}(\tau) = \left(\mathrm{C}(\tau) - \left(1 - \rho^2\right)\right)/\rho^2, \tag{5.1}$$

where $\rho = \mathrm{Signal}/\left(\mathrm{Signal} + \mathrm{Background}\right)$ and $\mathrm{C}(\tau)$ is the normalized coincidence histogram. Background count rates are estimated by measuring the count rate far from an emitter. Typical count rate values are 1-3 kHz for the background and 10-20 kHz for the emitters.

Multi-Gaussian Peak Fitting of Emission Spectrum: ZPL and Phonon Replicas

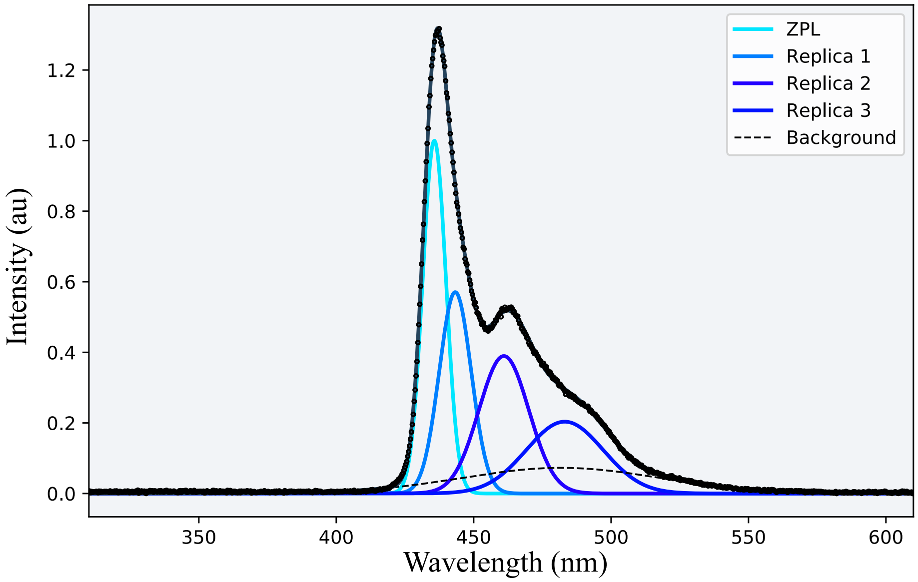

Figure 5.6: Result of multi-Gaussian peak fitting of emission spectrum.

Peak Name	ZPL	Replica 1	Replica 2	Replica 3	Background
Peak Intensity	1	0.571	0.390	0.204	0.073
Center (nm)	435.7	443.3	461.0	483.1	481.8
FWHM (nm)	10.0	13.7	21.4	33.0	84.8
Center (eV)	2.846	2.797	2.690	2.566	2.573
FWHM (meV)	65	87	125	175	456

Table 5.1: Summary of best-fit parameters for multi-Gaussian peak fitting to emission spectrum. Peak positions and widths have been listed in both wavelength and energy units for convenience.

NMF Components and Error Analysis

Spectral image MVA decomposition is performed using the HyperSpy package in the Python programming language. In order to determine the number of components a singular value decomposition is first performed, and the number of decomposition components for the final model is chosen by inspection of the PCA Scree plot. The final decomposition is performed using non-negative matrix factorization (NMF) with the reduced number of final components.

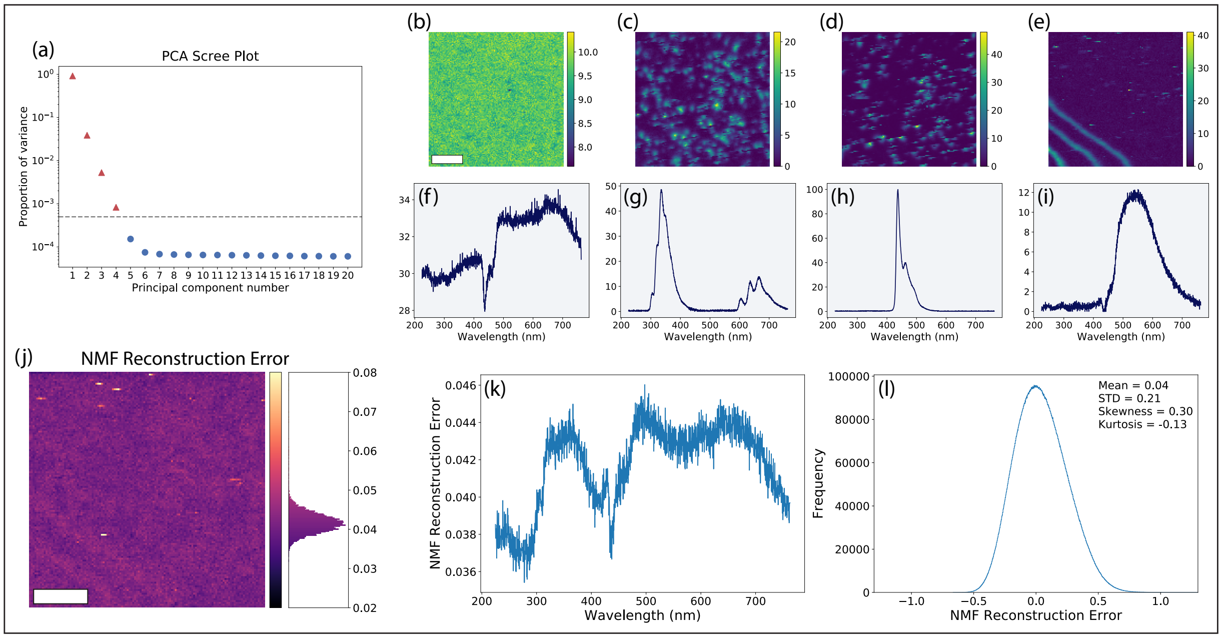

Figure 5.7: Summary of NMF decomposition of hyperspectral data. The number of components was chosen by inspection of the PCA Scree plot in (a). An arbitrary threshold of 0.0005 was chosen. Panels (b-e) show each of the NMF spatial components (loadings) with panels (f-i) showing the associated spectral components (factors). The scale bar is 1 um. The mean reconstruction error per spatial pixel is shown in panel (j). Panel (k) shows the mean reconstruction error per spectral pixel. Panel (l) shows a histogram of the reconstruction error for each voxel of the data set along with selected statistics.

Chapter 6

Nanoscale Engineering of UV-Light Emission in h-BN

"Start every day off with a smile and get it over with."

— W.C. Fields

6.1 Introduction

The ability to reliably create and activate qubits with nanometer scale spatial resolution is essential for next generation quantum information technologies. Systems that utilize photonic circuits are appealing because the computational and information transfer systems could be built around the same framework. In a photonic quantum information system, the polarization states of single photons are used as qubits. Solid-state single-photon emitters (SPEs) are particularly appealing as qubit sources because they offer a high degree of tunability (via the host solid-state system) and scalability (by leveraging existing semiconductor fabrication methods). Hexagonal boron nitride (h-BN) is a particularly promising candidate as a solid-state host for SPEs due to its high chemical inertness and stability as well as the ability to emit single photons at room temperature.

Common methods for creating SPEs in h-BN include thermal annealing [88, 111, 112], irradiation by high-energy particles [37, 112, 113], laser ablation [112, 114], and plasma treatment [115]. These methods offer an effective path for the creation of SPEs, but suffer from limited spatial resolution in the placement of individual emission centers. Recently it has been demonstrated that SPEs in h-BN can be deterministically activated using strain fields created by lithographically defined nanostructures [98]. This method is promising for the ability to create localized SPEs on-demand, but has limited scalability due to the complexity of device fabrication.

Here, we present a method to reliably and deterministically create and activate nanoscopic light-emitting features in h-BN with ~ 50 nanometer resolution using an electron beam.

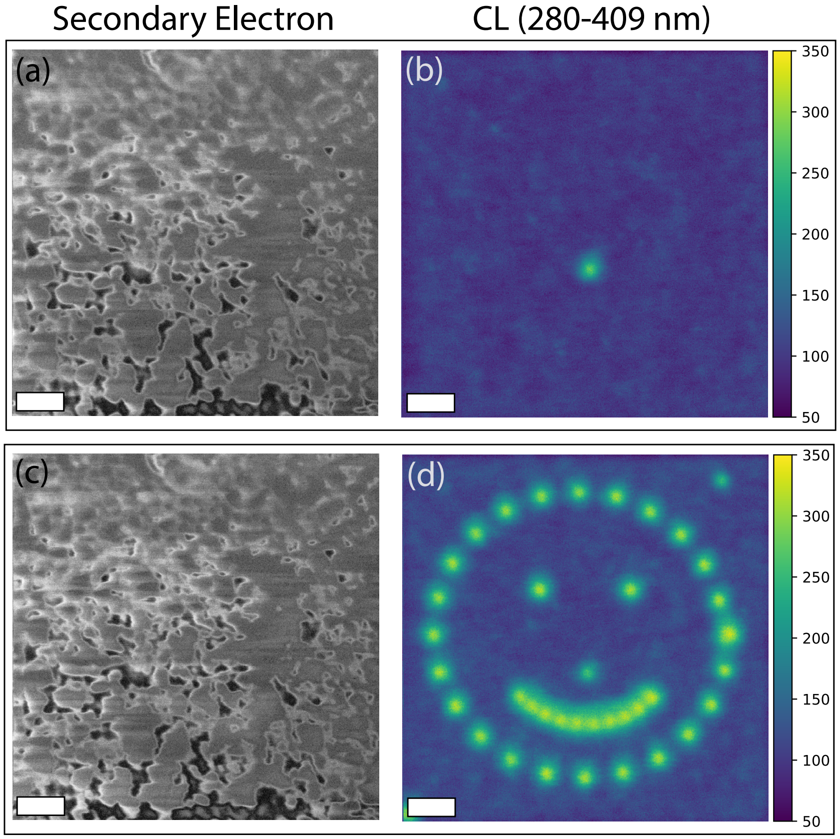

Figure 6.1: Patterned UV light emission in h-BN. The secondary electron (SE) and cathodoluminescence bandpass (from 280 nm to 409 nm) images of a pristine region of h-BN are shown in (a) and (b), respectively. The electron beam is placed at a pre-defined set of positions, dwelling for 1 second at each location, resulting in the light emission pattern shown in (d).The accompanying SE image in (c) shows that the gross morphology of the sample is unchanged. Scale bars are 500 nm.

6.2 Experimental

Our experimental procedure begins with commercially available h-BN powder. The powder contains $\sim 1\ \mu$m thick crystallites with lateral sizes between 10 and 100 μm . The powder is applied to blue wafer dicing tape and mechanically exfoliated to thin the crystallites and align them along the basal plane. The exfoliated crystals are directly transferred to p++ silicon substrates with a few nm thick native oxide layer. The substrates are thermally annealed at 850 °C for 30 minutes under 1 Torr of argon. A set of control samples are also made, which are not thermally annealed.

We use a home made cathodoluminescence (CL) system which is built around a Zeiss Supra-55 SEM (see figure 5.1). Luminescence from the sample is excited by the beam of

1-5 keV electrons. The resulting light is collected by a parabolic mirror and sent down an optical path for characterization. The system use the Molecular Foundry ScopeFoundry software to synchronize data collection from the SEM's secondary electron (SE) and in-lens electron detectors with optical data from either a spectrometer and/or a photon counting photomultiplier tube (PMT). This allows for optical characterization of the material at the spatial resolution of the SEM (∼1 nm), far below the diffraction limit of laser light, usually used for similar photoluminescence (PL) characterization. We use a combination of dichroic mirrors and optical bandpass filters to spectrally filter the UV light emission to the 280-409 nm range before sending it to a PMT to measure the intensity of the emission at each beam position of a raster scan.

Figures 6.1(a) and 6.1(b) show the SE and CL images of a pristine region of h-BN, respectively. There is a fairly uniform spatial background of UV emission and a small bright spot near the center of the image. Our method uses the electron beam to write arbitrary patterns of light emission into the substrate. The beam control software places the electron probe at a set of pre-determined positions and dwells at each location for 1 second. Figures 6.1(c) and 6.1(d) show the resultant light emission on the substrate after the patterning step. We see bright emission spots with diameters of ∼200 nm. The size of the spot is indicative that scattered and secondary electrons are important for the creation of these emitters, as the nominal size of the focused beam is only ∼ 1 nm.

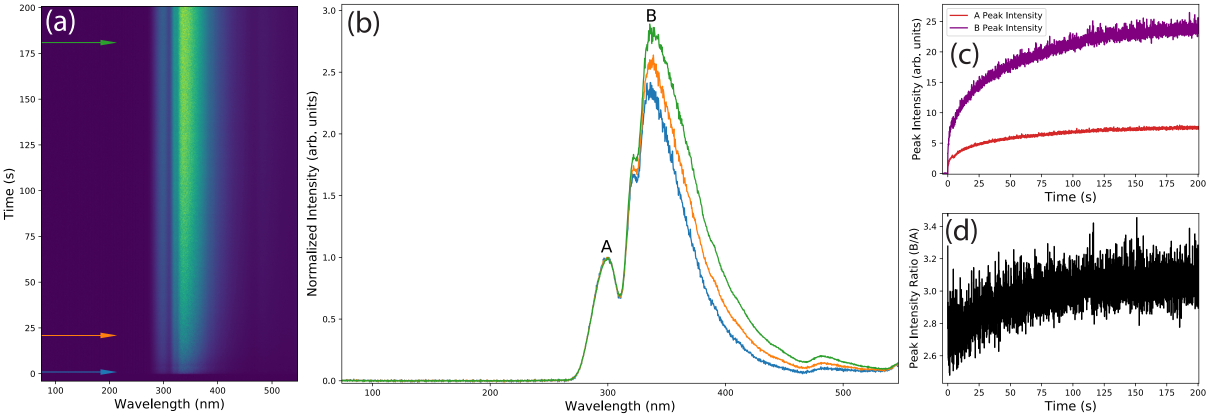

Figure 6.2: Spectral characterization of UV light emission in h-BN. Panel (a) shows the emission spectrum as a function of time under electron beam irradiation. Panel(b) shows three spectra, selected from the time series, normalized to the first peak in CL emission for easy comparison. The colored arrows in (a) indicate the temporal locations each spectra was taken from in the time series. The peaks at ∼ 300 nm and ∼ 340 nm are referred to as A and B. Panel (c) shows the height (not normalized) of the A and B peaks as a function of electron dose. Panel(d) shows the peak intensity ratio (B/A).

Using this method we are able to achieve a half-pitch resolution of ∼ 50 nm for a set of discrete points. In addition to discrete emission spots, this method can also create semicontinuous emission patterns by reducing the step size between patterning locations, as evidenced by the mouth of the face in figure 6.1(d).

The patterned emission spots have high temporal stability; they persist after exposure to air for several months or after a 10 second oxygen and nitrogen plasma treatment. It is important to note that this technique does not create emission patterns on samples that haven't been annealed before SEM imaging and patterning.Thermal annealing is a critically important step for the on-demand formation of UV light emission patterns in h-BN using an electron beam.

We investigate the spectral characteristics of our engineered emission spots using a spectrometer to characterize the light emission as a function of time under electron beam exposure. A pristine region of h-BN is located in the SEM and the electron beam is blanked. Under normal SEM imaging conditions, the dwell time per pixel ($\sim 5\ \mu$s) is much less than the dwell time when patterning (~ 1 s), resulting in the creation of a negligible amount of beam-induced light emission. The spectrometer starts recording and the electron beam is turned on and placed at a stationary location on the h-BN flake.

The spectrum time-series in figure 6.2(a) shows the results of this experiment. A cursory glance at the time-series data indicates that, to a first approximation, the emitted light intensity increases monotonically across the entire emission band as a function of electron

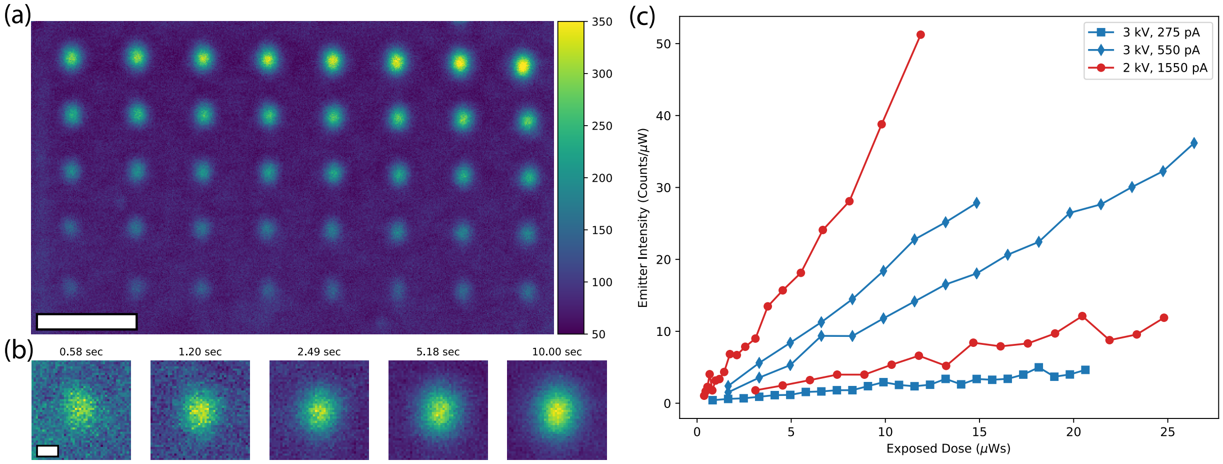

Figure 6.3: Electron dose dependence of emitter brightness. A grid of points was seeded with logarithmically spaced dwell times between 0.5 and 10 seconds, shown in (a). A zoomed in view of selected points is shown in (b), along with the dwell time used to seed each emission spot. Scale bars 1 um (a) and 100 nm (b). The plot in (c) shows that the total brightness of each emission spot (scaled to the power of the beam used to take the measurement) is proportional to the total energy deposited into the spot, even for different beam currents and energies. The slope of each line is different because the total energy deposited into the sample will change for different sample thicknesses, which is not controlled for in our experiments.

dose. Each spectrum has two main peaks at $\sim$ 300 nm and $\sim$ 340 nm, denoted “A” and “B”, shown in figure 6.2(b). Closer scrutiny of the individual spectra reveals that the intensities of the main emission peaks do not grow exactly uniformly, and that an additional shoulder appears in the “B” peak after prolonged beam exposure. Closer examination of the intensities of the A and B peaks over time reveals that the B peak grows slightly faster and brighter than the A peak, as shown by figures 6.2(c-d). The peak intensity versus time plot in figure 6.2(c) and the peak intensity ratio plot in figure 6.2(d) shows that the brightness of both peaks increases rapidly in the first $\sim$ 10 seconds and eventually saturates.

Next, we investigate the relationship between exposure time and emission intensity further by creating arrays of equally spaced spots with different beam dwell times. An example of the result of this procedure is shown in figures 6.3(a-b). The observation that emission spots become brighter for longer dwell times, suggests that the intensity of each spot depends on the total power deposited by the beam. To investigate this hypothesis, the spatial intensity distribution of each spot is fit to a 2D elliptic Gaussian with offset (equation 2.20). The total integrated intensity of each spot is then normalized to the power of the electron beam used to *measure* the emission intensity and is plotted against the total energy received during emitter creation (exposed dose). Figure 6.3(c) shows the spot intensity as a function of dose for 5 different samples, patterned using different accelerating voltages and beam currents.

Each experiment shows that the intensity of a spot grows linearly with the amount of power received from the beam regardless of current or voltage. Each line has a different slope because the amount of power actually absorbed by the sample is different than the power received (see figure 1.3), and depends on the sample thickness, which is not controlled for in these experiments. Likewise, the sizes of the emission spots will strongly depend on the profile of the scattered beam within the sample. This limitation can be overcome by using higher accelerating voltages, thinner samples, and suspended membranes to reduce the amount of secondary electrons and the size of the scattered beam within the h-BN.

6.3 Discussion

Due to technical limitations of our setup, we are unable to measure the photon time statistics of light in the UV region of the spectrum. Therefore, we cannot conclusively determine if our emission spots are localized clusters SPEs. However, comparison of our spectra to confirmed UV SPEs in h-BN [90], shown in figure 6.4, indicate that the light emission reported here has a similar spectral character with peaks at similar wavelengths. The discrepancies between the spectra could be due to different temperatures, illustrated by the differences between the spectra of patterned emission in the same sample at liquid nitrogen vs room temperature, shown in figure 6.4. Also, the relative peak intensities could simply be due to the differences in collection efficiency of the different optical systems used to make the measurements. Finally, the differences could be due to intrinsic differences in impurity types and levels between the samples used here and those of the previous study. As argued in chapter 5, the energy

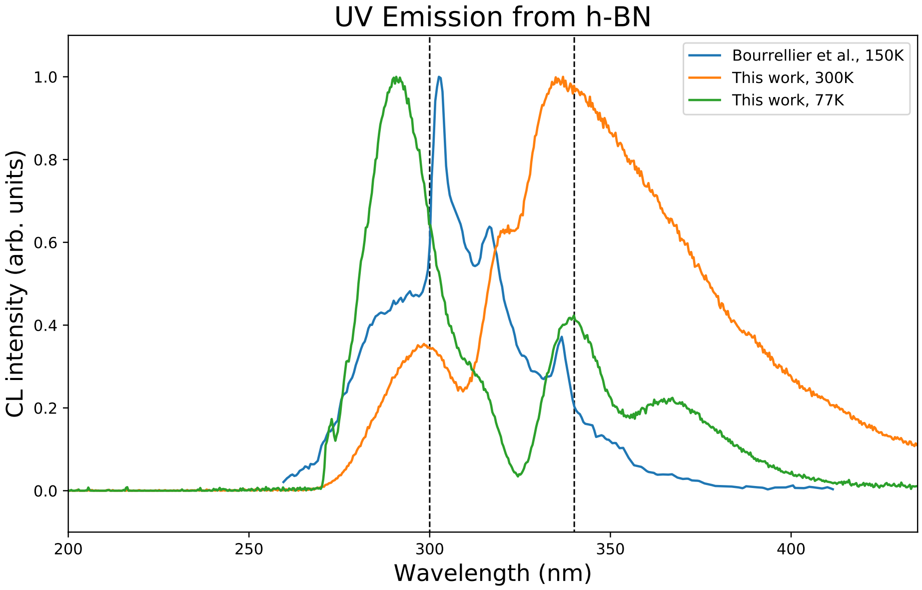

Figure 6.4: Comparison of patterned UV emission to verified single photon emitters in h-BN. The blue curve is reproduced using data from reference [90] from SPEs verified using HBT interferometry. The dashed black lines indicated the spectral band (300 nm -340 nm) over which the light emission is verified to have single-photon character, displaying photon anti-bunching.

landscape of light emission in h-BN is highly sensitive to the atomic species of the impurities and dopants present in a sample. Nevertheless, the high degree of similarity between the spectra observed in this work and previous studies indicate that our emitters are likely sources of single photons.

We outline a model for the observed behavior in Figure 6.5. Our model accounts for all of the major features of our experiment. Namely, the necessity to anneal the sample, the activation of defects using the beam, and the increase in intensity with increased dose. Commercially available h-BN has a relatively high concentration of defects and impurities. These impurities include carbon, oxygen, and absorbed moisture [45]. Annealing removes the moisture from the sample, giving the impurity atoms the ability to diffuse throughout the material. Exposure to the electron beam drives diffusion of residual impurity atoms and vacancies and provides energy to drive the recombination of the two into a defect complex, which acts as a color center where electron-hole pairs can radiatively recombine.

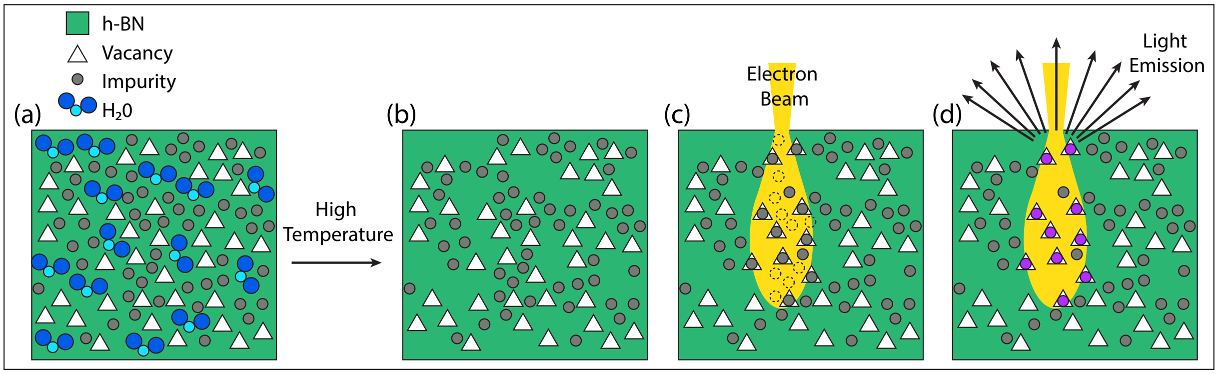

Figure 6.5: Proposed model for mechanism of patterned UV emission in h-BN. The sample initially has a high concentration of vacancies, intercalated impurity atoms, and water molecules, shown in (a). Panel (b) shows that the moisture is driven from the sample after high temperature annealing. Exposure to the electron beam induces diffusion of the remaining impurity atoms into nearby vacancies, as shown in (c). The resulting defect complexes, indicated by purple circles in (d), are now emissive and generate photons under electron beam excitation.

6.4 Conclusion

In conclusion, we present a facile method to fabricate arbitrary patterns of UV light emission in h-BN. We investigate the dependence of electron beam energy and current on the size and intensity of the luminescent regions and find that emission intensity is proportional to the received electron dose for dwell times less than $\sim$ 10 seconds. Our experiments indicate that the total brightness of each spot is linear with the amount of energy absorbed by the material. We show that thermal annealing is a crucial step for the on-demand formation of SPEs in h-BN. We propose that the mechanism for the observed UV emission is electron beam induced diffusion of intercalated impurities into intrinsic vacancies resulting in a luminesncent color center defect complex.

Chapter 7

Synthesis and Characterization of Transition-Metal Dichalcogenides

> *"The strawberries taste like strawberries! The snozzberries taste like snozzberries!"*
>
> — Roald Dahl, *Charlie and the Chocolate Factory*

This first half of this chapter is adapted from a paper published in *2D Materials*, titled "The Important Role of Water in Growth of Monolayer Transition Metal Dichalcogenides", based on work done in collaboration with researchers at The Molecular Foundry at Lawrence Berkeley National Lab [116].

The second half of the chapter outlines a novel data analysis methodology and work flow pipeline developed for characterizing nanocrystalline TMD thin films grown using the aforementioned synthesis routine.

7.1 Introduction

Interest in transition metal dichalcogenides (TMDs) has been renewed by the discovery of emergent properties when reduced to single, two-dimensional (2D) layers. The transition to direct band gap [117, 118], emerging charge density waves [119, 120], high mobility [121, 122, 123], and valley polarization [124, 125, 126] are some of the many exciting properties that have been reported in the TMD literature recently.

A major bottleneck to this research is the lack of reproducible and large scale synthetic methods for high quality, consistent monolayer TMD samples. The dominant growth method is the vaporization and subsequent chalcogenization of solid metal oxides in the presence of gaseous chalcogen precursors. This process is commonly referred to as chemical vapor deposition (CVD) or powder vaporization [127, 128, 129, 130]. Due to its simplicity, CVD is extensively used by the TMD community to produce high quality, micron-sized single crystals [127, 128, 129, 131, 132, 133, 134, 135].

Here, we describe the synthesis of luminescent monolayer TMD islands, multilayer TMD pyramids, TMD nanotubes and fullerenes, and nanocrystalline TMD thin films. We can have developed a methodology to reliably synthesize each of the previously mentioned TMD polytypes by varying three main growth parameters. Using plasma-assisted atomic layer deposition (ALD) to control the quantity of metal oxide precursor, introducing water vapor to control the volatilization and transport of the metal oxide precursor and adding organic molecules to seed nucleation sites for crystal growth.

Understanding the vaporization chemistry of solid transition metal precursors and vapor transport of volatilized precursors, particularly with respect to the influence of water vapor, is critical. Humidity, i.e. water content of the reaction environment, is an important parameter in the gas phase synthesis of inorganic materials, and while it is typically thought of as a contaminant, water is also an effective transport agent [136, 137, 138, 139]. Our experiments demonstrate a direct correlation between gas phase water content and the morphology of the resulting films. In particular, explicit control of the *in situ* water vapor concentration allows us to switch between two modes of growth: one in an effectively dry environment, in which the transition metal oxide source is converted directly to TMD material through a solid state reaction with the chalcogen source, and another in which the transition metal oxide undergoes vapor transport followed by reaction with the chalcogen source.

We find that a small amount of water enhances the volatilization, and hence vapor transport, of the oxides of tungsten and molybdenum at the elevated temperatures (500–800 °C) used in the conversion or growth of their TMD counterparts. We attribute this effect to the enhanced vaporization of WO_3 and MoO_3 in the presence of water, first demonstrated in the 1930s and 1940s [140, 141, 142, 143]. The well-established underlying mechanism is the formation of a volatile mono-hydroxide at elevated temperatures by a reversible reaction [137]. In thermodynamic equilibrium the reaction reads:

$$\mathrm{WO_3(s) + H_2O(g) \rightleftharpoons WO_2(OH)_2(g)} \tag{7.1}$$

$$\mathrm{MoO_3(s) + H_2O(g) \rightleftharpoons MoO_2(OH)_2(g)}. \tag{7.2}$$

Achieving precise control of humidity at ppm levels in CVD reactors poses a significant challenge. First, water is a common contaminant of all commercially available process gases. Second, it is adsorbed on all exposed surfaces and is slowly released during growth. Lastly, the water content of air in a typical laboratory space is on the order of 10,000 ppm, which provides a constant source of available water vapor. In order to ensure a growth environment with precisely controlled humidity, the CVD furnace was regularly helium leak checked and purged with dry nitrogen outside of sample loading and CVD growth. After loading a sample and exposing the furnace to atmosphere, the furnace was pump-purged with ultra-high purity (99.999%) argon before initiating high temperature growth.

With this level of control, we estimate that the baseline gas phase water concentration is ≤ 10 ppm. A schematic of the CVD reactor is shown in figure 7.1(a). Dry Argon is used as a carrier gas during growth and H_2S can be introduced as a chalcogenization agent when desired. The ratio between dry Ar carrier gas and Ar gas from a humidity reference with $c(H_2O) = 394$ ppm water can be adjusted to obtain the desired water concentration in the furnace.

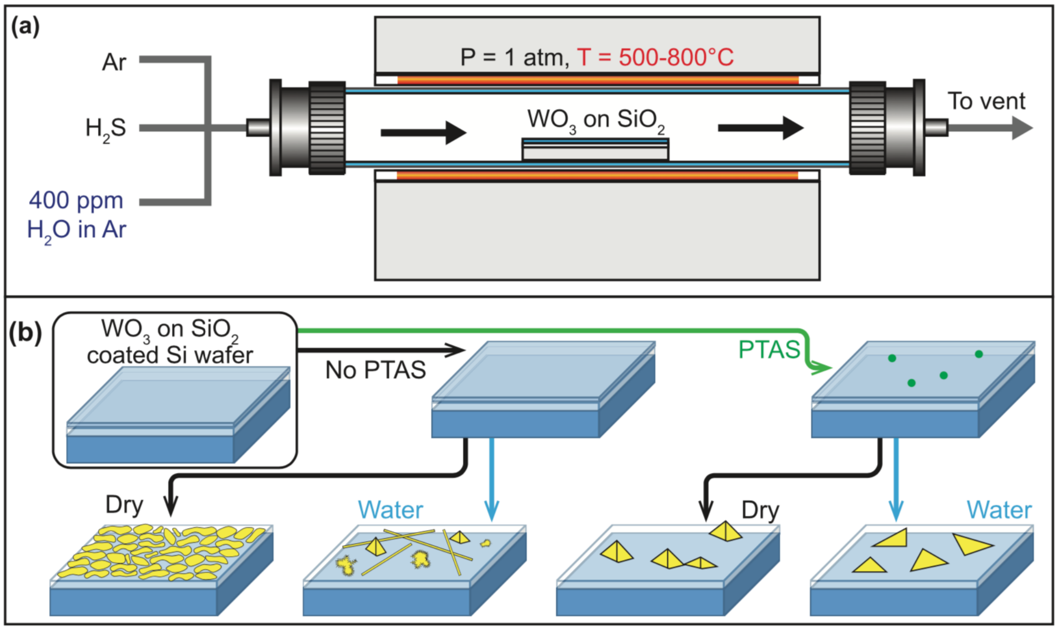

Figure 7.1: Effect of water vapor on the conversion and growth of WS_2 nanostructures from WO_3 films. (a) WO_3 films are deposited on Si/SiO_2 substrates, and subsequently chalcogenized in a tube furnace. Hydrogen disulfide (H_2S) and Argon (Ar) serve as a chalcogen source and carrier gas, respectively. The water content of the atmosphere in the tube is adjusted via a 400 ppm humidity reference. (b) Schematic depiction of the experimental design. WO_3 films are either used as-is or seeded with perylene-3,4,9,10- tetracarboxylic acid salt (PTAS) and then converted under dry or humid conditions, resulting in the morphologies depicted here. Figure courtesy of Christopher Chen.

Control of the chemical composition above the substrate is essential in isolating the factors governing nucleation and growth of thin films, as precursor delivery is especially critical in controlling the morphology of the reaction product. In this regard, solid precursors pose unique challenges (they typically have low volatility and low purity) and it can be challenging to control their evaporation kinetics due to surface and bulk contamination. These issues are further compounded by the high surface area inherent to the metal oxide powders commonly used for CVD. Therefore, in order to probe the effects of humidity on the vaporization of metal oxide precursors and subsequent growth of TMDs, it was necessary to use a source metal oxide that is finite and well quantified. We chose to use tungsten oxide films deposited by ALD as our source material. ALD has the benefit of consistently producing precise amounts of extremely flat materials with sub-angstrom thickness control. By using ultrathin films it is clear when surface transport, vaporization, or conversion has taken place.

One of the major challenges in 2D film growth is controlling nucleation, a critical factor impacting domain size. Recent reports have shown that for CVD, TMD nucleation can be effectively controlled with conjugated organic molecules by simply spin-coating dilute solutions of these 'seed' molecules onto the growth substrate [127, 144]. While the exact mechanism by which the seed molecules nucleate growth remains unclear, it is well documented that they increase crystal quality and allow control over the density of nucleation sites, enhancing reproducibility. Apparent nucleation sites seen in pristine [145] and PTAS-seeded [127] CVD growth of WS_2 and MoS_2 may be preferentially formed when the surface is functionalized with seed molecules [145]. For these reasons we tested the effect of seed molecules in water free and humid growth conditions. Perylene-3,4,9, 10-tetracarboxylic acid tetrapotassium salt (PTAS) was chosen, as it is a widely used seed molecule system.

7.2 Synthesis of Transition-Metal Dichalcogenides via Transition-Metal Oxide Chalcogenation

Using ALD deposited solid oxide precursors, we performed a systematic study with and without water vapor and PTAS seeding molecules. Commercially available silicon wafers with 250 nm thermal oxide were used as substrates. The substrates were conformally coated with WO_3 or MO_3 using plasma enhanced ALD deposition at $T = 40 - 200$ °C. We used bis(tert-butylimido)- bis-(dimethylamido) tungsten and molybdenum hexacarbonyl as precursors for WO_3 and MoO_3, respectively, and oxygen plasma in an Oxford Instruments FlexAl ALD system. The ALD growth rate was calibrated using fixed angle *in situ* spectroscopic ellipsometry (Woollam M-2000). The final thickness of the metal-oxide precursor substrate was controlled by varying the number of ALD cycles with a growth rate of 1 Å/cycle.

A schematic outline of our experimental approach is presented in figure 1(b). In the control experiment, metal oxide coated substrates were exposed to H2S in a dry environment, resulting in the direct conversion from the oxide to a polycrystalline sulfide. When water vapor was introduced, the morphology of the surface was drastically changed to a mix of few-layer, multilayer, and wire-like structures. A second set of oxide substrates were spin-coated with PTAS seeding molecules to enhance nucleation. In dry conditions, crystalline TMD multilayer islands separated by bare silicon dioxide were formed. However, with the addition of 100 ppm of water, PTAS seeded substrates yielded crystalline TMD monolayer triangles. Figure 7.2 shows scanning electron microscopy (SEM) images, atomic force microscopy (AFM) images, and Raman/photoluminescence (PL) spectra for each of the experimental conditions described.

Figure 7.2 shows a WO_3 film converted to WS_2 in a dry reactor. The conversion process of thin transition metal oxide films into transition-metal dichalcogenide films has been previously demonstrated [146, 147, 148, 149]. However, we note that our study also demonstrates that this direct, solid state conversion is only possible in the absence of moisture. The resulting film is composed of small, densely packed grains of WS_2. This can be seen in the SEM and AFM images, which are effectively featureless, and in the Raman/PL spectrum, which clearly demonstrates the presence of WS2 uniformly over the substrate. The low apparent PL intensity is likely due to the presence of small crystalline domains (10 nm), where edge

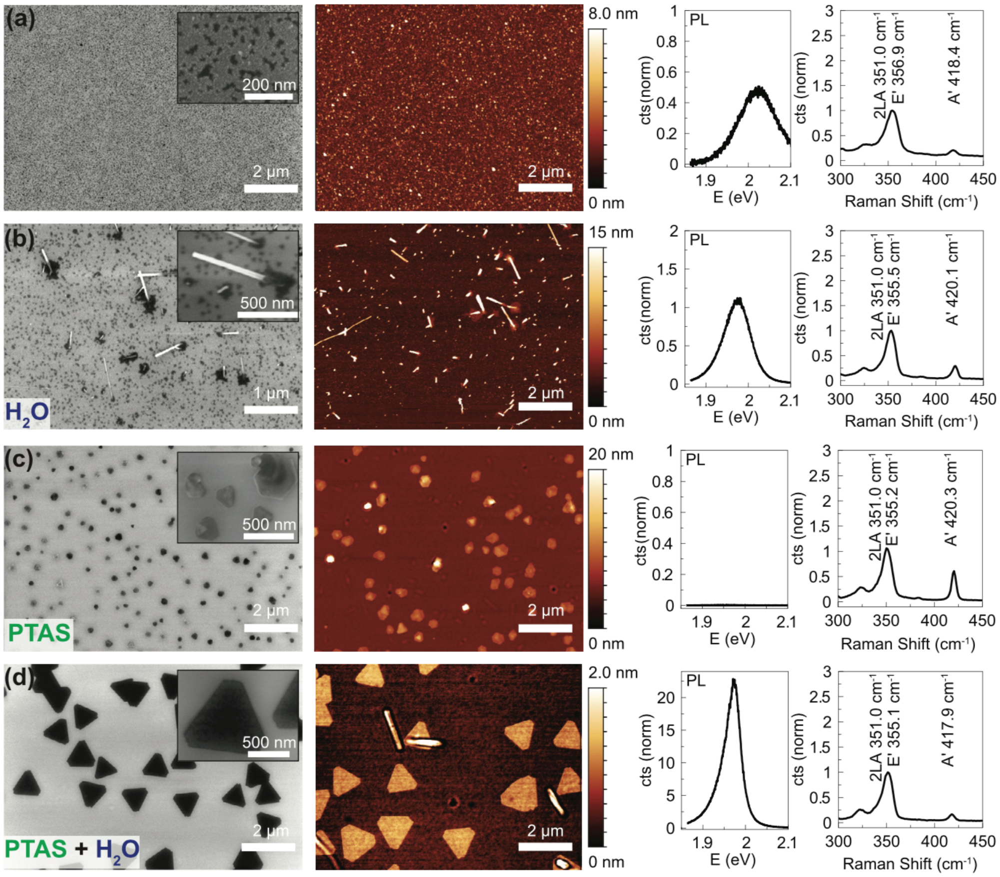

Figure 7.2: Characterization of WS_2 nanostructures grown under various conditions. The nanostructures are characterized by SEM and AFM (first and second column), as well as Raman and photoluminescence spectroscopy (third column). The spectra are normalized to the Raman mode intensity at $351\ \mathrm{cm}^{-1}$. Conversion of 1 nm thick WO_3 films into WS_2 at T = 800 °C, H_2S flow of 5 sccm and Ar flow of 250 sccm (a) in dry Argon atmosphere, (b) in the presence of 100 ppm water vapor, (c) with seeding molecules on the substrate and (d) with both 100 ppm water vapor and seeding molecules on the substrate. Figure courtesy of Christopher Chen.

defects dominate the optical properties of the film. It should be noted that these films show a significant blue shift in their PL spectrum and in the in-plane vibrational modes compared to larger, single crystal monolayers. These observations could be due to the presence of compressive strain in the polycrystalline films [150, 151].

As shown in figure 7.2(b), the addition of 100 ppm of water resulted in drastically modified film morphology compared to the water-free case. The SEM and AFM images are dominated by the presence of tube or wire-like structures, multi-layer patches, and some single layer regions of WS_2. Further analysis with transmission electron microscopy (TEM) identifies some of the additional structures as WS_2 inorganic fullerenes and nanotubes in addition to the layered structure (figure 7.3).

An electron transparent sample with a variety of WS_2 polytypes was prepared on a Si_3N_4 window in a Si frame prepared using conventional photolithography and etching techniques. 10 nm of SiO_2 was deposited onto the windows with PE-ALD in order to approximate the thermal oxide substrates. 2 nm of WO_3 was deposited onto the windows, and the surface was functionalized with 50 μM PTAS before growth. Growth was done at 650 °C with 100 ppm of water vapor.

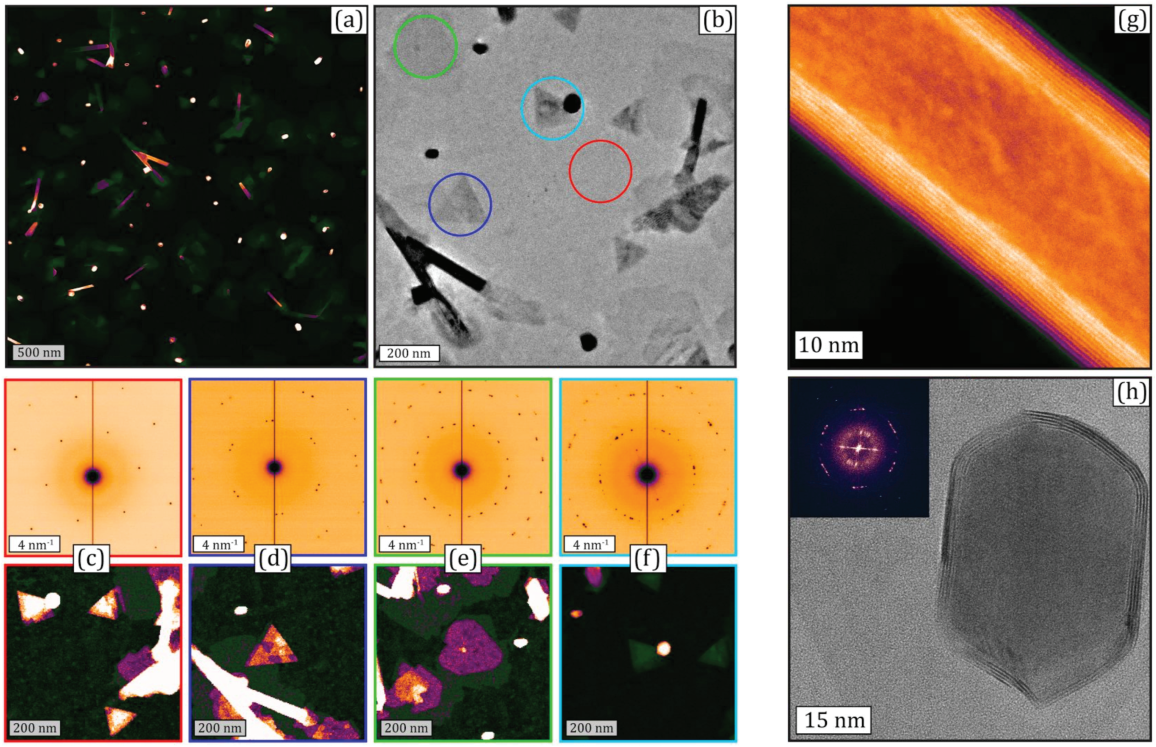

Figure 7.3: TEM identification of nanostructred WS_2 grown directly on an SiO_2/Si_3N_4 membrane. A variety of morphological polytypes can be seen in both HAADF STEM (a) and BF TEM (b) images of same area. To highlight the structural differences between each of the regions, selected area electron diffraction patterns (∼180 nm spot, top) and HAADF STEM images with adjusted contrast to show features of interest are presented for monolayer single crystal films (c), multilayer triangles on a larger film (d), multilayer islands (e), and a triangle and an inorganic fullerene (f). Further evidence of the nanotubes and inorganic fullerenes can be resolved with a representative higher resolution HAADF STEM image of an individual tube (g) and BF TEM of an individual inorganic fullerene with an inset FFT (h) respectively.

These additional phases were first observed in the conversion of W thin films to WS_2 and subsequently extensively studied by Tenne *et al* [152, 153, 154, 155, 156]. We hypothesize that the oxide after water-assisted volatilization has a morphology containing roughly spherical and elongated oxide structures, which are then converted into inorganic fullerenes [153] and nanotubes [156] respectively. Both Raman and PL reveal a combination of bulk material and monolayers. The monolayer regions show significantly increased PL and Raman intensity over the water-free case as well as an increased separation between the E^1_{2g} and the A^1_g mode of 65.5 cm^{-1}, likely due to the presence of few-layer domains. Large regions of the substrate do not show Raman nor PL signatures that are characteristic of WS_2, suggesting that they are completely bare. From these observations it is clear that even small concentrations of water have a significant impact on the volatility and mobility of WO_3 during the growth process.

Figure 7.2(c) shows the result of inclusion of PTAS during the dry conversion process. SEM and AFM imaging reveal bulk crystals over the entire surface, which were confirmed to be WS_2 by Raman spectroscopy. The regions between the crystallites are bare, and no WS2 or residual WO3 was observed. Furthermore, the consistent shift of the out-of-plane vibrational mode by about 1–3 cm^{-1} and the lack of observable PL clearly preclude the existence of single- or bi-layer regions on the surface. Considering that under identical conditions, but without the seed molecules, the thin WO_3 films directly convert to WS_2, it is apparent that the seed molecules nucleate crystals which then coarsen during the growth process.

We now examine the effect of seeding molecules on the growth process in the presence of water. While we have already shown that water greatly increases the volatility of the WO_3 precursor and that seed molecules have a strong effect on the growth process, the combination of these two produce remarkable results, as shown in figure 7.2(d). With ~100 ppm of water vapor, micron-sized, monolayer single-crystalline islands form over the entire surface, as shown by SEM and AFM imaging. Across the growth substrate, the crystals showed uniformly intense PL, and the Raman spectra match those reported for monolayer WS_2. The triangular islands are separated by bare SiO2, as confirmed by Raman spectroscopy.

At intermediate water vapor concentrations, between the baseline and 100 ppm, the resulting morphology was an intermediate of the bulk crystalline and monolayer islands seen for dry and 100 ppm water seeded growth, respectively. At higher water vapor concentrations, the volatility of WO_3 was enhanced such that WS_2 could not be found after growth.

7.3 Synthesis and Characterization of Transition-Metal Dichalcogenide Nanotubes

For very high water vapor concentrations ($\gg$ 100 ppm), 5-10 nm WS_2 ALD films converted directly on SiN TEM membranes resulted in a high density of nanotubes. Figures 7.4 and 7.5 summarize the TEM characterization of these nanotubes.

The nanotubes form a continuous forest over the entirety of the growth substrate. They rest on a bed of continuous single- and multilayer WS_2 islands. They are 10-30 nm in diameter,several microns in length, and highly crystalline. Many of the tubes have a filled core containing unconverted WO_x rods. The nanotubes appear to grow from nucleation site on multi-layer TMD islands. We hypothesize that the growth of nanotubes results from the formation and subsequent conversion of WO_x nanorods templates.

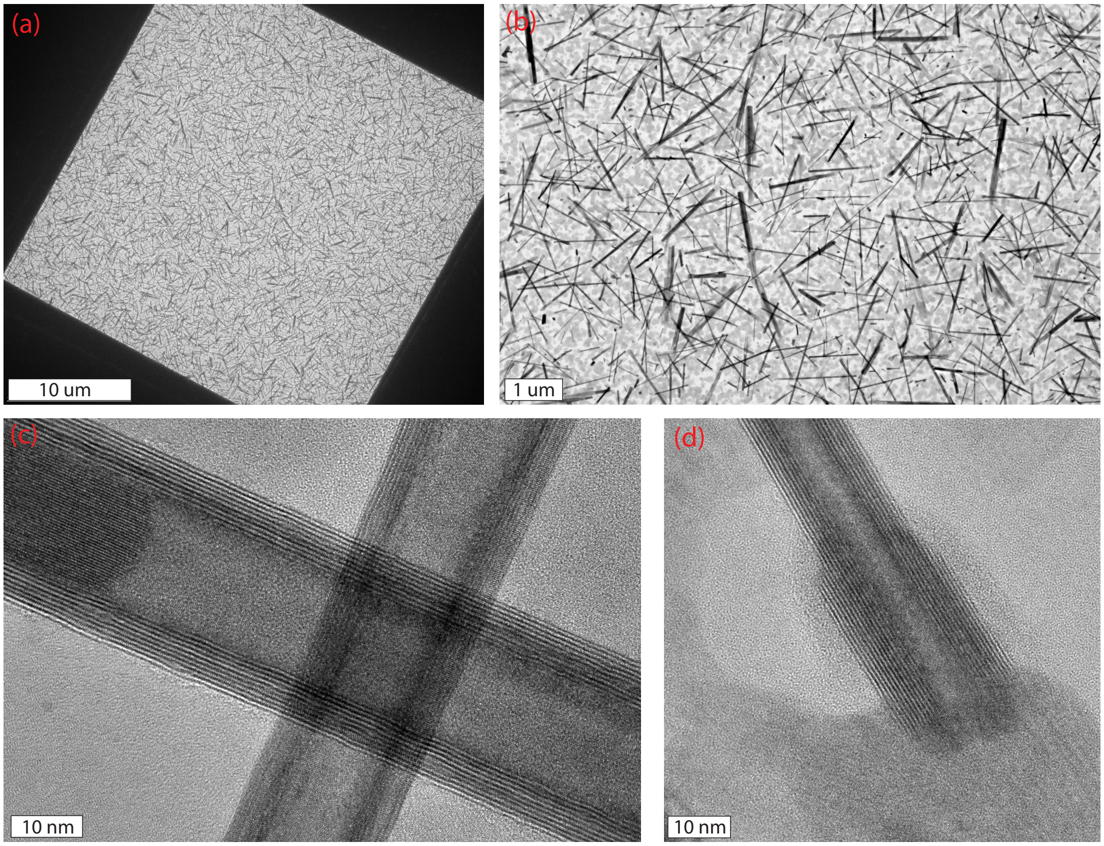

Figure 7.4: TEM charcterization of WS_2 nanotubes grown directly on an SiO_2/Si_3N_4 membrane. The oxide film is entirely converted to a forest of nanotubes that is continuous over the entire growth substrate, evidenced by the low-mag TEM image in panel (a). Also present are single- few- and multilayer- islands of WS_2, as shown in panel (b). Inspection of the data also reveals that many nanotubes are filled with tungsten oxide nanorods. Panel (c) shows that the nanotubes and the WO_x filling (top left) are highly crystalline. Panel (d) shows how the nanotubes are seeded from nucleation sites on the WS_2 islands and they grow.

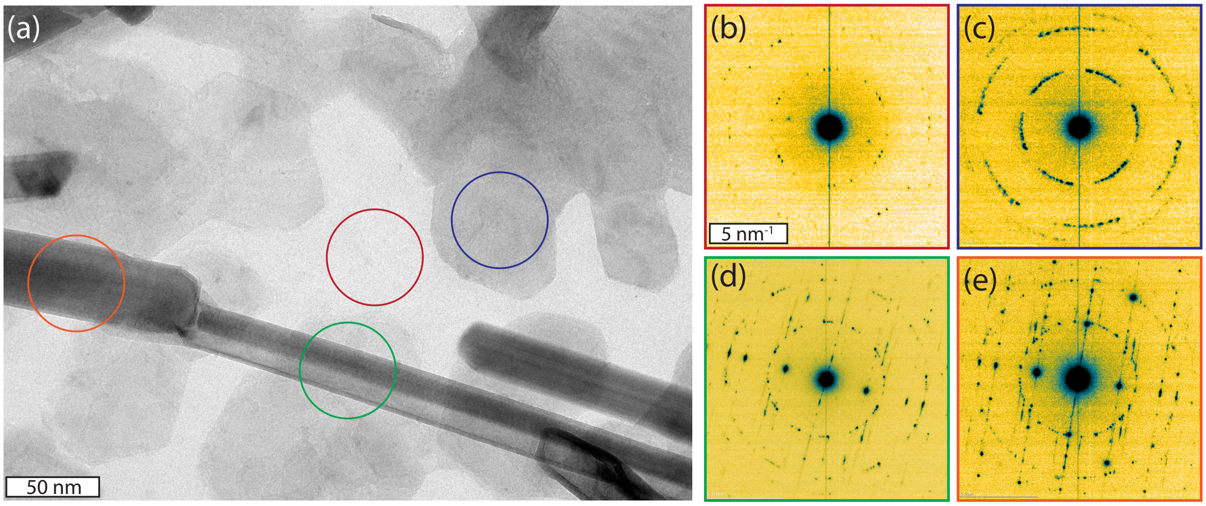

Figure 7.5: Select-Area Electron Diffraction (SAED) analysis of WS_2 nanotube synthesis. The diffraction patterns in (b-e) were taken from the regions marked by the colored circles in (a). This type of characterization allows for the unambiguous assignment of crystal structure to each nanostructure in the sample. The lightest regions of the TEM image are single- and few- layer WS_2 with domains sizes of ~20-50 nm (panel (b)). The darker islands, are multilayer WS_2 that are stacked with random twist angles between adjacent layers (panel (c)). The nanotubes are of mixed chirality, and many are filled with tungsten oxide nanorods (panels (d-e)).

7.4 Information Theoretical Approach to Characterizing TMD Thin Films

Polycrystalline TMD thin films can be grown at wafer scale and lend themselves to scalability [129, 148]. These films have a high density of intrinsic grain boundaries and other defects that can influence physical properties and drive exotic correlated electron effects and emergent phenomena [120]. In this section, we show how to employ 4DSTEM on large area polycrystalline WS_2 thin films to fully characterize the local crystalline texture and structure.

WS_2 (see section 7.2 for synthesis methods) films are supported by an electron transparent SiN membrane. Figure 7.6(b) shows a conventional STEM image of the thin film acquired using an annular dark field (ADF) detector. The contrast in this image indicates differences in thickness, mass density, and local crystallography of the sample. The bright regions are the thin film, the dark regions are voids, and the very bright spots are regions of contamination. The sample presumably has a distribution of grain sizes and orientations, but this is not directly apparent from the STEM image of Fig. 7.6(b).

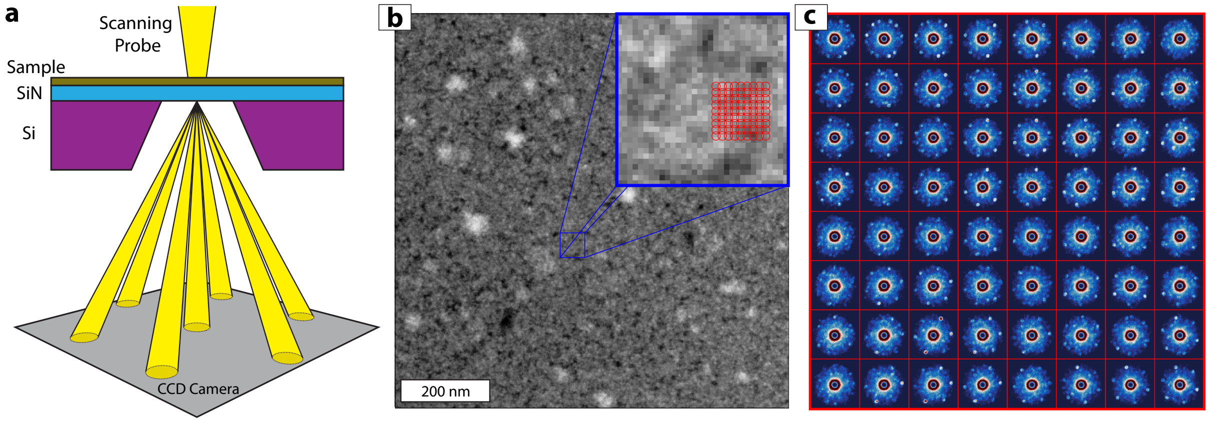

Figure 7.6: Experimental setup for 4DSTEM measurements of TMD films. (a) A small convergence angle probe of electrons is rastered across a thin sample suspended across a supporting frame (typically with a window). A CCD detector in the back focal plane records the electron count (reflecting the diffraction pattern) at each probe location, thus measuring the local crystallography of the sample with nanometer scale resolution. The films are synthesized by converting WO_x films deposited directly onto SiN TEM membranes. (b) High-angle annular dark-field (HAADF) signal. The blue box (inset) is a zoom-in (7X magnification) for the small blue square area outlined in the center of the image. (c) 64 representative diffraction patterns acquired for the WS_2 sample at the spatial locations identified by the red grid in (b). The diameter of the red grid circles in (b) indicates the approximate probe size. In (c), each red box represents a spatial pixel of size 2 nm sampled by a 2.7 nm probe; the field of view of the diffraction pattern within each red box is 10.8 nm^{-1}.

In a 4DSTEM experiment (figure 7.6(a)), we acquire diffraction data over a wide area of the sample. This is in contrast to traditional dark-field (DF) TEM imaging, where a physical aperture is placed in the diffraction plane of the instrument at the location of a Bragg spot, resulting in an image formed by Bragg scattered electrons that have passed through the aperture. DF-TEM characterization uses a series of aperture images, acquired at several aperture positions, to construct a map of the spatial distribution of the crystalline grains in a sample [20, 19]. In contrast, 4DSTEM simultaneously acquires all possible aperture positions, including those that do not fall directly on a Bragg peaks.

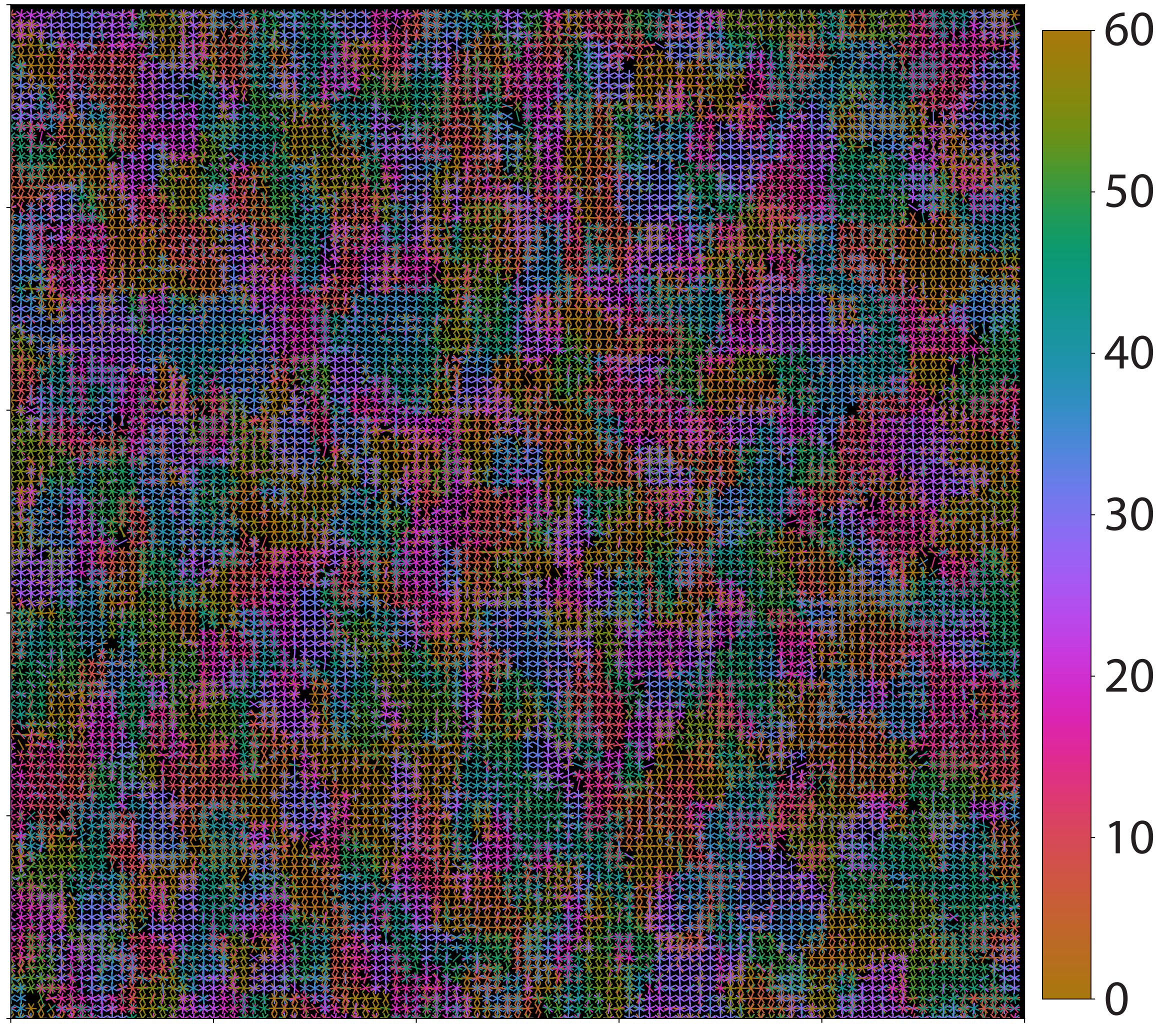

Figure 7.7: Visualization of grain structure in WS_2 thin film. Peaks are detected in the diffraction pattern at each spatial location of the 4DSTEM data. The angle of each peak is extracted and used to generate the colored lines shown in the figure. The color scale indicates the angle of each line, modulo 60 degrees. The image field of view is 200 nm.

The red circles in the inset of figure 7.6(b) correspond to approximate positions of the probe during the 4DSTEM mapping. Figure 7.6(c) shows a visualization of the associated raw diffraction pattern data. Each red box in Fig. 7.6(c) presents spectral data collected from the corresponding spatial pixel (red circles) in Fig. 7.6(b). It is apparent that each diffraction pattern has a mixture of two main features: sharp, bright spots arranged in an approximately hexagonal pattern arising from Bragg scattering from the crystalline planes of the thin film and an (approximately) azimuthally symmetric diffuse component that arises from the amorphous support substrate (the highly saturated central spot due to unscattered electrons contains no useful information and has been masked in Fig. 7.6(c)).

The data of 7.6(c) hint at differently oriented crystallites (i.e. domains) with hexagonal symmetry within the sample. However, the true rotational symmetry and detailed domain structure are not easily accessible by simply eyeballing these data. In fact, as we find below, the rotational symmetry in this specimen is not six-fold at all. This illustrates the general difficulty of directly visualizing or assigning unambiguous meaning to higher dimensional data sets.

Figure 7.7 shows the results of a traditional analysis of the 4DSTEM data. First, Bragg peaks are detected in 10 randomly chosen diffraction patterns using difference of Gaussian (DoG) blob detection. The detected blobs are extracted and averaged together to create an exemplar for the diffraction spots to be used as a template. Next, Bragg peaks are detected in each diffraction pattern of the 4DSTEM data using cross-correlation matching of the template. This preliminary set of located peaks is filtered by removing any matches that fall outside of a well-defined range of reciprocal space radii ($3.43\ \mathrm{nm}^{-1} \leq q \leq 3.94\ \mathrm{nm}^{-1}$), corresponding to the in-plane reciprocal lattice constant of WS_2 ($q_0 = 3.67\ \mathrm{nm}^{-1}$). Finally, the image shown in figure 7.7 is generated by drawing lines corresponding to the orientations of all detected peaks at each spatial pixel. The color scale indicates the angle, in degrees, of each Bragg reflection modulo 60 degrees.

Figure 7.7 reveals that the specimen is comprised of many small grains with lateral sizes on the order of ten nanometers. The majority of the grains do not overlap, but there are regions on the sample with multiple grains in a single location. The result presented in figure 7.7, while striking, is time consuming to construct and detailed knowledge of the sample is required to perform the data analysis. Furthermore, even though the image presented in figure 7.7 has a significant reduction in size and dimension compared to the original data, there is still too much information density to allow the facile extraction of the most relevant material properties (*e.g.* the exact distribution of grain sizes and orientations.)

We now apply our MVA methodology, outlined in Fig. 7.8. Before MVA decomposition, the data is pre-treated. Many MVA techniques are highly sensitive to small shifts and outliers in data, which can either be a blessing or a curse. In order to minimize artefacts in the MVA output, the data are first aligned (there are small shifts in the diffraction patterns from different spatial pixels) and outliers are removed (cosmic rays result in “hot pixels” and the intensity from the central beam is highly saturated).

The shifts between diffraction patterns are calculated by cross-correlation of the central beam, enhanced by a noise reducing Gaussian filter follwed by an edge-finding Sobel filter.

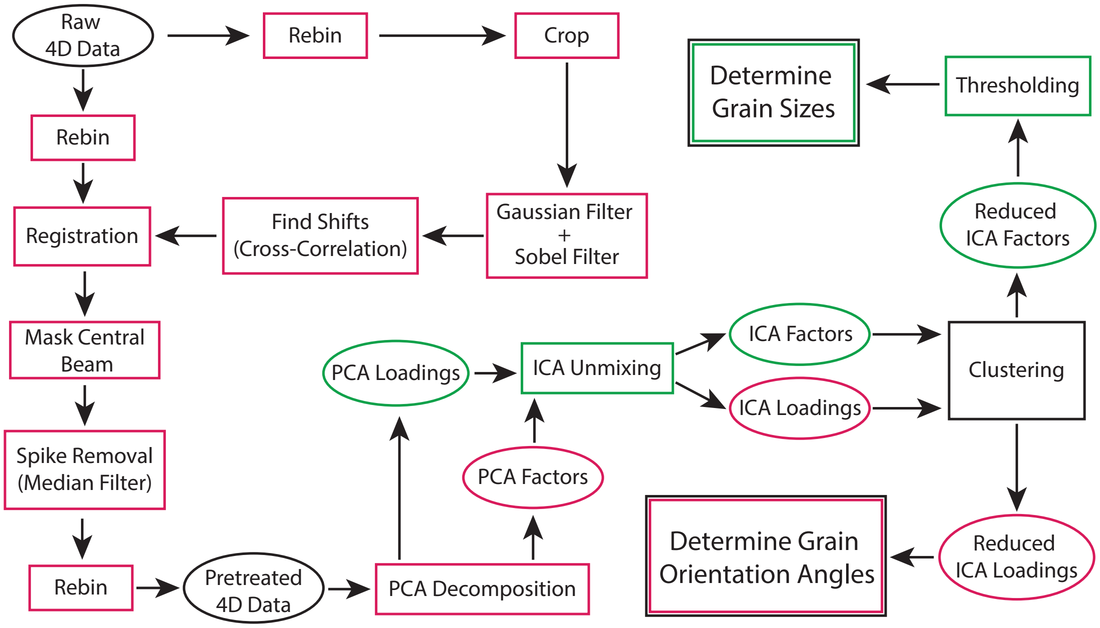

Figure 7.8: Flowchart for MVA workflow of 4DSTEM data. Red items denotes spectral pixels while green denotes spatial pixels. Rectangular boxes are operations and ovals are data.

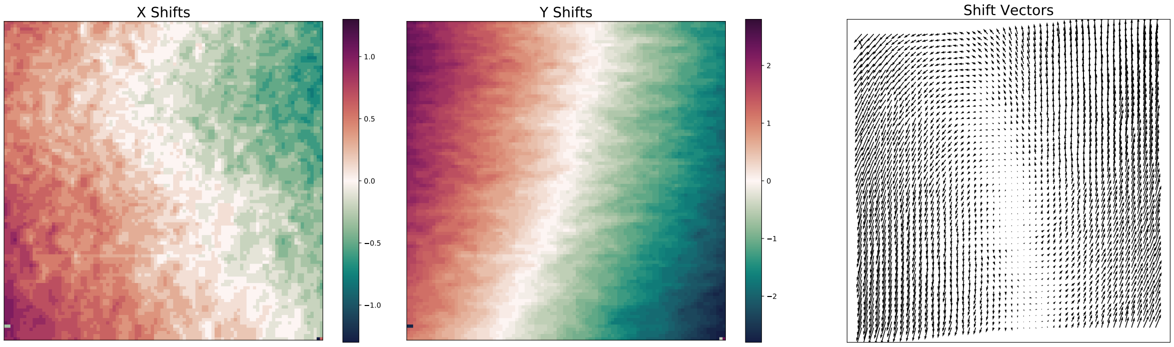

Figure 7.9: Measured shifts for diffraction patterns from 4DSTEM data from polycrystalline WS_2. The x and y shifts are measured with sub-pixel precision at each spatial location and the associated diffraction pattern is shifted to bring the data into registration. The field of view of each image is 200 nm.

The results of data registration are shown in figure 7.9. Next, hot pixels are removed using a 3x3 median filter and the intensity from the central beam is masked with a circular disk. The final data pre-treatment step is to rebin each diffraction pattern to make the size data more manageable and reduce the computation time of each step. The data set presented here is reduced to a size of $(100 \times 100 \times 256 \times 256)$ from an original size of $(100 \times 100 \times 512 \times 512)$.

The first step of the MVA portion of the data analysis workflow is PCA decomposition. Fig. 7.10 shows the primary features of the PCA decomposition. The first several components (1-5) are the most important and they indicate clear spatial structure. We observe a rotationally symmetric component, related to the mean response of the sample, as well as azimuthally varying ring shaped components which describe the intensity of the Bragg spots throughout the sample. The next components (15-19) have less clear spatial structure, but decidedly more complex spectral structure which describe complicated intensity variations of the diffuse background. Components 50-54 have no discernable spatial structure and a spectral structure that has no immediately clear meaning. The final components (500-504) have no structure either spatially or spectrally and show the descent of the components into random noise.

One of the biggest challenges for MVA analysis of data is the determination of the number of components to keep and discard. The PCA scree plot and it's related quantities are useful tools for assessing this number. Figure 7.11 outlines the process of component number analysis. The Scree plot (fig. 7.11(a)) shows what proportion of the total variance each component adds to the data. The integral of the Scree plot (fig. 7.11(b)) shows how much

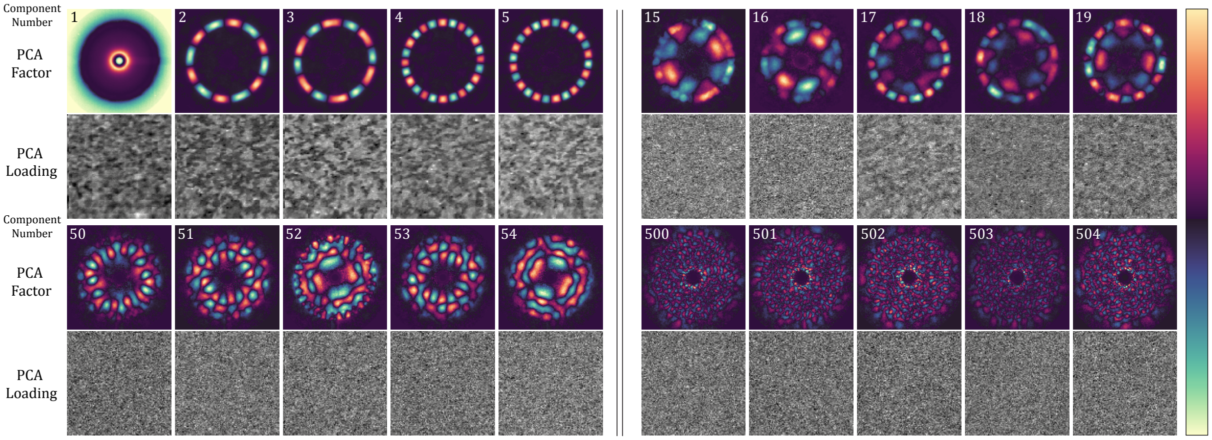

Figure 7.10: Results of the principle component analysis (PCA) for polycrystalline WS_2. Selected k-space PCA factors (analogous to diffraction patterns) above their associated real space PCA loadings (analogous to images) are shown above. Similar to Fourier decomposition, the data are expressed as a linear combination of a new basis. This information basis describes the variance of the data. The first member describes the highest variance, the second member the second highest variance, and so on. As the basis component number gets higher the k-space PCA factors and associated real space PCA loadings move from describing the intensity of the primary diffraction spacing (components 1-19), to describing the intensity of the amorphous substrate (components 15- 54), to finally the noise of the detector (components 500-504). The field of view of each PCA factor and loading is 10.8 nm^{-1} and 200 nm respectively.

each component adds to the cumulative variance, and is also a useful metric for determining the final number of components. The RMS reconstruction error (defined by eq. 2.8 and shown in fig. 7.11(c)) can also be used to determine the number of components.

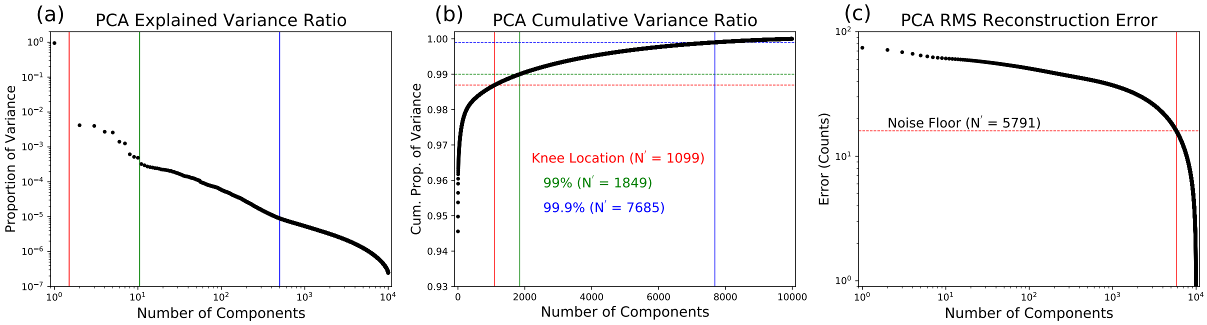

Figure 7.11: Determination of number of PCA components using Scree plot and reconstruction error. The internal structure of the PCA Scree plot, shown in in panel (a), shows four regimes of components, delineated by the red, green, and blue vertical lines. The colored lines in the cumulative PCA Scree plot in panel (b) show three (arbitrary) cutoffs for dimensional reduction, listed on the figure. Panel (c) shows the RMS reconstruction error, along with the noise floor of the detector.

Inspection of figure 7.11(a) reveals that there are four distinct regimes of components, denoted by the vertical colored lines. Each regime of the scree plot has a distinct structure. The first component alone accounts for nearly 95% of the total variance in the data (left of the red line). The curve defined by the components in the second regime (left of the green line) has a distinct shape, and each component accounts for between ~ 0.1 and 1% of the variance in the data. The remaining two regimes (left and right of the blue line) appear as a smooth curve with an elbow around 500 components. These values (1, 10 and 500 components) are useful starting places for choosing an output dimension for the data to inspect general features of the PCA decomposition.

A more quantitative, and possibly rigorous, method for choosing the final dimension is to keep all components below an arbitrary threshold in the Scree or cumulative variance plots. Figure 7.11(b) shows three different choices of cutoff, the knee of the curve (red), 99% of the total variance (green), and 99.9% of the total variance (blue). In this plot, the vertical lines indicate the final output dimension and the horizontal lines indicate the threshold.

Figure 7.11(c) shows the RMS Reconstruction error as a function of the final number of components, calculated from equation 2.8. By setting the cutoff using the noise floor of the CCD detector of the microscope, PCA decomposition allows for lossless data compression and storage.

The PCA components are orthogonal and thus do not necessarily describe physical processes. In order to decompose the PCA components into a new basis that more accurately reflects the reality of the sample, we employ ICA unmixing of the spatial PCA loadings.

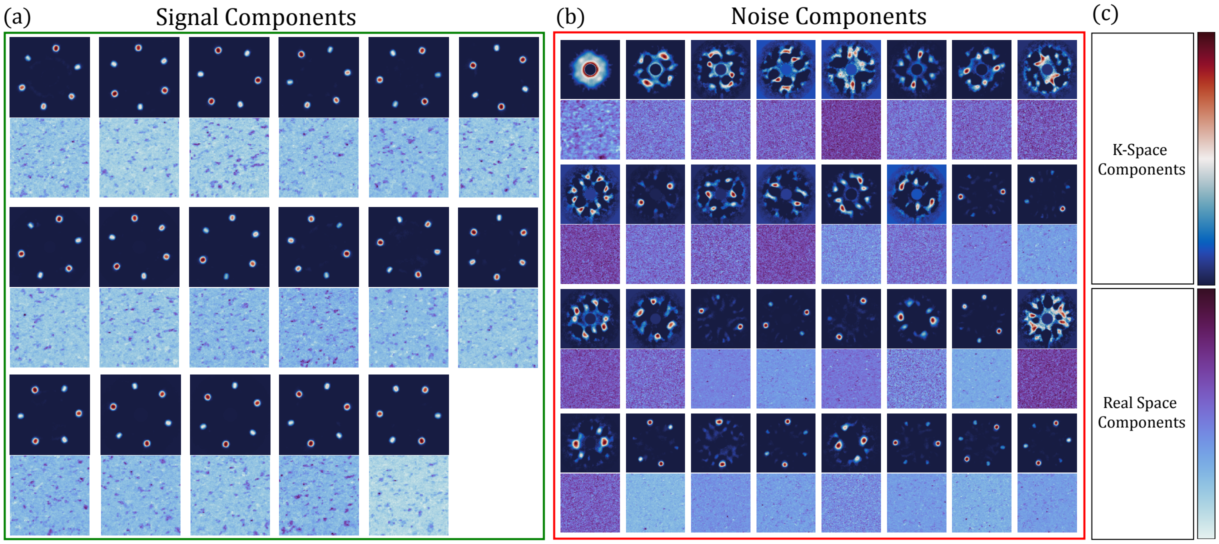

Figure 7.12: ICA unmixing of PCA components. The k-space components (top sub-panels) and real-space components (bottom sub-panels) are sorted into two categories of noise or signal. The signal components in panel (a) appear as three-fold symmetric diffraction patterns in k-space and a collection of small crystalline grains in real-space. The color scales for the k-space and real-space components are shown in (c).

We use intuition gained from the PCA Scree plot to choose the number of components for the ICA input and output. Figure 7.12 shows the results of ICA unmixing using 498 PCA inputs and an output ICA dimension of 49. The first and eighth PCA components are both azimuthally symmetric and are removed from the analysis to increase contrast in the relevant final ICA outputs, described below.

The ICA components display several major attributes. Most striking is the presence of distinct crystalline grains with three-fold rotationally symmetric diffraction patterns, shown in figure 7.12(a) (k-space components, top subpanels). The spatial distribution of each unique grain type is shown in the associated real space component (bottom subpanels).

The first noise component in figure 7.12(b), shows the mean response of the sample under the electron beam. The majority of the noise components appear as spatially homogeneous, illustrated by most of the bottom subpanels of figure 7.12(b), with no apparent physical meaning other than instrumentation noise. Finally, we find rare components in figure 7.12(b) that are not spatially homogenous and have hexagonal diffraction patterns with approximate two-fold rotational symmetry. We attribute these components to describing differences in tilt parallel to the beam.

The model that has emerged from MVA is that the sample is largely composed of multiple grains, each with three-fold rotational symmetry consistent with the 1H phase. Importantly, this three-fold symmetry is not readily apparent from the raw data and has only emerged

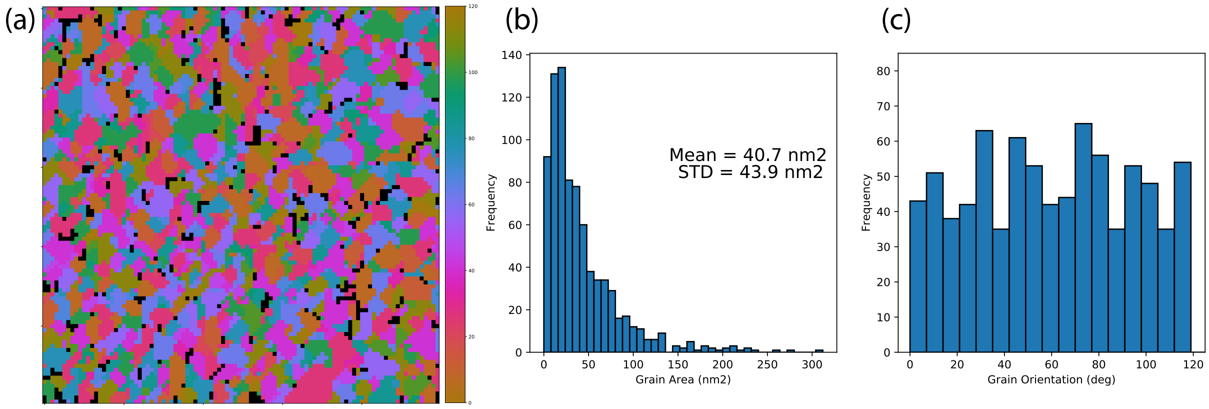

Figure 7.13: Results of MVA grain size/orientation analysis for polycrystalline WS2. The image in (a) shows the spatial distribution of distinct crystalline grains, with the color scale indicating the crystallographic orientation. The black regions are voids where no crystallographic component has appreciable value. The histogram in (b) shows the distribution of grain areas. The distribution peaks at 10 nm^2, and drops to near zero at 150 nm^2. The grain orientation angle distribution is shown in (c). The orientation is defined by the angle of the most intense peak of the k-space component for each component modulo 120 degrees (due to the 3-fold symmetry of the underlying 1H lattice). The distribution is approximately flat between 0 and 120 degrees indicating no preferred grain orientation.

upon MVA processing.

To extract the details of the grain size and rotational orientation across the specimen, we employ image featurization (using Hu moments, section 2.11) and a clustering algorithm (affinity propagation, section 2.12) to automatically sort the components into groups that have similar spatial features and spectral symmetry [157, 27, 29]. This analysis is applied to the IC diffraction patterns, and the same grouping is then applied to the corresponding IC spatial images. We use standard thresholding and particle analysis methods (section 2.13) to generate histograms of the grain sizes and orientations (figure 7.13)(b-c) and a rotational orientation grain map (figure 7.13)(a). From the area distribution we see that the CVD synthesis method used to produce the WS$_2$ films favors small grains ($\sim$10 nm^2), but larger ones are also present up to approximately 100 nm^2. We also find from the diffraction patterns that there is no preferred orientation for the crystalline grains.

In order to assess the efficacy of our MVA methodology, we compare the results using MVA to similar results obtained using traditional methods. Figure 7.14 shows both results side by side. The range of angles for grain map using MVA has been reduced to 60 degrees for a fair comparison. We see that although the agreement is not perfect, the two maps have a high level of similarity, confirming that our MVA methodology is a useful tool for quickly assessing the approximate distribution of sample parameters in a high dimensional data set.

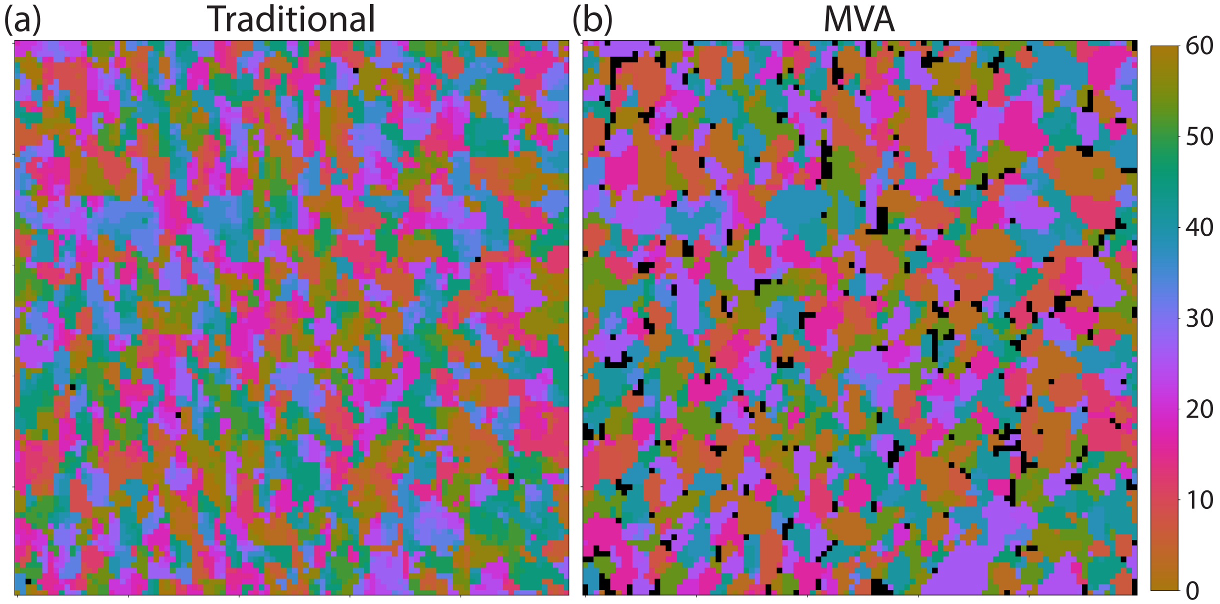

Figure 7.14: Grain size/orientation map from polycrystalline WS_2. Panel(a) shows the results using a traditional analysis and panel (b) shows the results using MVA methodology.

Chapter 8

Optical and Electronic Properties of Gallium Selenide Sulfide Alloys

"California's a wonderful place to live - if you happen to be an orange."

— Fred Allen

This chapter is adapted from a paper published in *Physical Review B*, titled "Tunable Electronic Structure in Gallium Chalcogenide van der Waals Compounds", based on work done in collaboration with the MAESTRO group at Advanced Light Source at Lawrence Berkeley National Lab [38].

8.1 Chapter Abstract

Transition metal monochalcogenides comprise a class of two-dimensional materials with electronic band gaps that are highly sensitive to material thickness and chemical composition. Here, we explore the tunability of the electronic excitation spectrum in GaSe using angle-resolved photoemission spectroscopy. The electronic structure of the material is modified by *in-situ* potassium deposition as well as by forming GaS_xSe_{1-x} alloy compounds. We find that potassium-dosed samples exhibit a substantial change of the dispersion around the valence band maximum (VBM). The observed band dispersion resembles that of a single tetralayer and is consistent with a transition from the direct gap character of the bulk to the indirect gap character expected for monolayer GaSe. Upon alloying with sulfur, we observe a phase transition from AB to AA' stacking. Alloying also results in a rigid energy shift of the VBM towards higher binding energies which correlates with a blue shift in the luminescence. The increase of the band gap upon sulfur alloying does not appear to change the dispersion or character of the VBM appreciably, implying that it is possible to engineer the gap of these materials while maintaining their salient electronic properties.

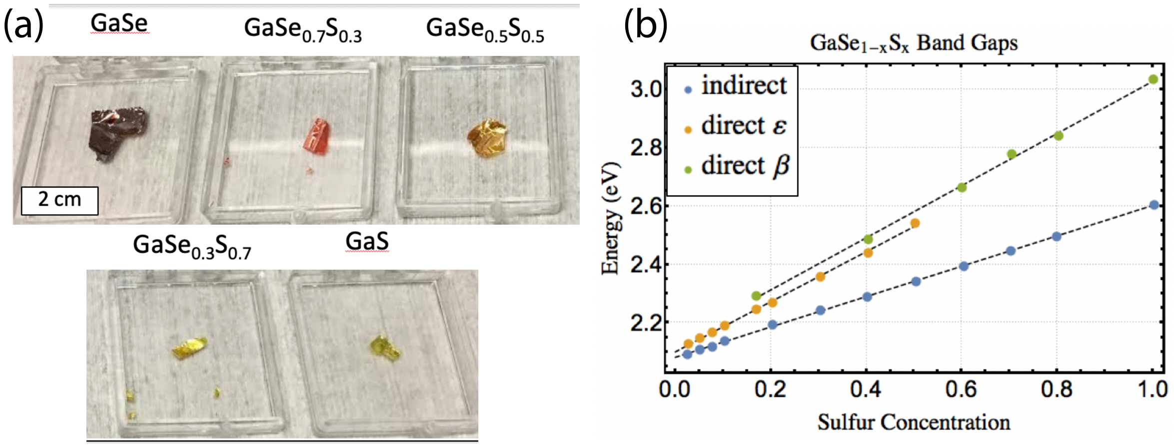

Figure 8.1: Picture of bulk crystals of GaS_xSe_{1-x} alloys across the compositional range ($0 \leq x \leq 1$). The optical properties of these compounds vary smoothly as the concentration of sulfur is varied, as evidenced by the color of the crystals (a) and change in band gap (b). The crystals have two distinct stacking polytypes, ε and β.

8.2 Introduction

The ability to isolate monolayers and study their physical properties has led to a resurgence of interest in layered van der Waals (VDW) materials as two-dimensional systems. Transition-metal chalcogenides belong to this class of materials and demonstrate unique thermoelectric, photonic and electronic properties [158]. The composition, phase, and crystal structure of these materials can be tuned to display a wide range of electronic phases including metallic [159, 160], semiconducting [117, 161, 162], superconducting [163, 164, 165] and charge-density wave [166, 167, 165], inspiring utilization in a wide range of applications including electronic devices, sensors, and quantum devices [168].

Transition metal monochalcogenides comprise a class of two-dimensional materials with electronic band gaps that are highly sensitive to material thickness and chemical composition. In their bulk form, monochalcogenides of Ga and In, such as GaSe, InSe, and GaS are van der Waals compounds. Gallium chalcogenides (GCs) are direct bandgap semiconductors that can be mechanically exfoliated from a bulk parent crystal. Their properties are highly sensitive to material thickness, chemical composition, and crystalline structure [169, 170, 171]. Bulk GaSe and GaS have direct band gaps of 2.10 eV and 3.05 eV, respectively, and transition to indirect gaps when the number of layers is reduced [172, 173]. Monolayer field effect devices maintain mobilities on the order of of 0.1 $cm^2V^{-1}s^{-1}$, on/off ratios of 10^4 - 10^5 as well as quantum efficiencies that exceed those of graphene by several orders of magnitude when implemented in a device architecture [174, 175, 176].

Alloys with mixed chalcogen content, GaS_xSe_{1-x}, allow for control of the bandgap, allowing engineering of the optical absorption and photoluminescence (PL) [177, 178]. Interlayer coupling, defects, doping, and interaction with an underlying substrate may further modify the electronic structure of the GCs, as observed in exfoliated flakes of GaSe and GaTe on SiO2 and graphene [179, 180, 181] and epitaxially grown GaSe flakes on graphene [173, 182, 183].

Here, we illustrate how the crystalline and electronic properties of GC materials are affected by changes in chemical composition, doping, and reduced dimensionality using high resolution scanning transmission electron microscopy (HRSTEM), angle-resolved photoemission spectroscopy (ARPES), and PL.

HRSTEM reveals that GaSe tetralayers stack in the AB sequence (ε phase) while sulfur alloys and GaS stack almost exclusively in the AA$'$ sequence (β phase). The complete $E\left(k_x, k_y, k_z\right)$ electronic structure of AB-stacked GaSe is determined using ARPES, allowing us to directly extract the band dispersion along high symmetry directions and determine valence band (VB) extrema and effective masses. We illustrate how the full energy-momentum-resolved quasiparticle band structure of the GCs is modulated when the chemical composition and/or interaction between layers is changed.

We explore the influence of potassium deposition on the band structure, finding it only causes a slight energy shift of the VBs and does not lead to degenerate doping which would enable ARPES visualization of the conduction band. However, potassium dosing does lead to a significant change of the dispersion around the top of the VB, implying a strong modification at the surface GaSe tetralayer compared to the bulk. The observed band dispersion resembles that of a single tetralayer and is consistent with a transition from the direct gap character of the bulk, to the indirect gap character expected for monolayer GaSe.

Finally, we explore the effect of sulfur alloying on the band structure. Upon alloying with sulfur, we observe a phase transition from AB to AA$'$ stacking. We find that increasing sulfur content produces a rigid VB shift and results in a corresponding blue shift in the PL, suggesting that alloying is a viable method for tuning GC optical properties. The increase of the band gap upon sulfur alloying does not appear to change the dispersion or character of the VBM appreciably, implying that it is possible to engineer the gap of these materials while maintaining their salient electronic properties.

8.3 Experimental Methods

We study pure GaSe and GaS as well as three alloy compositions spanning the entire compositional range of $\mathrm{GaS}_x\mathrm{Se}_{1-x}$ alloys, pictured in figure 8.1(a). Crystals are grown using the modified Bridgman-Stockbarger method [184]. Briefly, stoichiometric amounts of Ga, S, and Se powder are weighed and mixed in sealed quartz ampoules to achieve the desired alloying ratio. The Ampoules are then heated in a zone furnace at 970 °C for two weeks to grow single crystals 2-8 mm in diameter.

The HRSTEM samples are prepared by a two-step process. First, the crystals are cleaved using blue wafer dicing tape and transferred to Si substrates coated with 100 nm thick SiO_2. Next, a Cu TEM grid with carbon film is adhered to flakes on the $\mathrm{Si/SiO}_2$ wafer using a drop of isopropanol. Once the drop has dried, the SiO_2 is etched away using 1M NaOH. Lastly the grid is washed in deionized water and dried prior to imaging. HRSTEM is carried out using a double C_s corrected FEI Titan 80-300 operating at an accelerating voltage of 80 kV at the Molecular Foundry.

For ARPES measurements, large crystals of GCs are glued to a Cu sample holder using epoxy and cleaved *in-situ* in the ultra-high vacuum (UHV) chamber with a base pressure better than 5×10^{-11} mbar. The samples are cooled to 85 K prior to cleaving and kept at this temperature during ARPES measurements. The cleaved single-crystal domain sizes are on the order of 100 μm as defined by spatially scanning the sample with the synchrotron beam. The ARPES data are collected at the Microscopic and Electronic Structure Observatory (MAESTRO) at the Advanced Light Source (ALS) using the microARPES end-station equipped with a hemispherical Scienta R4000 analyzer. The beamline slit settings are adjusted so that the size of the beam is on the order of 20 μm. VB and Ga 3d core level spectra are obtained primarily using a photon energy of 94 eV. S 2p and Se 3p core level data are collected using a photon energy of 300 eV. Photon energy scans of GaSe are acquired for photon energies between 21 eV and 140 eV. In order to relate the photoelectron kinetic energy, E_{kin}, to the out-of-plane momentum, k_z, we use the free-electron final state assumption where $k_z^2 = (2m/\hbar^2)\,(E_{kin} + V_0)$, where V_0 is the inner potential [185]. We find that $V_0 = 10.2$ eV provides the best description of the data, given the out-of-plane lattice constant c = 15.96 Å and the Brillouin zone (BZ) periodicity of $2\pi/c$ for the measured polytypes of GaSe.

The Fermi energy is determined on the clean Cu sample holder in contact with the crystals for all photon energies. The presence of surface photovoltage-induced energy shifts in the samples is checked by varying the photon flux. No such changes were observed, except on GaS, which excluded ARPES measurements on this material.

Potassium dosing experiments on GaSe are carried out *in-situ* using SAES getters mounted in the analysis chamber while the sample is kept at 85 K. Each dose takes 50 seconds, and between doses, an (E, k) spectrum of the VB and an energy spectrum over the Ga 3d/K 3p binding energy region are taken. The collection of these spectra takes 70 seconds and 12 doses were applied for the results presented here, amounting to a total time of 24 minutes for collecting the dataset.

Judging from the change in photoemission intensity from the VB upon further dosing, we estimate a coverage rate of a complete monolayer after 12 doses. We observe that prolonged exposure to the synchrotron beam for the fully K-dosed sample leads to broadening and significant deterioration of the quality of the spectral features, preventing detailed photon energy or angle scans for the K-dosed samples.

The total energy and momentum resolution in the ARPES data are better than 20 meV and 0.01 Å^{-1}, respectively.

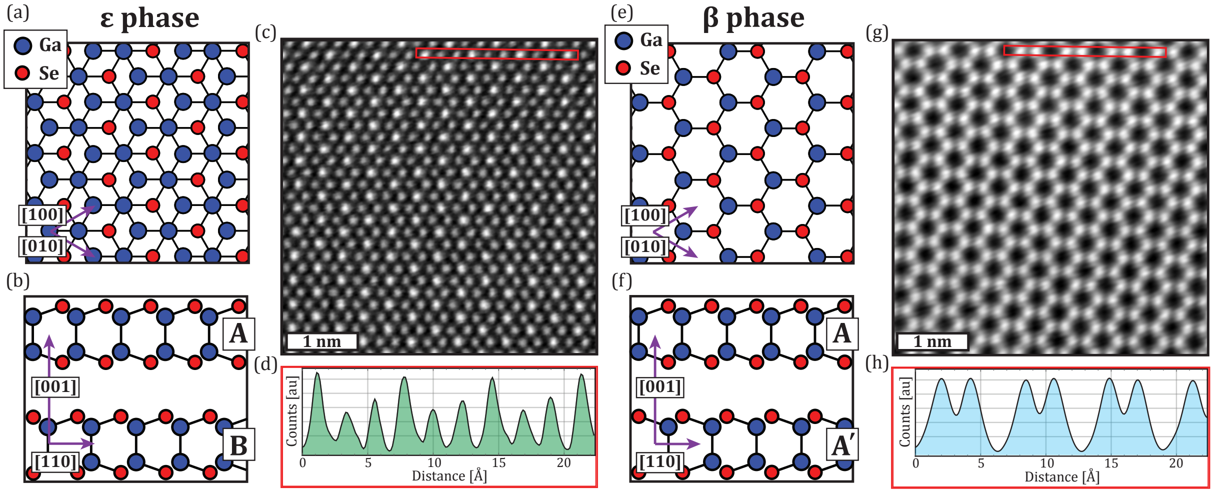

Figure 8.2: Real space structure and HRSTEM images of the two most common GaS_xSe_{1-x} polytypes. Panels (a) and (b) show the crystal structure of the ε phase in the planes defined by the axes in the labels. The corresponding HRSTEM image in (c) shows a trigonal lattice, resulting from the projection of Bernal (AB) stacked honeycomb layers. The intensity cut in (d) was obtained from the red rectangle in (c) and shows bright atomic columns with approximately twice the intensity of dim atomic columns. Analogous images in (e)-(f) show the geometry of the β phase. The HRSTEM image in (g) shows a honeycomb mesh, with no intensity in the interstitial columns between hexagonal cells.

8.4 Results and Discussion

HRSTEM Measurements of Gallium Chalcogenides

The GaS_xSe_{1-x} system forms a continuous set of alloys for the entire compositional range ($0 \leq x \leq 1$) of the stoichiometry [186, 187, 188]. Like other layered VdW materials, the intralayer bonding is strong and mostly covalent while the interlayer bonding is weak and of VdW character. The unit cell consists of two tetrahedral pyramids stacked tip to tip with chalcogen atoms at the base and a Ga atom at the apex, forming a four-atom-thick tetralayer.

The layer stacking exhibits several different polytypes, depending on composition and growth conditions. In the ε phase (Fig. 8.2(a-b)), successive tetralayers are stacked in the sequence AB, resulting in Ga atoms from the A layer being vertically aligned with chalcogen atoms in the the B layer, and chalcogen atoms in the A layer being vertically aligned with the interstitial voids in the centers of the hexagons from the B layer, similar to Bernal stacking in graphite. The inversion symmetric β phase (Fig. 8.2(e-f)) is obtained by stacking successive tetralayers in the sequence AA′, resulting in Ga(chalcogen) atoms from the A layer eclipsing chalcogen(Ga) atoms from the A′ layer. The system can also form the rhombohedral γ phase

(ABC stacking), but this stacking sequence is not observed experimentally in our samples.

Previous studies have explored the relationship between sulfur content and stacking phase [186, 187, 188]. $\mathrm{GaS}_x\mathrm{Se}_{1-x}$ alloys with low sulfur content (x < 0.15) stack in the ε phase while alloys with higher sulfur content (x > 0.35) display the β stacking phase. Our experimental results (described below) also show this trend. We find that the ε phase occurs for x ≤ 0.3 and the β phase for x > 0.3, The β and ε phases are thought to co-exist for intermediate sulfur content ($0.15 <$ x < 0.35), phase segregated throughout the crystal, but our samples do not show experimental evidence for this theory.

Contrast in HRSTEM indicates differences in atomic number, density, and thickness throughout a specimen. Due to the specific stacking sequences exhibited by the polytypes of $\mathrm{GaS}_x\mathrm{Se}_{1-x}$ alloys and the contrast mechanisms of STEM imaging, our imaging experiments (Fig. 8.2(c) and 8.2(g)) unambiguously reveal the stacking phases of these materials.

Figure 8.2(c) shows a typical HRSTEM image for an alloy with high sulfur content (x ~ 0.75), appearing as a trigonal lattice with alternating bright and dim atomic columns. Figure 8.2(d) shows a line plot of the intensity extracted from the region outlined by the red rectangle in Fig. 8.2(c). The heights of the peaks in the line trace indicate that there are approximately twice as many atoms in bright columns compared to the dim columns, consistent with the stacking geometry of the ε phase, shown in Fig. 8.2(b). Figure 8.2(g) shows an analogous image for pure GaSe which appears as a honeycomb mesh of atomic columns with no appreciable intensity in the interstitial voids between hexagons. The line profile (Fig. 8.2(h)) shows that the atomic columns have uniform intensity, consistent with AA$'$ stacking exhibited by the β phase.

ARPES Electronic Structure Measurements of GaSe

An overview of the electronic band structure of pristine GaSe is presented in Fig. 8.3. The data are acquired at a photon energy of 94 eV, which probes around the Γ point, as described by the BZ sketches in Fig. 8.3(a). Figures 8.3(b)-(c) show cuts along the $\Gamma - K - M$ and $\Gamma - M - \Gamma$ high symmetry directions as signified by the dashed lines in Fig. 8.3(a). The evolution of the dispersion with binding energy is presented via the constant binding energy cuts in Fig. 8.3(d)-(h), which reveal the trigonal symmetry of the dispersion as well as strong intensity variations between the bands in the BZs. The valence band maximum (VBM) is situated at Γ and is characterized by a parabolic-shaped lobe. The location of the VBM at Γ is consistent with theoretical predictions that GaSe is a direct-gap semiconductor with the conduction band minimum (CBM) also located at Γ [189]. Additional sub bands dispersing towards M and K appear above binding energies of 1.5 eV. The material remains rather featureless away from Γ before the onset of this higher binding energy range, implying most of the optical properties of GaSe will derive from the central parabolic lobe. The ARPES data discussed here are fully consistent with the electronic structure data presented in Ref. [190].

We investigate the k_z-dispersion in the three dimensional BZ of GaSe shown in Fig. 8.4(a). By measuring the photon energy dependence of the dispersion at normal emission

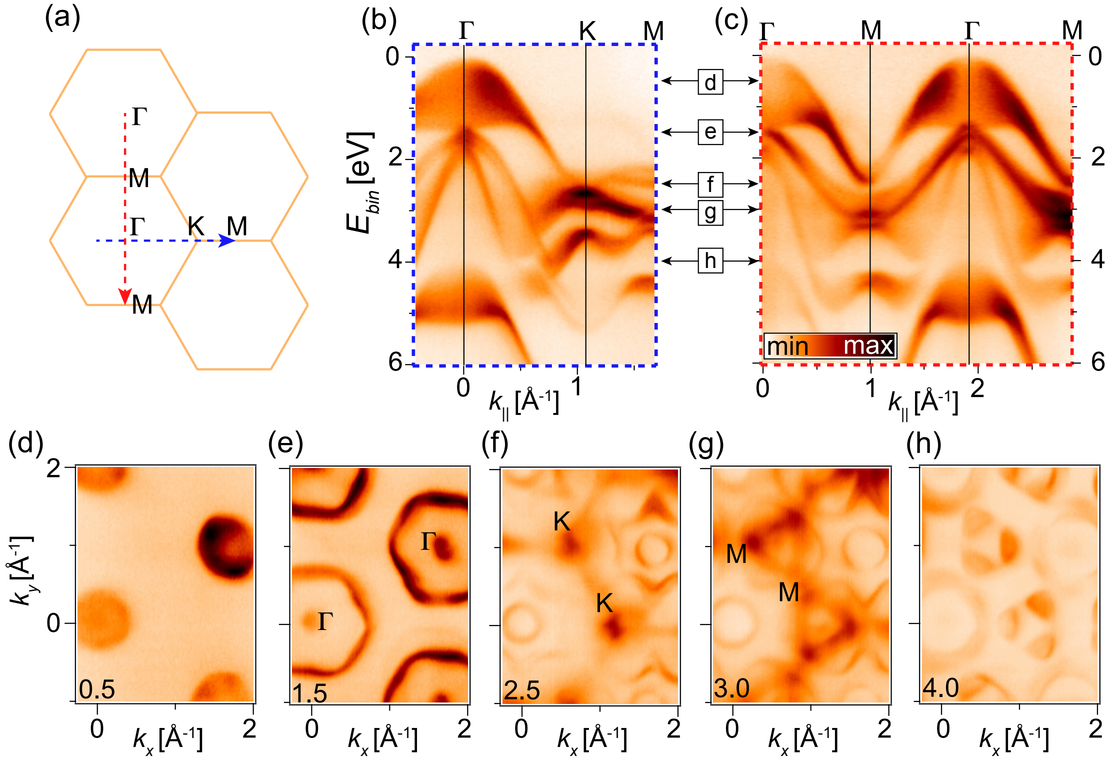

Figure 8.3: ARPES measurements at a photon energy of 94 eV of the electronic structure of pristine GaSe around the Γ point. (a) Sketch of the BZs and their orientation in the experiment with Γ, K and M symmetry points labeled.(b) Measured dispersion in the $\Gamma - K - M$ direction obtained along the blue dashed line shown in (a). (c) Measured dispersion in the $\Gamma - M - \Gamma$ direction obtained along the red dashed line shown in (a). The double headed arrows in (b)-(c) indicate the planes of constant energy from which the cuts in (d)-(h) are taken. The energy of each cut is also listed in bottom of each panel in units of electron volts (eV). High symmetry points Γ, K and M have been labeled in (e), (f) and (g), respectively.

we are able to trace the band structure along the $\Gamma - A$ direction, as seen in Fig. 8.4(b). A strong k_z-dispersion is visible in the center of the parabolic lobe, which is further highlighted via the fits (open circles) and guide line in Fig. 8.4(b), whereas the bands at binding energies higher than 1.5 eV have a much more flat k_z-dispersion. The fitted dispersion reveals an apparent BZ doubling effect; however, this occurs due to a suppression of the photoemission intensity in adjacent BZs [190], similar to observations in photoemission experiments on graphite [191, 192]. The band structure along the $\Gamma - K$ line is shown for two neighboring BZs in the k_z direction in Fig. 8.4(c-d). The main intensity moves from the bottom corners of the parabolic lobe in Fig. 8.4(c) to the VBM in Fig. 8.4(d). Similar intensity variations are observed in neighboring in-plane BZs, as sketched in Fig. 8.4(e). The ($k_{||}$, k_z)-contour at a binding energy of 0.2 eV shown in Fig. 8.4(f) shows a cut around the VBM for the

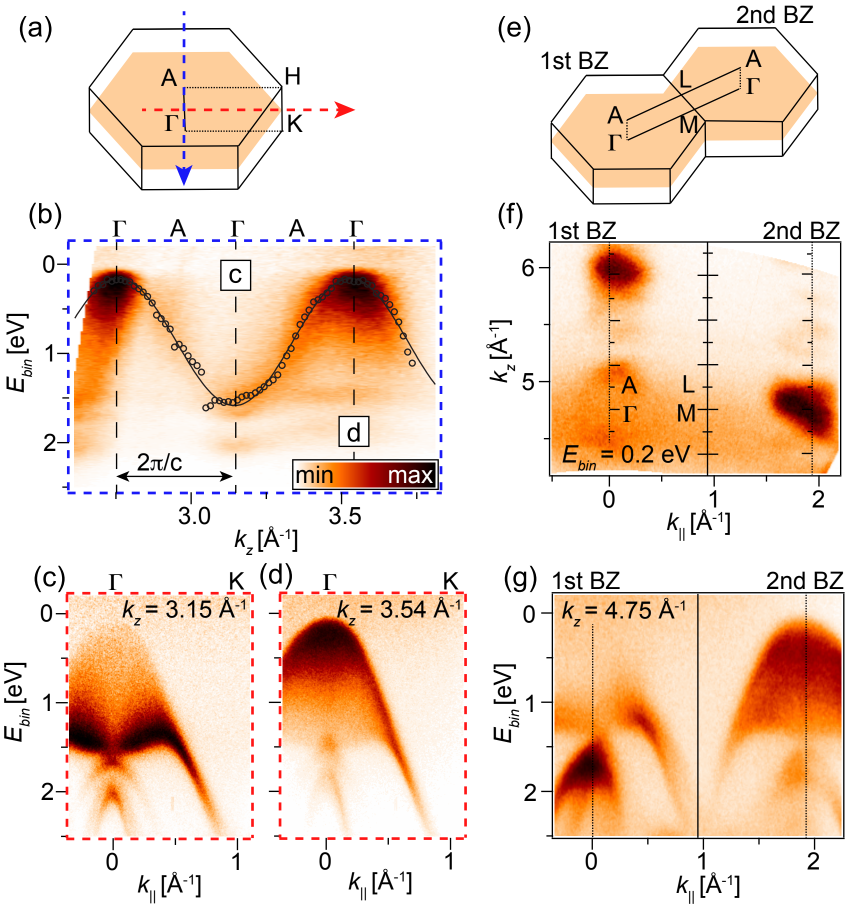

Figure 8.4: ARPES measurements of the k_z-dispersion of GaSe. (a) Sketch of bulk BZ highlighting the $\Gamma - A - H - K$ plane. (b) Dispersion along the $\Gamma - A$ direction, as marked by the blue dashed line in (a). Fits of the position of the VBM intensity are shown via open circles. The solid curve following the fitted dispersion is a guide for the eye. The BZ size of $2\pi/c$ in the z-direction is marked by a double-headed arrow and two vertical dashed lines. (c)-(d) Dispersion extracted at the given k_z values, corresponding to the $\Gamma - K$ direction (red dashed line). (e) Sketch of 1st and 2nd BZs with an outline of the $\Gamma - A - L - M$ plane. (f) Constant energy contour of the plane sketched in (e) extracted at a binding energy of 0.2 eV with high symmetry points annotated by tick marks. (g) Dispersion along the $\Gamma - M - \Gamma$ direction obtained at a k_z value of 4.75 Å^{-1}.

$\Gamma - A - L - M$ plane (see Fig. 8.4(e)). The intensity maxima are seen to shift between the 1st and 2nd BZs and the absolute intensity levels also vary strongly within the same BZ. A cut along the $\Gamma - M$ line at $k_z = 4.75$ Å^{-1} in Fig. 8.4(g) shows the upper VB parabolic lobe in two neighboring zones. In the first BZ, the intensity is concentrated in the bottom corner while in the 2nd BZ the intensity is concentrated around the VBM.

This behavior can be reconciled with the orbital character of the bands, previously studied with detailed calculations [169]. Since the states near the VBM are mainly of Se p_z character, the interlayer interactions will cause intensity modulations reflecting the coupling of the GaSe tetralayers, leading to a dispersion resembling a single tetralayer for the k_z value used for the slice shown in Fig. 8.4(c), while the k_z value for Fig. 8.4(d) shows a dispersion with a more bulk-like character [169]. The subbands just below the VBM exhibit less dramatic behavior due to the $p_{x(y)}$ character of these states which are less sensitive to the adjacent GaSe tetralayers [193, 194].

Potassium Deposition of GaSe

The effect of K dosing of bulk GaSe is explored in Fig. 8.5. Alkali metal deposition offers a possibility to chemically donate electrons near the surface of GaSe and thereby dope the material. The ARPES measurements along the $\Gamma - K - M$ direction in Fig. 8.5(a-b) before and after complete K dosing show that a significant band structure change occurs, rather than strong electron doping. A maximum energy shift of 0.1 eV of the VB towards higher binding energies is observed, which may originate from surface band bending due to the added charge or a slight doping of the material. After further dosing, we observe that the spectral weight shifts from the top (see Fig. 8.5(a)) to the bottom (see Fig. 8.5(b)) of the VB lobe. In Fig. 8.5(c), the VBM dispersion (open circles), extracted via fits to energy distribution curves (EDCs), has been fitted with 2nd and 4th order polynomial functions in the clean and K doped cases, respectively. In the pristine GaSe, a global VBM is observed at Γ and at a binding energy of (0.09 ± 0.03) eV. The effective mass around the top of the parabola is $m^* = (1.1 \pm 0.2)m_0$, where m_0 is the free electron mass. In K dosed GaSe, the VBM splits off into two maxima located at ± 0.3 Å^{-1} with a binding energy of (1.30 ± 0.04) eV and an effective mass of $m^* = (1.7 \pm 0.2)m_0$.

The EDCs extracted at normal emission in Fig. 8.5(d) trace the peak positions at each K dosing step. Voigt line shapes have been fitted to each of the peaks, which have been plotted together with the photoemission intensity at normal emission at each K dose in Fig. 8.5(e), revealing a gradual shift of the ARPES intensity from the pristine bulk dispersion seen in Fig. 8.5(a) to the modified dispersion shown in Fig. 8.5(b). The modified dispersion strongly resembles the "bow-shape" or"inverted sombrero" dispersion of single-layer GaSe, where the inversion of the VB is characterized by the energy difference between the VBM and the local energy minimum at Γ [169, 178, 195, 196, 197]. Here, we find that the band inversion is (48 ± 12) meV, which compares well with a value of 80 meV obtained from recent DFT calculations [196]. The value is substantially smaller than 120 meV found for single-layer GaSe grown on graphene on silicon carbide [197] and than the value of (150 +/- 10) meV that we determine for the similar dispersion at $k_z = 3.15$ Å^{-1} in Fig. 8.4(c). We expect that interlayer interactions between the Se p_z orbitals play a significant role for these dispersion changes around the VBM [169] and that the gradual change observed in Fig. 8.5(e) signals a modification of the topmost GaSe layer, leading to a weaker coupling to the underlying bulk. This may be facilitated by K intercalation in the van der Waals gap

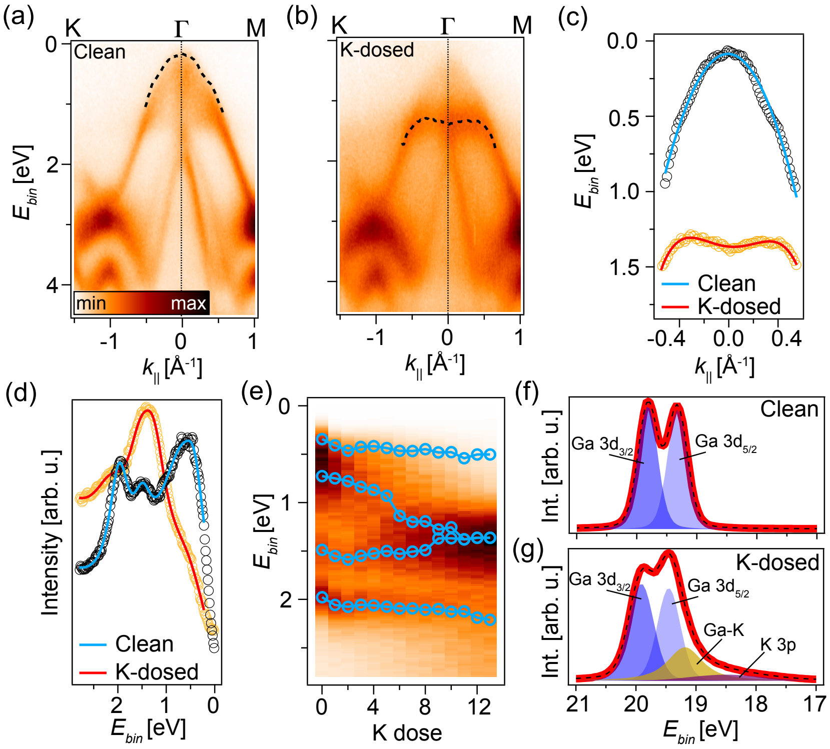

Figure 8.5: Effect of K dosing on the GaSe electronic structure. (a)-(b) ARPES Measurements of the dispersion in the $\Gamma - K - M$ direction (a) before and (b) after K dosing. The dashed curves present the fitted location of the VBM peak intensity. (c) Location of the VBM peak intensity (open circles) fitted with a 2nd order and a 4th order polynomial for the clean and K dosed samples, respectively. (d) EDCs (open circles) and results of Voigt function fits (curves) in the clean and K dosed cases. The EDCs were extracted at Γ along the lines shown in (a)-(b). The position of the top-most peak is plotted via dashed lines in (a)-(b) and open circles in (c). (e) Evolution of the photoemission intensity at Γ as a function of K dosing steps. The open circles and guidelines mark the fitted peak positions obtained by performing the EDC analysis shown in (d) in each K dosing step. (f)-(g) Ga 3d core level measurements (f) before and (g) after K dosing. The data (thick red curves) have been fitted (dashed curves) with Doniach-Sunjic line shapes (filled peaks) for each of the observed components.

between the layers, as observed in metallic [198], and semiconducting [199] transition metal dichalcogenides, or by a chemical interaction on the surface of the crystal, which significantly changes the coupling between individual layers as seen in graphene multilayers [200, 201]. In these situations one may also expect a change of the interlayer separation of tetralayers as well as a shift of inner potential, which also contribute to the spectral changes we observe. The possibility of chemical changes near the surface is further supported by the observation

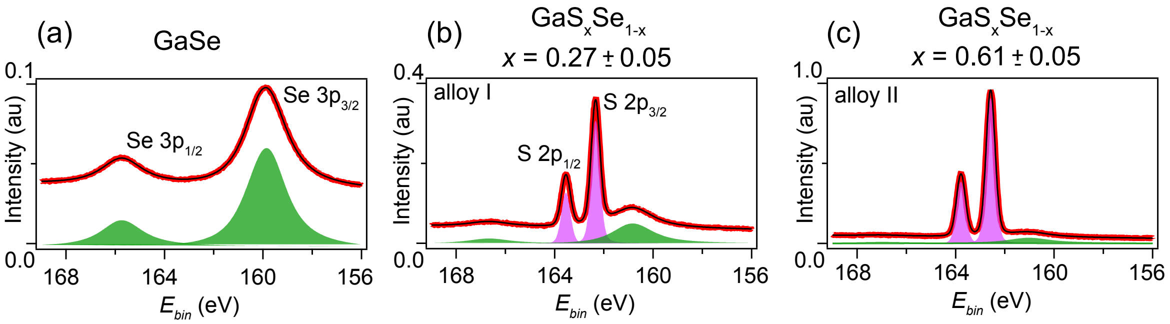

Figure 8.6: Composition of $\mathrm{GaS}_x\mathrm{Se}_{1-x}$ alloys from core level data. (a)-(c) Core level measurements (red thick curves) in the Se 3p and S 2p binding energy region for (a) GaSe and (b)-(c) $\mathrm{GaS}_x\mathrm{Se}_{1-x}$ alloys. Fit results (black curves) to Doniach-Sunjic line shapes (filled peaks) are provided in each panel. The composition x of the alloys determined via the fitted peak components is stated in (b)-(c). Note the intensity scale varies between the panels.

of an additional core level component in the binding energy range between the Ga 3d and K 3p core levels for the K-dosed sample, which is demonstrated by the comparison between the clean GaSe core level spectrum in Fig. 8.5(f) and the spectrum for the fully K-dosed sample in Fig. 8.5(g).

ARPES and PL Measurements of $\mathrm{GaS}_x\mathrm{Se}_{1-x}$

$\mathrm{GaS}_x\mathrm{Se}_{1-x}$ alloys offer a promising route to tune the optical gap and luminescent properties of III-VI semiconductors. However, it is unknown how robust the electronic structure remains between different alloys. Here we compare pristine GaSe with two different $\mathrm{GaS}_x\mathrm{Se}_{1-x}$ alloys (alloys I and II). The stoichiometry x is checked via core level measurements of the Se 3p and S 2p binding energy regions, shown in Fig. 8.6. By comparing the spectral weight of the Se 3p core levels, we are able to estimate that the composition of alloy I is $\mathrm{x} = 0.27 \pm 0.05$ and the composition of alloy II is $\mathrm{x} = 0.61 \pm 0.05$. These values are consistent when we perform the same analysis on the Se 3d core levels (not shown). The core level data is in agreement with the stoichiometry of precursor added to the growth ampoule.

Figure 8.7(a)-(c) present ARPES measurements of the VBs for the three systems. The overall band dispersion is found to be very similar with a constant effective mass of $m^* = (1.1 \pm 0.2)m_0$. The binding energy position of the VBM changes significantly between the three systems, indicating a change of the electronic band gap. It is also possible that Fermi level pinning plays a strong role for the band positions, as the defect concentration is likely different in the alloys. PL measurements, shown in Fig. 8.7(d), reveal a change of the optical gap. The PL peak positions plotted in Fig. 8.7(e) show that the optical gap increases as more S is added in the alloy. The same trend is seen for the VBM binding energy position in Fig. 8.7(f), which fits with a simultaneous increase of the quasiparticle band gap. The trend

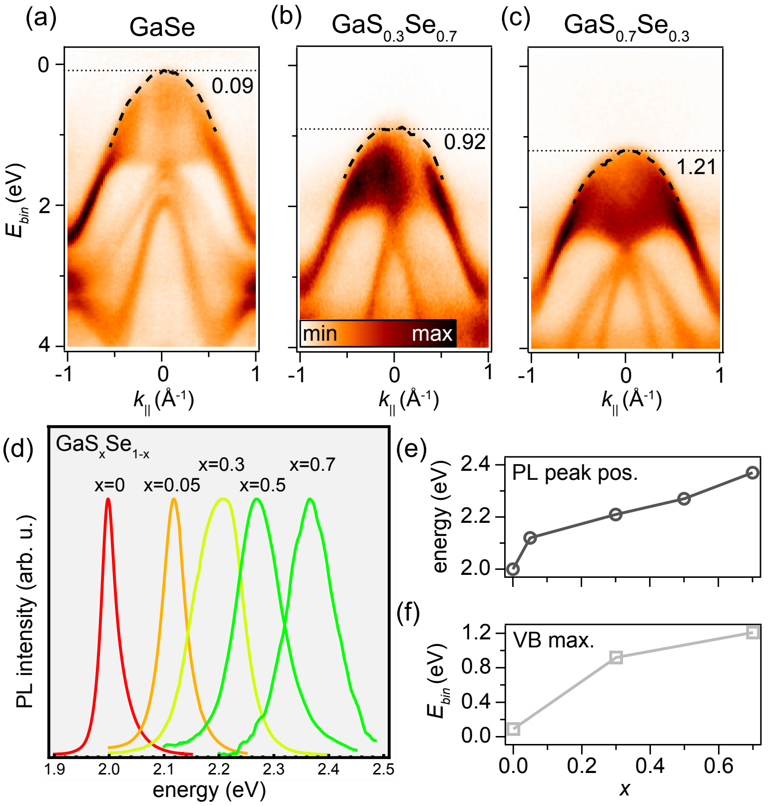

Figure 8.7: VBM and PL peaks positions for $\mathrm{GaS}_x\mathrm{Se}_{1-x}$ alloys. (a)-(c) ARPES measurements of the upper VB region for (a) GaSe, (b) $\mathrm{GaS}_{0.27}\mathrm{Se}_{0.73}$ and (c) $\mathrm{GaS}_{0.61}\mathrm{Se}_{0.39}$. The dotted line presents the fitted position of the VBM and the dashed curves exhibit the fitted dispersion around the VBM in each case. The corresponding VBM binding energy positions are given in units of eV with an error bar of ±0.03 eV. (d) PL intensity for the same samples as in (a)-(c) and Fig. 8.6. (e)-(f) Positions of the (e) PL peaks and (f) VBM as a function of composition.

determined here is fully consistent with optical absorption measurements of $\mathrm{GaS}_x\mathrm{Se}_{1-x}$ [178]. Note that ARPES measurements of pure GaS were attempted but the sample was found to charge too severely, which is likely due to the larger band gap of the material compared to the other $\mathrm{GaS}_x\mathrm{Se}_{1-x}$ compounds investigated here.

The ε and β stacking phases observed in HRSTEM are not expected to give rise to striking differences in the electronic structure [193, 194, 195]. However, detailed inspection of the measurements in Fig. 8.7(a)-(c) does show some variation in the intensity and structure of the dispersive bands in the higher binding energy region above the central VB lobe. While different stacking phases may affect the photoemission intensity, the change in chemical environment caused by the mixed chalcogen content directly influences the in-plane $\mathrm{p}_{x(y)}$ orbitals that the higher binding energy bands are composed of, thereby leading to the possibility of a modified dispersion.

8.5 Chapter Conclusion

We have measured the bulk electronic structure of GaSe using ARPES and thereby identified the bulk band dispersion, the structure of the VBM, and the complex photoemission intensity variations associated with the tetralayer unit cell. Potassium deposition of GaSe leads to a dramatic change of the VBM dispersion from a parabolic shape characteristic for the bulk to an inverted bow-like shape that is usually associated with single-layer samples. Our data are consistent with an increased band gap and a transition from a direct to an indirect band gap semiconductor, which is caused by a strong modification of the top-most GaSe tetralayer due to the interaction with the deposited K atoms. We have investigated the effect of sulfur alloying on the crystalline and electronic structure and used HRSTEM to observe a transition from the ε phase to the β phase for sulfur content above $\sim$30 percent. We have also shown that alloying causes a rigid shift of the VBM binding energy position without a significant change in the actual band dispersion around the VBM. This rigid shift is consistent with an increase in the optical band gap measured by PL.

Bibliography

[1] Eugene Hecht. *Optics*. Addison-Wesley, 2002.

[2] C. M. Sparrow. “On Spectroscopic Resolving Power”. In: *The Astrophysical Journal* 44 (1916), p. 76.

[3] Ludwig Reimer. *Scanning Electron Microscopy: Physics of Image Formation and Microanalysis*. Springer Science & Business Media, 1998.

[4] R. F. Egerton. “Scattering delocalization and radiation damage in STEM-EELS”. In: *Ultramicroscopy* 180 (2017), pp. 115–124.

[5] DB Williams and BC Carter. *Transmission Electron Microscopy: A Textbook for Material Science*. Springer New York, 2016.

[6] Brent Fultz and James Howe. *Transmission Electron Microscopy and Diffractometry of Materials*. Springer Berlin Heidelberg, 2013.

[7] Ludwig Reimer and Helmut Kohl. *Transmission Electron Microscopy: Physics of Image Formation*. Springer Science & Business Media, 2008.

[8] Jannik C. Meyer et al. “Hydrocarbon lithography on graphene membranes”. In: *Appl. Phys. Lett.* 92.12 (2008), p. 123110.

[9] Andres Castellanos-Gomez et al. “Deterministic transfer of two-dimensional materials by all-dry viscoelastic stamping”. In: *2D Mater.* 1.1 (2014), p. 011002.

[10] Xuesong Li et al. “Large-Area Synthesis of High-Quality and Uniform Graphene Films on Copper Foils”. In: *Science* 324.5932 (2009), pp. 1312–1314.

[11] Junhao Lin et al. “Gentle transfer method for water- and acid/alkali-sensitive 2D materials for (S)TEM study”. In: *APL Materials* 4.11 (2016), p. 116108.

[12] Charles Kittel. *Introduction to Solid State Physics*. Wiley, 2004.

[13] Neil W. Ashcroft and N. David Mermin. *Solid State Physics*. Cengage Learning, 2011.

[14] M. Eckert. “Max von Laue and the discovery of X-ray diffraction in 1912”. In: *Annalen der Physik* 524.5 (2012), A83–A85.

[15] David Jeffery Griffiths. *Introduction to Quantum Mechanics*. Pearson Prentice Hall, 2005.

[16] J. J. Sakurai and Jim Napolitano. *Modern Quantum Mechanics.* Cambridge University Press, 2017.

[17] Brian Shevitski et al. “Dark-field transmission electron microscopy and the Debye-Waller factor of graphene”. In: *Phys. Rev. B* 87.4 (2013), p. 045417.

[18] J.M. Cowley. *International Tables for Crystallography, Vol. C, Section 4.3.1, A.J.C. Wilson, Ed.* Kluwer Academic, Dordrecht, 1992.

[19] Kwanpyo Kim et al. “Grain Boundary Mapping in Polycrystalline Graphene”. In: *ACS Nano* 5.3 (2011), pp. 2142–2146.

[20] Pinshane Y. Huang et al. “Grains and grain boundaries in single-layer graphene atomic patchwork quilts”. In: *Nature* 469.7330 (2011), pp. 389–392.

[21] Ondrej L. Krivanek et al. “Vibrational spectroscopy in the electron microscope”. In: *Nature* 514.7521 (2014), pp. 209–212.

[22] John C. Russ. *The Image Processing Handbook.* CRC Press, 2006.

[23] Pentti Paatero and Unto Tapper. “Positive matrix factorization: A non-negative factor model with optimal utilization of error estimates of data values”. In: *Environmetrics* 5.2 (1994), pp. 111–126.

[24] Daniel D. Lee and H. Sebastian Seung. “Learning the parts of objects by non-negative matrix factorization”. In: *Nature* 401.6755 (1999), pp. 788–791.

[25] Morten Arngren, Mikkel N. Schmidt, and Jan Larsen. “Unmixing of Hyperspectral Images using Bayesian Non-negative Matrix Factorization with Volume Prior”. In: *J Sign Process Syst* 65.3 (2011), pp. 479–496.

[26] Guoxu Zhou, Andrzej Cichocki, and Shengli Xie. “Fast Nonnegative Matrix/Tensor Factorization Based on Low-Rank Approximation”. In: *IEEE Transactions on Signal Processing* 60.6 (2012), pp. 2928–2940.

[27] Ming-Kuei Hu. “Visual pattern recognition by moment invariants”. In: *IRE Transactions on Information Theory* 2.8 (1962), pp. 179–187.

[28] Stuart P. Lloyd. “Least squares quantization in pcm”. In: *IEEE Transactions on Information Theory* 28 (1982), pp. 129–137.

[29] Brendan J. Frey and Delbert Dueck. “Clustering by Passing Messages Between Data Points”. In: *Science* 315.5814 (2007), pp. 972–976.

[30] R Kubo, A Kawabata, and S Kobayashi. “Electronic Properties of Small Particles”. In: *Annu. Rev. Mater. Sci.* 14.1 (1984), pp. 49–66.

[31] S. V. Gaponenko. *Optical Properties of Semiconductor Nanocrystals.* Cambridge University Press, 1998.

[32] C. B. Murray, C. R. Kagan, and M. G. Bawendi. “Synthesis and Characterization of Monodisperse Nanocrystals and Close-Packed Nanocrystal Assemblies”. In: *Annual Review of Materials Science* 30.1 (2000), pp. 545–610.

[33] Kim De Nolf et al. “Controlling the Size of Hot Injection Made Nanocrystals by Manipulating the Diffusion Coefficient of the Solute”. In: *J. Am. Chem. Soc.* 137.7 (2015), pp. 2495–2505.

[34] Michela Sainato et al. “Long-Range Order in Nanocrystal Assemblies Determines Charge Transport of Films”. In: *ACS Omega* 2.7 (2017), pp. 3681–3690.

[35] Thang Pham et al. “Torsional instability in the single-chain limit of a transition metal trichalcogenide”. In: *Science* 361.6399 (2018), pp. 263–266.

[36] Scott Meyer et al. “Metal-insulator transition in quasi-one-dimensional ${\mathrm{HfTe}}_{3}$ in the few-chain limit”. In: *Phys. Rev. B* 100.4 (2019), p. 041403.

[37] Brian Shevitski et al. “Blue-Light-Emitting Color Centers in High-Quality Hexagonal Boron Nitride”. In: *Physical Review B* (2019).

[38] Brian Shevitski et al. “Tunable Electronic Structure in Gallium Chalcogenide van der Waals Compounds”. In: *Physical Review B* (2019).

[39] K. S. Novoselov et al. “Two-dimensional atomic crystals”. In: *PNAS* 102.30 (2005), pp. 10451–10453.

[40] A. Nagashima et al. “Electronic dispersion relations of monolayer hexagonal boron nitride formed on the Ni(111) surface”. In: *Phys. Rev. B* 51.7 (1995), pp. 4606–4613.

[41] C. R. Dean et al. “Boron nitride substrates for high-quality graphene electronics”. In: *Nature Nanotechnology* 5.10 (2010), pp. 722–726.

[42] Toan Trong Tran et al. “Quantum emission from hexagonal boron nitride monolayers”. In: *Nature Nanotechnology* 11.1 (2016), pp. 37–41.

[43] L. J. Martínez et al. “Efficient single photon emission from a high-purity hexagonal boron nitride crystal”. In: *Phys. Rev. B* 94.12 (2016), p. 121405.

[44] R. Haubner et al. “Boron Nitrides — Properties, Synthesis and Applications”. In: *High Performance Non-Oxide Ceramics II.* Springer Berlin Heidelberg, 2002.

[45] T. Taniguchi and K. Watanabe. “Synthesis of high-purity boron nitride single crystals under high pressure by using Ba–BN solvent”. In: *Journal of Crystal Growth* 303.2 (2007), pp. 525–529.

[46] S. Matt Gilbert et al. “Fabrication of Subnanometer-Precision Nanopores in Hexagonal Boron Nitride”. In: *Sci Rep* 7.1 (2017), pp. 1–7.

[47] S. Matt Gilbert et al. “Alternative stacking sequences in hexagonal boron nitride”. In: *2D Mater.* 6.2 (2019), p. 021006.

[48] Cheol-Joo Kim et al. “Stacking Order Dependent Second Harmonic Generation and Topological Defects in h-BN Bilayers”. In: *Nano Lett.* 13.11 (2013), pp. 5660–5665.

[49] Nasim Alem et al. “Atomically thin hexagonal boron nitride probed by ultrahigh-resolution transmission electron microscopy”. In: *Phys. Rev. B* 80.15 (2009), p. 155425.

[50] J. Kotakoski et al. “Electron knock-on damage in hexagonal boron nitride monolayers”. In: *Phys. Rev. B* 82.11 (2010), p. 113404.

[51] Jamie H. Warner et al. “Atomic Resolution Imaging and Topography of Boron Nitride Sheets Produced by Chemical Exfoliation”. In: *ACS Nano* 4.3 (2010), pp. 1299–1304.

[52] Jannik C. Meyer et al. “Selective Sputtering and Atomic Resolution Imaging of Atomically Thin Boron Nitride Membranes”. In: *Nano Lett.* 9.7 (2009), pp. 2683–2689.

[53] Gyeong Hee Ryu et al. “Atomic-scale dynamics of triangular hole growth in monolayer hexagonal boron nitride under electron irradiation”. In: *Nanoscale* 7.24 (2015), pp. 10600–10605.

[54] Nasim Alem et al. “Vacancy growth and migration dynamics in atomically thin hexagonal boron nitride under electron beam irradiation”. In: *physica status solidi (RRL) – Rapid Research Letters* 5.8 (2011), pp. 295–297.

[55] Zhi Zhou et al. “DNA Translocation through Hydrophilic Nanopore in Hexagonal Boron Nitride”. In: *Scientific Reports* 3 (2013), p. 3287.

[56] Song Liu et al. “Boron Nitride Nanopores: Highly Sensitive DNA Single-Molecule Detectors”. In: *Advanced Materials* 25.33 (2013), pp. 4549–4554.

[57] Thang Pham et al. “A Universal Wet-Chemistry Route to Metal Filling of Boron Nitride Nanotubes”. In: *Nano Lett.* 16.1 (2016), pp. 320–325.

[58] Aidin Fathalizadeh et al. “Scaled Synthesis of Boron Nitride Nanotubes, Nanoribbons, and Nanococoons Using Direct Feedstock Injection into an Extended-Pressure, Inductively-Coupled Thermal Plasma”. In: *Nano Lett.* 14.8 (2014), pp. 4881–4886.

[59] Sally Turner et al. “Self-assembly and metal-directed assembly of organic semiconductor aerogels and conductive carbon nanofiber aerogels with controllable nanoscale morphologies”. In: *Carbon* 153 (2019), pp. 648–656.

[60] Sally Turner et al. “Density Tunable Graphene Aerogels Using a Sacrificial Polycyclic Aromatic Hydrocarbon”. In: *physica status solidi (b)* 254.11 (2017), p. 1700203.

[61] Jonathan da Rocha Martins and Hélio Chacham. “Disorder and Segregation in B-C-N Graphene-Type Layers and Nanotubes: Tuning the Band Gap”. In: *ACS Nano* 5.1 (2011), pp. 385–393.

[62] Yao Zheng et al. “Two-Step Boron and Nitrogen Doping in Graphene for Enhanced Synergistic Catalysis”. In: *Angewandte Chemie International Edition* 52.11 (2013), pp. 3110–3116.

[63] Shuangyin Wang et al. “BCN Graphene as Efficient Metal-Free Electrocatalyst for the Oxygen Reduction Reaction”. In: *Angewandte Chemie International Edition* 51.17 (2012), pp. 4209–4212.

[64] Li Song et al. “Anomalous insulator-metal transition in boron nitride-graphene hybrid atomic layers”. In: *Phys. Rev. B* 86.7 (2012), p. 075429.

[65] Baleeswaraiah Muchharla et al. “Tunable Electronics in Large-Area Atomic Layers of Boron–Nitrogen–Carbon”. In: *Nano Lett.* 13.8 (2013), pp. 3476–3481.

[66] R. F. Egerton. *Electron Energy-Loss Spectroscopy in the Electron Microscope.* Springer Science & Business Media, 2011.

[67] Koretaka Yuge. “Phase stability of boron carbon nitride in a heterographene structure: A first-principles study”. In: *Phys. Rev. B* 79.14 (2009), p. 144109.

[68] Ph. Redlich et al. “BCN nanotubes and boron doping of carbon nanotubes”. In: *Chemical Physics Letters* 260.3 (1996), pp. 465–470.

[69] P.W. Shor. “Algorithms for quantum computation: discrete logarithms and factoring”. In: *Proceedings 35th Annual Symposium on Foundations of Computer Science.* 1994, pp. 124–134.

[70] Richard P. Feynman. “Simulating physics with computers”. In: *Int J Theor Phys* 21.6 (1982), pp. 467–488.

[71] Charles H. Bennett and Gilles Brassard. “Quantum cryptography: Public key distribution and coin tossing”. In: *Theoretical Computer Science* 560 (2014), pp. 7–11.

[72] R. L. Rivest, A. Shamir, and L. Adleman. “A Method for Obtaining Digital Signatures and Public-Key Cryptosystems”. In: *Communications of the ACM* 21 (1978), pp. 120–126.

[73] J. I. Cirac and P. Zoller. “Quantum Computations with Cold Trapped Ions”. In: *Phys. Rev. Lett.* 74.20 (1995), pp. 4091–4094.

[74] David G. Cory, Amr F. Fahmy, and Timothy F. Havel. “Ensemble quantum computing by NMR spectroscopy”. In: *Proc Natl Acad Sci U S A* 94.5 (1997), pp. 1634–1639.

[75] G. Wendin. “Quantum information processing with superconducting circuits: a review”. In: *Rep. Prog. Phys.* 80.10 (2017), p. 106001.

[76] T. E. Northup and R. Blatt. “Quantum information transfer using photons”. In: *Nature Photonics* 8.5 (2014), pp. 356–363.

[77] S. Meuret et al. “Photon Bunching in Cathodoluminescence”. In: *Phys. Rev. Lett.* 114.19 (2015), p. 197401.

[78] Rosa Brouri et al. “Photon antibunching in the fluorescence of individual color centers in diamond”. In: *Opt. Lett., OL* 25.17 (2000), pp. 1294–1296.

[79] Chen-How Huang, Yung-Hsiang Wen, and Yi-Wei Liu. “Measuring the second order correlation function and the coherence time using random phase modulation”. In: *Opt. Express, OE* 24.4 (2016), pp. 4278–4288.

[80] Hoi-Kwong Lo, Marcos Curty, and Kiyoshi Tamaki. “Secure quantum key distribution”. In: *Nature Photonics* 8.8 (2014), pp. 595–604.

[81] Valerio Scarani et al. "The security of practical quantum key distribution". In: *Rev. Mod. Phys.* 81.3 (2009), pp. 1301–1350.

[82] Pieter Kok et al. "Linear optical quantum computing with photonic qubits". In: *Rev. Mod. Phys.* 79.1 (2007), pp. 135–174.

[83] Jeremy L. O'Brien, Akira Furusawa, and Jelena Vučković. "Photonic quantum technologies". In: *Nature Photonics* 3.12 (2009), pp. 687–695.

[84] Christian Kurtsiefer et al. "Stable Solid-State Source of Single Photons". In: *Phys. Rev. Lett.* 85.2 (2000), pp. 290–293.

[85] P. Neumann et al. "Multipartite Entanglement Among Single Spins in Diamond". In: *Science* 320.5881 (2008), pp. 1326–1329.

[86] S. Castelletto et al. "A silicon carbide room-temperature single-photon source". In: *Nature Materials* 13.2 (2014), pp. 151–156.

[87] Anthony J. Morfa et al. "Single-Photon Emission and Quantum Characterization of Zinc Oxide Defects". In: *Nano Lett.* 12.2 (2012), pp. 949–954.

[88] Toan Trong Tran et al. "Robust Multicolor Single Photon Emission from Point Defects in Hexagonal Boron Nitride". In: *ACS Nano* 10.8 (2016), pp. 7331–7338.

[89] Toan Trong Tran et al. "Quantum Emission from Defects in Single-Crystalline Hexagonal Boron Nitride". In: *Phys. Rev. Applied* 5.3 (2016), p. 034005.

[90] Romain Bourrellier et al. "Bright UV Single Photon Emission at Point Defects in h-BN". In: *Nano Lett.* 16.7 (2016), pp. 4317–4321.

[91] Nasreen G. Chopra et al. "Boron Nitride Nanotubes". In: *Science* 269.5226 (1995), pp. 966–967.

[92] Angel Rubio, Jennifer L. Corkill, and Marvin L. Cohen. "Theory of graphitic boron nitride nanotubes". In: *Phys. Rev. B* 49.7 (1994), pp. 5081–5084.

[93] D. Golberg et al. "Octahedral boron nitride fullerenes formed by electron beam irradiation". In: *Appl. Phys. Lett.* 73.17 (1998), pp. 2441–2443.

[94] Thang Pham et al. "Formation and Dynamics of Electron-Irradiation-Induced Defects in Hexagonal Boron Nitride at Elevated Temperatures". In: *Nano Lett.* 16.11 (2016), pp. 7142–7147.

[95] Daniel B. Durham, D. Frank Ogletree, and Edward S. Barnard. "Scanning Auger spectromicroscopy using the ScopeFoundry software platform". In: *Surface and Interface Analysis* 50.11 (2018), pp. 1174–1179.

[96] Francisco de la Peña et al. *hyperspy/hyperspy: HyperSpy v1.5.2.* 2019. DOI: `10.5281/zenodo.3396791`. URL: `https://doi.org/10.5281/zenodo.3396791`.

[97] P. Jaffrennou et al. "Origin of the excitonic recombinations in hexagonal boron nitride by spatially resolved cathodoluminescence spectroscopy". In: *Journal of Applied Physics* 102.11 (2007), p. 116102.

[98] Nicholas V. Proscia et al. “Near-deterministic activation of room-temperature quantum emitters in hexagonal boron nitride”. In: *Optica, OPTICA* 5.9 (2018), pp. 1128–1134.

[99] Matthew A. Feldman et al. “Colossal photon bunching in quasiparticle-mediated nanodiamond cathodoluminescence”. In: *Phys. Rev. B* 97.8 (2018), p. 081404.

[100] Sophie Meuret et al. “Photon bunching reveals single-electron cathodoluminescence excitation efficiency in InGaN quantum wells”. In: *Phys. Rev. B* 96.3 (2017), p. 035308.

[101] Claude A. Klein. “Bandgap Dependence and Related Features of Radiation Ionization Energies in Semiconductors”. In: *Journal of Applied Physics* 39.4 (1968), pp. 2029–2038.

[102] M. V. Hauf et al. “Chemical control of the charge state of nitrogen-vacancy centers in diamond”. In: *Phys. Rev. B* 83.8 (2011), p. 081304.

[103] P. Siyushev et al. “Optically Controlled Switching of the Charge State of a Single Nitrogen-Vacancy Center in Diamond at Cryogenic Temperatures”. In: *Phys. Rev. Lett.* 110.16 (2013), p. 167402.

[104] Bernhard Grotz et al. “Charge state manipulation of qubits in diamond”. In: *Nature Communications* 3 (2012), p. 729.

[105] A. Zobelli et al. “Electron knock-on cross section of carbon and boron nitride nanotubes”. In: *Phys. Rev. B* 75.24 (2007), p. 245402.

[106] C. Donolato. “An analytical model of SEM and STEM charge collection images of dislocations in thin semiconductor layers. II. EBIC images of dislocations”. In: *physica status solidi (a)* 66.2 (1981), pp. 445–454.

[107] Ondrej Dyck et al. “Placing single atoms in graphene with a scanning transmission electron microscope”. In: *Appl. Phys. Lett.* 111.11 (2017), p. 113104.

[108] Bethany M. Hudak et al. “Directed Atom-by-Atom Assembly of Dopants in Silicon”. In: *ACS Nano* 12.6 (2018), pp. 5873–5879.

[109] T. Gaebel et al. “Photochromism in single nitrogen-vacancy defect in diamond”. In: *Appl. Phys. B* 82.2 (2006), pp. 243–246.

[110] J. Schwartz et al. “Effects of low-energy electron irradiation on formation of nitrogen–vacancy centers in single-crystal diamond”. In: *New J. Phys.* 14.4 (2012), p. 043024.

[111] M. Koperski, K. Nogajewski, and M. Potemski. “Single photon emitters in boron nitride: More than a supplementary material”. In: *Optics Communications* 411 (2018), pp. 158–165.

[112] Sumin Choi et al. “Engineering and Localization of Quantum Emitters in Large Hexagonal Boron Nitride Layers”. In: *ACS Appl. Mater. Interfaces* 8.43 (2016), pp. 29642–29648.

[113] Hanh Ngoc My Duong et al. “Effects of High-Energy Electron Irradiation on Quantum Emitters in Hexagonal Boron Nitride”. In: *ACS Appl. Mater. Interfaces* 10.29 (2018), pp. 24886–24891.

[114] Songyan Hou et al. “Localized emission from laser-irradiated defects in 2D hexagonal boron nitride”. In: *2D Mater.* 5.1 (2018), p. 015010.

[115] Zai-Quan Xu et al. “Single photon emission from plasma treated 2D hexagonal boron nitride”. In: *Nanoscale* 10.17 (2018), pp. 7957–7965.

[116] Christoph Kastl et al. “The important role of water in growth of monolayer transition metal dichalcogenides”. In: *2D Mater.* 4.2 (2017), p. 021024.

[117] Kin Fai Mak et al. “Atomically Thin MoS2: A New Direct-Gap Semiconductor”. In: *Phys. Rev. Lett.* 105.13 (2010), p. 136805.

[118] S. Lebègue and O. Eriksson. “Electronic structure of two-dimensional crystals from ab initio theory”. In: *Phys. Rev. B* 79.11 (2009), p. 115409.

[119] A. H. Castro Neto. “Charge Density Wave, Superconductivity, and Anomalous Metallic Behavior in 2D Transition Metal Dichalcogenides”. In: *Phys. Rev. Lett.* 86.19 (2001), pp. 4382–4385.

[120] Sara Barja et al. “Charge density wave order in 1D mirror twin boundaries of single-layer $MoSe_2$”. In: *Nature Physics* 12.8 (2016), pp. 751–756.

[121] V. Podzorov et al. “High-mobility field-effect transistors based on transition metal dichalcogenides”. In: *Appl. Phys. Lett.* 84.17 (2004), pp. 3301–3303.

[122] Xuming Zou et al. “Interface Engineering for High-Performance Top-Gated MoS2 Field-Effect Transistors”. In: *Advanced Materials* 26.36 (2014), pp. 6255–6261.

[123] Hennrik Schmidt et al. “Transport Properties of Monolayer MoS2 Grown by Chemical Vapor Deposition”. In: *Nano Lett.* 14.4 (2014), pp. 1909–1913.

[124] Kin Fai Mak et al. “Control of valley polarization in monolayer MoS2 by optical helicity”. In: *Nature Nanotech* 7.8 (2012), pp. 494–498.

[125] Hualing Zeng et al. “Valley polarization in MoS2 monolayers by optical pumping”. In: *Nature Nanotech* 7.8 (2012), pp. 490–493.

[126] Bairen Zhu et al. “The Study of Spin-Valley Coupling in Atomically Thin Group VI Transition Metal Dichalcogenides”. In: *Advanced Materials* 26.31 (2014), pp. 5504–5507.

[127] Yi-Hsien Lee et al. “Synthesis of Large-Area MoS2 Atomic Layers with Chemical Vapor Deposition”. In: *Advanced Materials* 24.17 (2012), pp. 2320–2325.

[128] H. F. Liu, S. L. Wong, and D. Z. Chi. “CVD Growth of MoS2-based Two-dimensional Materials”. In: *Chemical Vapor Deposition* 21.10-11-12 (2015), pp. 241–259.

[129] Kibum Kang et al. “High-mobility three-atom-thick semiconducting films with wafer-scale homogeneity”. In: *Nature* 520.7549 (2015), pp. 656–660.

[130] Saptarshi Das et al. "Beyond Graphene: Progress in Novel Two-Dimensional Materials and van der Waals Solids". In: *Annual Review of Materials Research* 45.1 (2015), pp. 1–27.

[131] Zheng Liu et al. "Strain and structure heterogeneity in MoS2 atomic layers grown by chemical vapour deposition". In: *Nature Communications* 5 (2014), p. 5246.

[132] Wei Bao et al. "Visualizing nanoscale excitonic relaxation properties of disordered edges and grain boundaries in monolayer molybdenum disulfide". In: *Nature Communications* 6 (2015), p. 7993.

[133] Sarah M. Eichfeld et al. "Highly Scalable, Atomically Thin WSe2 Grown via Metal–Organic Chemical Vapor Deposition". In: *ACS Nano* 9.2 (2015), pp. 2080–2087.

[134] Yongjun Lee et al. "Characterization of the structural defects in CVD-grown monolayered MoS2 using near-field photoluminescence imaging". In: *Nanoscale* 7.28 (2015), pp. 11909–11914.

[135] Yongji Gong et al. "Synthesis of Millimeter-Scale Transition Metal Dichalcogenides Single Crystals". In: *Advanced Functional Materials* 26.12 (2016), pp. 2009–2015.

[136] Andrew J. Ritenour et al. "Efficient n-GaAs Photoelectrodes Grown by Close-Spaced Vapor Transport from a Solid Source". In: *ACS Appl. Mater. Interfaces* 4.1 (2012), pp. 69–73.

[137] M. Lenz and R. Gruehn. "Developments in Measuring and Calculating Chemical Vapor Transport Phenomena Demonstrated on Cr, Mo, W, and Their Compounds". In: *Chem. Rev.* 97.8 (1997), pp. 2967–2994.

[138] E. Koskiahde et al. "Doping of GaAs epitaxial layers grown on (100) GaAs by close-spaced vapor transport". In: *Can. J. Phys.* 67.4 (1989), pp. 251–258.

[139] Peer Schmidt et al. "Chemical Vapor Transport Reactions–Methods, Materials, Modeling". In: *Advanced Topics on Crystal Growth* (2013).

[140] C. J. van Nieuwenburg and H. B. Blumendal. "The pneumatolytic synthesis of silicates, II". In: *Recueil des Travaux Chimiques des Pays-Bas* 50.11 (1931), pp. 989–996.

[141] G. R. Belton and R. L. McCarron. "The Volatilization of Tungsten in the Presence of Water Vapor". In: *J. Phys. Chem.* 68.7 (1964), pp. 1852–1856.

[142] G. R. Belton and A. S. Jordan. "The Volatilization of Molybdenum in the Presence of Water Vapor". In: *J. Phys. Chem.* 69.6 (1965), pp. 2065–2071.

[143] T. Millner and J. Neugebauer. "Volatility of the Oxides of Tungsten and Molybdenum in the Presence of Water Vapour". In: *Nature* 163.4146 (1949), pp. 601–602.

[144] Xi Ling et al. "Role of the Seeding Promoter in MoS2 Growth by Chemical Vapor Deposition". In: *Nano Lett.* 14.2 (2014), pp. 464–472.

[145] Jeffrey D. Cain et al. “Growth Mechanism of Transition Metal Dichalcogenide Monolayers: The Role of Self-Seeding Fullerene Nuclei”. In: *ACS Nano* 10.5 (2016), pp. 5440–5445.

[146] Yu-Chuan Lin et al. “Wafer-scale MoS2 thin layers prepared by MoO3 sulfurization”. In: *Nanoscale* 4.20 (2012), pp. 6637–6641.

[147] Ana Laura Elías et al. “Controlled Synthesis and Transfer of Large-Area WS2 Sheets: From Single Layer to Few Layers”. In: *ACS Nano* 7.6 (2013), pp. 5235–5242.

[148] Jeong-Gyu Song et al. “Layer-Controlled, Wafer-Scale, and Conformal Synthesis of Tungsten Disulfide Nanosheets Using Atomic Layer Deposition”. In: *ACS Nano* 7.12 (2013), pp. 11333–11340.

[149] Jeong-Gyu Song et al. “Controllable synthesis of molybdenum tungsten disulfide alloy for vertically composition-controlled multilayer”. In: *Nature Communications* 6 (2015), p. 7817.

[150] Yanlong Wang et al. “Raman Spectroscopy Study of Lattice Vibration and Crystallographic Orientation of Monolayer MoS2 under Uniaxial Strain”. In: *Small* 9.17 (2013), pp. 2857–2861.

[151] Hiram J. Conley et al. “Bandgap Engineering of Strained Monolayer and Bilayer MoS2”. In: *Nano Lett.* 13.8 (2013), pp. 3626–3630.

[152] Y. Feldman et al. “Bulk Synthesis of Inorganic Fullerene-like MS2 (M = Mo, W) from the Respective Trioxides and the Reaction Mechanism”. In: *J. Am. Chem. Soc.* 118.23 (1996), pp. 5362–5367.

[153] Y. Feldman, V. Lyakhovitskaya, and R. Tenne. “Kinetics of Nested Inorganic Fullerene-like Nanoparticle Formation”. In: *J. Am. Chem. Soc.* 120.17 (1998), pp. 4176–4183.

[154] Y. Feldman et al. “High-Rate, Gas-Phase Growth of MoS2 Nested Inorganic Fullerenes and Nanotubes”. In: *Science* 267.5195 (1995), pp. 222–225.

[155] L. Margulis et al. “Nested fullerene-like structures”. In: *Nature* 365.6442 (1993), pp. 113–114.

[156] A. Rothschild, J. Sloan, and R. Tenne. “Growth of WS2 Nanotubes Phases”. In: *J. Am. Chem. Soc.* 122.21 (2000), pp. 5169–5179.

[157] Fabian Pedregosa et al. “Scikit-learn: Machine Learning in Python”. In: *Journal of Machine Learning Research* 12 (2011), 2825-2830.

[158] Milinda Wasala et al. “Recent advances in investigations of the electronic and optoelectronic properties of group III, IV, and V selenide based binary layered compounds”. In: *J. Mater. Chem. C* 5.43 (2017), pp. 11214–11225.

[159] K. S. Novoselov et al. “Electric Field Effect in Atomically Thin Carbon Films”. In: *Science* 306.5696 (2004), pp. 666–669.

[160] Jun Feng et al. "Metallic Few-Layered VS2 Ultrathin Nanosheets: High Two-Dimensional Conductivity for In-Plane Supercapacitors". In: *J. Am. Chem. Soc.* 133.44 (2011), pp. 17832–17838.

[161] Andrea Splendiani et al. "Emerging Photoluminescence in Monolayer MoS2". In: *Nano Lett.* 10.4 (2010), pp. 1271–1275.

[162] Kenji Watanabe, Takashi Taniguchi, and Hisao Kanda. "Direct-bandgap properties and evidence for ultraviolet lasing of hexagonal boron nitride single crystal". In: *Nature Materials* 3.6 (2004), pp. 404–409.

[163] I. Guillamon et al. "Superconducting Density of States and Vortex Cores of 2H-NbS2". In: *Phys. Rev. Lett.* 101.16 (2008), p. 166407.

[164] Efrén Navarro-Moratalla et al. "Enhanced superconductivity in atomically thin TaS2". In: *Nat Commun* 7.1 (2016), pp. 1–7.

[165] Miguel M. Ugeda et al. "Characterization of collective ground states in single-layer NbSe2". In: *Nature Physics* 12.1 (2016), pp. 92–97.

[166] Guanxiong Liu et al. "Low-Frequency Electronic Noise in Quasi-1D TaSe3 van der Waals Nanowires". In: *Nano Lett.* 17.1 (2017), pp. 377–383.

[167] Xiaoxiang Xi et al. "Strongly enhanced charge-density-wave order in monolayer NbSe2". In: *Nature Nanotechnology* 10.9 (2015), pp. 765–769.

[168] Wonbong Choi et al. "Recent development of two-dimensional transition metal dichalcogenides and their applications". In: *Materials Today* 20.3 (2017), pp. 116–130.

[169] Dmitry V. Rybkovskiy, Alexander V. Osadchy, and Elena D. Obraztsova. "Transition from parabolic to ring-shaped valence band maximum in few-layer GaS, GaSe, and InSe". In: *Phys. Rev. B* 90.23 (2014), p. 235302.

[170] Hui Cai et al. "Band Engineering by Controlling vdW Epitaxy Growth Mode in 2D Gallium Chalcogenides". In: *Advanced Materials* 28.34 (2016), pp. 7375–7382.

[171] J. Robertson. "Electronic structure of GaSe, GaS, InSe and GaTe". In: *J. Phys. C: Solid State Phys.* 12.22 (1979), p. 4777.

[172] Sidong Lei et al. "Synthesis and Photoresponse of Large GaSe Atomic Layers". In: *Nano Lett.* 13.6 (2013), pp. 2777–2781.

[173] Zeineb Ben Aziza et al. "Tunable quasiparticle band gap in few-layer GaSe/graphene van der Waals heterostructures". In: *Phys. Rev. B* 96.3 (2017), p. 035407.

[174] PingAn Hu et al. "Synthesis of Few-Layer GaSe Nanosheets for High Performance Photodetectors". In: *ACS Nano* 6.7 (2012), pp. 5988–5994.

[175] Yubing Zhou et al. "Epitaxy and Photoresponse of Two-Dimensional GaSe Crystals on Flexible Transparent Mica Sheets". In: *ACS Nano* 8.2 (2014), pp. 1485–1490.

[176] Dattatray J. Late et al. "GaS and GaSe Ultrathin Layer Transistors". In: *Advanced Materials* 24.26 (2012), pp. 3549–3554.

[177] Hiroshi Serizawa, Yoshiro Sasaki, and Yuichiro Nishina. "Polytypes and Excitons in GaSe1-xSx Mixed Crystals". In: *J. Phys. Soc. Jpn.* 48.2 (1980), pp. 490–495.

[178] Chan Su Jung et al. "Red-to-Ultraviolet Emission Tuning of Two-Dimensional Gallium Sulfide/Selenide". In: *ACS Nano* 9.10 (2015), pp. 9585–9593.

[179] Hui Chen et al. "Intrinsic defects in gallium sulfide monolayer: a first-principles study". In: *RSC Adv.* 5.63 (2015), pp. 50883–50889.

[180] O. Del Pozo-Zamudio et al. "Photoluminescence of two-dimensional GaTe and GaSe films". In: *2D Mater.* 2.3 (2015), p. 035010.

[181] Wonjae Kim et al. "Tunable Graphene–GaSe Dual Heterojunction Device". In: *Advanced Materials* 28.9 (2016), pp. 1845–1852.

[182] Zeineb Ben Aziza et al. "van der Waals Epitaxy of GaSe/Graphene Heterostructure: Electronic and Interfacial Properties". In: *ACS Nano* 10.10 (2016), pp. 9679–9686.

[183] Xufan Li et al. "Van der Waals Epitaxial Growth of Two-Dimensional Single-Crystalline GaSe Domains on Graphene". In: *ACS Nano* 9.8 (2015), pp. 8078–8088.

[184] Youbao Ni et al. "Growth and quality of gallium selenide (GaSe) crystals". In: *Journal of Crystal Growth* 381 (2013), pp. 10–14.

[185] Stephan Hüfner and Tadeusz Waldemar Huber. *Photoelectron Spectroscopy: Principles and Applications*. Springer Science & Business Media, 2003.

[186] C. R. Whitehouse and A. A. Balchin. "Structural studies of compounds in the series GaSxSe1-x ($0 \leq x \leq 1$) grown by iodine vapour transport". In: *J Mater Sci* 13.11 (1978), pp. 2394–2402.

[187] J. C. J. M. Terhell, V. A. M. Brabers, and G. E. van Egmond. "Polytype phase transition in the series GaSe1-xSx". In: *Journal of Solid State Chemistry* 41.1 (1982), pp. 97–103.

[188] G. Arancia et al. "Electron diffraction study of melt- and vapour-grown GaSe1-xSx single crystals". In: *phys. stat. sol. (a)* 33.2 (1976), pp. 563–571.

[189] Daniel Olguín, Alberto Rubio-Ponce, and Andrés Cantarero. "Ab initio electronic band structure study of III–VI layered semiconductors". In: *Eur. Phys. J. B* 86.8 (2013), p. 350.

[190] L. Plucinski et al. "Electronic band structure of GaSe(0001): Angle-resolved photoemission and ab initio theory". In: *Phys. Rev. B* 68.12 (2003), p. 125304.

[191] Eric L. Shirley et al. "Brillouin-zone-selection effects in graphite photoelectron angular distributions". In: *Phys. Rev. B* 51.19 (1995), pp. 13614–13622.

[192] M. Mucha-Kruczynski et al. "Characterization of graphene through anisotropy of constant-energy maps in angle-resolved photoemission". In: *Phys. Rev. B* 77.19 (2008), p. 195403.

[193] M. O. D. Camara, A. Mauger, and I. Devos. “Electronic structure of the layer compounds GaSe and InSe in a tight-binding approach”. In: *Phys. Rev. B* 65.12 (2002), p. 125206.

[194] S. Nagel, A. Baldereschi, and K. Maschke. “Tight-binding study of the electronic states in GaSe polytypes”. In: *J. Phys. C: Solid State Phys.* 12.9 (1979), p. 1625.

[195] D. V. Rybkovskiy et al. “Size-induced effects in gallium selenide electronic structure: The influence of interlayer interactions”. In: *Phys. Rev. B* 84.8 (2011), p. 085314.

[196] Zeineb Ben Aziza et al. “Valence band inversion and spin-orbit effects in the electronic structure of monolayer GaSe”. In: *Phys. Rev. B* 98.11 (2018), p. 115405.

[197] Ming-Wei Chen et al. “Large-grain MBE-grown GaSe on GaAs with a Mexican hat-like valence band dispersion”. In: *npj 2D Mater Appl* 2.1 (2018), pp. 1–7.

[198] K. Rossnagel et al. “Fermi surface, charge-density-wave gap, and kinks in 2H-TaSe2”. In: *Phys. Rev. B* 72.12 (2005), 121103(R).

[199] T. Eknapakul et al. “Electronic Structure of a Quasi-Freestanding MoS2 Monolayer”. In: *Nano Lett.* 14.3 (2014), pp. 1312–1316.

[200] Taisuke Ohta et al. “Controlling the Electronic Structure of Bilayer Graphene”. In: *Science* 313.5789 (2006), pp. 951–954.

[201] Taisuke Ohta et al. “Interlayer Interaction and Electronic Screening in Multilayer Graphene Investigated with Angle-Resolved Photoemission Spectroscopy”. In: *Phys. Rev. Lett.* 98.20 (2007), p. 206802.